



HAL
open science

Thermal engineering in an epitaxial nanostructured germanium semi-conductor

Yanqing Liu

► **To cite this version:**

Yanqing Liu. Thermal engineering in an epitaxial nanostructured germanium semi-conductor. Physics [physics]. Université Joseph Fourier; Centre National de la Recherche Scientifique, 2015. English. NNT: . tel-01259689v1

HAL Id: tel-01259689

<https://hal.science/tel-01259689v1>

Submitted on 20 Jan 2016 (v1), last revised 17 Jan 2018 (v2)

HAL is a multi-disciplinary open access archive for the deposit and dissemination of scientific research documents, whether they are published or not. The documents may come from teaching and research institutions in France or abroad, or from public or private research centers.

L'archive ouverte pluridisciplinaire **HAL**, est destinée au dépôt et à la diffusion de documents scientifiques de niveau recherche, publiés ou non, émanant des établissements d'enseignement et de recherche français ou étrangers, des laboratoires publics ou privés.

THÈSE

Pour obtenir le grade de

DOCTEUR DE L'UNIVERSITÉ DE GRENOBLE

Spécialité : **Nanophysique**

Arrêté ministériel :

Présentée par

Yanqing LIU

Thèse dirigée par **Olivier Bourgeois**

préparée au sein de l'**Institut Néel**
et de l'**Ecole doctorale de Physique de Grenoble**

Thermal engineering in an epitaxial nanostructured germanium semiconductor

Thèse soutenue publiquement le **16 Novembre 2015**,
devant le jury composé de :

Prof. Emmanuel Hadji

CEA-INAC, Grenoble, Président

Prof. Clivia Sotomayor Torres

ICN, Barcelona, Rapporteur

Prof. David Lacroix

Université de Lorraine, Rapporteur

Prof. Nathalie Trannoy

Université de Reims, Examineur

Prof. Olivier Bourgeois

Institut Néel (CNRS), Grenoble, Directeur de thèse

Dr. Séverine Gomes

CETHIL (INSA/UCBL1/CNRS), Lyon, Co-Directrice de thèse

Dr. Dimitri Tainoff

Institut Néel (CNRS), Grenoble, Invité



What the sun and sky do to the senses
What the landscape and waters, hills free vistas to the eye
He has done to the soul
Though/While ever the best remains untold
Though/While the secret and the solving still are hidden

— Walt Whitman, 1948

To my parents, and all my beloved.



Acknowledgements

For these three years, I first would like to thank my PhD supervisor Pr. Olivier Bourgeois. I thank for his guidance in the work, patience with all my questions, his kindness and humor. From him I see how a serious researcher can also be a charming group leader. It has been a honor for me to have worked with him.

I should sincerely thank Dimitri Tainoff, for so many things that he has helped me during these three years in the development of this work, facing all these difficulties and problems. I am not even sure if I could make through them all without his help. He is such a good researcher, serious worker, meanwhile a funny, kind and adorable friend and brother.

I would like also to thank André Barski, Mustapha Boukhari in INAC/CEA for all their work of sample preparation. Without them, this work would not go on well. I am also grateful to Séverine Gomes and Ali Assy in CETHIL in Lyon, for all their help during my SThM experiments. It was only short periods with them and the group in CETHIL, I still cherish.

I would like to thank Jacques Richard for his help on theoretical calculations, as well as for all interesting discussions on culture and literature. Thanks to Jean-luc Garden, Emmanuel André, Gaël Moiroux and all the members in the Captercal pool for their technical help. I thank Gwenaëlle Julié, Sebastien Dufresnes and the whole Nanofab team for their help in clean room work.

I should thank the whole group of TPS, together with current members and some of the members before. It has always been a pleasure to spend time with them, during the work or out of work. They are dynamic, sportive and most importantly, they have endless interesting topics to discuss about. I believe well that under the leadership of Olivier the group will progress and prosper.

I own the biggest gratitude to my parents, my grandma and my whole family in China. I hope they know that I love them so much even if I am not there by their side. I know, without understanding what I have been doing in the PhD, they are already proud of me from far away. I would like to thank Matteo. For all these good and bad moments that we have gone through together during these years. For helping me, supporting me and staying by my side when I am not strong enough. And for trying to make me a better one.

Finally, I would like to acknowledge the financial support from the European project MERGING grant agreement No.309150, and from the Région Rhône-Alpes through the program of ARC Energy.

*Grenoble, 25 September 2015
Yanqing LIU*



Abstract

For the development of thermal engineering in semiconductor (SC) based devices, the requirement of new materials under the idea of "electron crystal - phonon glass" model stays always a great challenge. In this work, a new germanium based SC model has been studied and experimentally characterized regarding its thermal conductivity for thermal engineering. The materials are thin films of an epitaxial germanium matrix embedded with randomly distributed Ge_3Mn_5 nano-inclusions (5-50 nm in diameter), grown on a Germanium-on-insulator (GOI) substrate. The Ge matrix is demonstrated to be highly single-crystalline doped p-type by manganese atoms. TEM characterizations revealed that the nano-inclusions are nearly spherical and their geometries and diameter distributions are tunable depending on the growth parameters in molecular beam epitaxy, i.e. the Mn concentration and the annealing temperature.

The thermal conductivities of the Ge:Mn thin films have been measured using both a highly sensitive technique based on the 3-omega method, and the scanning thermal microscopy (SThM). The measurement results revealed dramatically reduced thermal conductivities (compared to Ge bulk), $3\text{-}15\text{ Wm}^{-1}\text{K}^{-1}$, for Ge:Mn thin films containing different Mn% (6%-14%) at room temperature. The minimum value of $3.3\text{ Wm}^{-1}\text{K}^{-1}$ for Ge:Mn thin film containing 10% Mn was found to have beaten the "alloy limit" of thermal conductivity set by $\text{Si}_{1-x}\text{Ge}_x$ at room temperature ($6\text{-}12\text{ Wm}^{-1}\text{K}^{-1}$). The low thermal conductivities for all Ge:Mn/GOI samples have also been confirmed by SThM results. These remarkable results have demonstrated the significant effects of the nano-inclusions on the phonon transport in the crystalline Ge matrix. Numerical simulations based on Boltzmann transport equation have been performed, and different models have been tried. Further modeling work will be continued to try to achieve a fully interpretation of the experimental results on these Ge:Mn thin films, and to understand the understand the phonon scattering mechanisms in this nano-structured SC material.

Résumé

Ce travail de thèse porte sur les propriétés de transport thermique liées aux phonons dans un nouveau matériau nano-structuré constitué de couches minces de Ge:Mn de type "electron crystal - phonon glass". Ce matériau est élaboré par épitaxie par jets moléculaires au CEA/INAC à Grenoble sur des substrats spécifiques de "Germanium-on-insulator (GOI)". Il est constitué par une matrice de germanium possédant une qualité cristalline parfaite dans laquelle est incluse une importante concentration de nano-inclusions de Ge_3Mn_5 de forme quasi-sphérique. L'analyse de clichés de microscopie électronique à transmission (MET) montre que ces nano-inclusions ont une distribution de diamètre variant de 5 à 50 nm. Il est par ailleurs possible de jouer sur les paramètres de croissance afin de modifier la dispersion de taille des inclusions ainsi que leur concentration. Cette possibilité nous a permis d'étudier de façon exhaustive l'influence des nano-inclusions sur le transport de chaleur autour de la température ambiante.

Pour ce faire, une expérience de mesure de conductivité thermique "3-omega" dédiée à ces échantillons et extrêmement sensible, a été fabriquée à l'Institut Néel. Cette expérience nous a permis de mesurer les variations de conductivité thermique induites par la modification de la distribution en taille des nano-inclusions de Ge:Mn dans des couches minces d'une centaine de nanomètres d'épaisseur, avec une erreur réduite d'environ 14%. Il a été montré que le transport thermique dans ces couches minces pouvait être réduit d'un facteur 20 comparé au germanium massif puisque des valeurs de conductivité thermique de l'ordre de $3 \text{ W m}^{-1} \text{ K}^{-1}$ ont été mesurées. Ces valeurs de conductivité thermique, confirmées par des expériences de Microscopie thermique à sonde locale (SThM) au Centre d'Energétique et de Thermique de Lyon (CETHIL), sont inférieures à la limite d'alliage pour le SiGe. Des simulations numériques ont été utilisées afin de mieux comprendre cette diminution spectaculaire de la conductivité thermique et d'interpréter les données expérimentales. Ces simulations montrent que cette diminution n'est pas explicable par des modèles théoriques standards. Ces faibles conductivités thermiques ainsi que la grande mobilité des porteurs dans le germanium font de ces matériaux à base de GeMn de bons candidats pour la thermoélectricité.



Contents

Acknowledgements	5
Abstract	7
Abstract (Français)	9
Table of contents	13
Introduction	5
1 Thermal engineering in nano-structured materials	7
1.1 Introduction to phonons and phonon transport	7
1.1.1 Phonon	7
1.1.2 Thermal transport and phonon scattering	17
1.2 Thermal engineering at nano-scale	23
1.2.1 Introduction	23
1.2.2 Nano-thermoelectrics	23
1.2.3 Nano-phononics	26
1.2.4 Conclusion	30
2 An "electron crystal-phonon glass" model system based on germanium	31
2.1 Introduction	31
2.2 Nano-inclusion embedded SC system for thermoelectrics	32
2.3 Growth of Ge:Mn thin films by MBE	33
2.4 TEM characterization of Ge:Mn thin films	35
2.5 Conclusion	39
3 Experimental methods for thermal conductivity measurement	41
3.1 Introduction	41
3.1.1 The 3-omega method	42
3.1.2 Time-domain thermo-reflectance	47
3.1.3 Scanning thermal microscopy	47
3.2 Experimental 3-omega setups	49
3.2.1 Principles for semi-infinite substrate with a finite-width transducer . . .	50
3.2.2 Differential 3-omega method for film-on-substrate system	51

Contents

3.2.3	Thermometry	53
3.2.4	Introduction of insulating layer for electrical conductive thin films . . .	54
3.2.5	Experimental setups	56
3.2.6	Validation of setups on test samples	58
3.2.7	Analysis of error and sensitivity of 3ω measurements	62
3.3	Scanning Thermal Microscopy (SThM)	64
3.3.1	Principles for thermal conductivity measurement	64
3.3.2	Effective thermal conductivity for multi-layer samples	68
3.4	Conclusion	70
4	Experimental results on Ge:Mn thin films	71
4.1	Preparation for 3ω measurements	72
4.1.1	Sample preparation and measurement setups	72
4.1.2	Tests on a Ge:Mn sample grown on a n-type Ge substrate	74
4.2	3ω measurements on a series of Ge:Mn/GOI samples	77
4.2.1	Measurements of Si thermal conductivity from GOI substrate at different temperatures	79
4.2.2	Extraction of Ge:Mn thermal conductivity	80
4.2.3	Influence of $T_{annealing}$ on Ge:Mn thermal conductivity	81
4.2.4	Influence of %Mn on Ge:Mn thermal conductivity	81
4.2.5	Discussions	86
4.2.6	Conclusion	87
4.3	Variation of Ge:Mn thermal conductivity with temperature	87
4.4	SThM measurements: effective thermal conductivity of Ge:Mn	88
4.5	Conclusion	90
5	Interpretation of the experimental results on Ge:Mn thin films	93
5.1	Modeling of Ge:Mn thin film as a porous material	93
5.2	Modeling of thermal conductivity of Ge:Mn based on Boltzmann transport equation	96
5.2.1	Callaway's model	97
5.2.2	Holland's model	99
5.2.3	Introduction of τ_{NI}^{-1} for nano-inclusion material system	104
5.2.4	Simulation results on Ge:Mn	107
5.3	Conclusion	110
6	Experimental results on other nano-structured thermoelectric materials	111
6.1	Epitaxial $\text{Ge}_x\text{Sn}_{1-x}\text{Mn}$ thin films	111
6.2	Porous alumina membranes filled with bismuth telluride nanowires	114
6.3	Conclusion	119
	Conclusions	124
	Appendix	126

Bibliography	137
List of figures	137
List of tables	145



Introduction

Engineering of phonon-related thermal properties of condensed matters has been increasingly drawing attention in recent research, especially in miniaturized devices based on Si/Ge semiconductors (SCs). Thermal engineering using cooling or energy harvesting systems becomes more and more important in various devices, especially in CMOS (Complementary Metal Oxide Semiconductor) and MEMS (Microelectromechanical systems) devices. The global challenge is to increase the efficiency of materials for the use in thermal engineering.

For SCs the principal heat carriers are phonons, which have an average mean free path of ~ 100 nm at room temperature and a broad distribution of wavelength spreading from 1 nm to few microns. With the objective of manipulating and controlling the phonon transport in SCs, the engineering of materials can then follow different approaches via playing either with phonon wavelength [1] or with the phonon mean free path [2, 3, 4]. In the last two decades, important progresses have been made in the use of nano-technologies for thermal engineering. Advancements are achieved especially in the development of nano-structured materials for thermoelectrics (TE) and nano-phononics, including different thermoelectric nanowires [5, 6], superlattices [7, 8], and 1D-3D phononic crystals ([9, 10, 11]).

As for 3D material for thermal engineering, one of the most important systems is the inclusion-embedded SC material, which shows great advantages and potential for the demonstration of thermal conductivity reduction. For crystalline semiconductors, the ideal model would be a defect-free highly crystalline system containing nanoscaled inclusions with a wide diameter distribution. It can be theoretically predicted that as the distance between the inclusions are comparable to the phonon mean free path in the matrix, the nano-inclusions can inhibit efficiently the phonon transport through introducing more phonon scattering processes.

Here in the PhD work we present an experimental investigation of the thermal properties of a germanium based "electron crystal - phonon glass" material containing nano-inclusions. The objective is to understand the mechanisms of phonon scattering in single crystalline heterogeneous materials.

Chapter 1 is a general introduction of phonon transport and thermal engineering at nano-scale. Chapter 2 focuses on the structural presentation of the studied material, which are thin films of a single-crystalline germanium matrix embedded with randomly distributed Ge_3Mn_5

Contents

nano-inclusions. The thin films are grown by epitaxy on a Germanium-on-Insulator (GOI) substrate at laboratory INAC/CEA. Nano-inclusions are found to be nearly spherical with a diameter distribution of 5-50 nm depending on the growth parameters used during the epitaxy. Moreover, the germanium matrix is perfectly crystalline and p-type doped by manganese, ensuring a high electrical conductivity of the Ge:Mn material.

Chapter 3 presents a detailed discussion on the experimental techniques that have been used in the work for the measurement of the thermal conductivities of the Ge:Mn thin films. Highly sensitive differential 3-omega techniques have been developed at Institut Néel for measurements on thin film materials, using the differential method or the Wheatstone bridge. The 3-omega technique based on differential method permits precise measurements of thermal conductivity with an error $\sim 14\%$ on electrical conductive thin films. Moreover, the scanning thermal microscopy (SThM) has also been used for the thermal characterization of the Ge:Mn samples at laboratory of Centre d'Énergétique et de Thermique de Lyon.

In chapter 4, the experimental results of the thermal conductivity of different Ge:Mn samples will be presented and discussed. The 3-omega measurements revealed dramatic reductions of the thermal conductivity by a factor of 4 to 20, compared to Ge bulk at room temperature (RT), for Ge:Mn thin films containing different Mn concentrations (6%-14%). A minimum value of $3.3 \text{ Wm}^{-1}\text{K}^{-1}$ was found for Ge:Mn thin film containing 10% Mn, below the “alloy limit” of the thermal conductivity set by $\text{Si}_{1-x}\text{Ge}_x$ at RT ($6\text{-}12 \text{ Wm}^{-1}\text{K}^{-1}$). This minimum value corresponds, theoretically, to a remarkably reduced phonon mean free path of 11 nm in the Ge:Mn thin film at RT compared to Ge bulk. The results of SThM measurements also confirmed low thermal conductivity values, far below $6 \text{ Wm}^{-1}\text{K}^{-1}$, for all Ge:Mn samples at RT.

Chapter 5 focuses on the work of numerical modeling, with the objective of trying to theoretically explain the physics behind the experimental results presented in chapter 4. A model for porous medium has been tried and simulations based on the solution of the Boltzmann transport equation have been performed. Different modified Callaway/Holland models have been applied to try to interpret the experimental results and to understand the mechanisms of the influence of the nano-inclusions on the phonon transport in semi-conductor materials. The simulation results show similar trend of the Ge:Mn thermal conductivity as a function of Mn concentration compared to the experimental results. Using the model developed by Asen-Palmer et al. [12] encouraging coherence with the experimental results was found, with thermal conductivity values of $7\text{-}8 \text{ Wm}^{-1}\text{K}^{-1}$ for all Ge:Mn thin films. However, the models failed to fully describe the absolute low value of the Ge:Mn thermal conductivity at RT.

Taking the benefit of the home-made highly sensitive 3-omega setup, thermal conductivity measurements on several other potential thermoelectric thin film materials have also been done in this work. It concerns $\text{Ge}_x\text{Sn}_{1-x}\text{Mn}$ thin films and Al_2O_3 membranes filled with Bi_2Te_3 nanowires. The results will be presented and discussed in chapter 6.

This thesis has been prepared in the framework of a Region Rhone-Alpes COGEETEN project and the European FET Energy project MERGING (<http://merging.eu/>).

Français:

L'ingénierie des propriétés thermiques liées aux phonons a fait l'objet d'un nombre croissant d'études dont beaucoup visent à concevoir des systèmes de refroidissement ou de récupération d'énergie à une échelle micro/nanométrique avec des matériaux semi-conducteurs classiques: Si, Ge, GaAs. L'un des objectifs est par exemple une meilleure maîtrise des propriétés thermiques dans les CMOS (Complementary Metal Oxide Semiconductor) et les MEMS (Microelectromechanical systems). Le défi global est d'accroître l'efficacité des matériaux semi-conducteurs (SC) pour leur utilisation en tant que briques de base de dispositifs thermiques.

Pour les SCs, les principaux vecteurs de l'énergie thermique sont les phonons, qui ont un libre parcours moyen de quelques centaines de nanomètres et une large distribution de longueurs d'ondes qui s'étalent d'un nanomètre à quelques microns à la température ambiante. Ces deux grandeurs correspondent à deux façons de manipuler les phonons afin de contrôler les propriétés de transport thermique des matériaux, soit en jouant avec la longueur d'onde des phonons [1], soit avec leur libre parcours moyen [2, 3, 4]. Dans les deux dernières décennies, des progrès importants ont été accomplis dans l'utilisation des nano-technologies pour le contrôle et la fabrication de micro/nano dispositifs thermiques. Ces progrès ont été réalisés en particulier grâce au développement des matériaux nano-structurés pour la thermoélectricité (TE) et de la nano-phononique. Les matériaux utilisés à ces fins se présentent sous la forme de nano-fils thermoélectriques [5, 6], de super-réseaux [7, 8], et de cristaux phononiques 1D-3D ([9, 10, 11]).

Des nano-matériaux 3D sont également étudiés pour leurs propriétés thermiques. Parmi ces matériaux, les systèmes les plus intéressants sont les matériaux "electron crystal – phonon glass". Ces matériaux sont constitués d'une matrice semi-conductrice cristalline au sein de laquelle serait intégrée une grande concentration de nano-inclusions. Pour les semi-conducteurs cristallins, le modèle idéal serait une matrice cristalline permettant un bon transport électronique contenant des inclusions nanométriques avec une large distribution de diamètre qui elles limiteraient le transport des phonons. Si la distance entre les inclusions est supérieure au libre parcours moyen des électrons, soit environ 1 nm à 300 K, les propriétés de transport électronique seront celles du massif. Si cette distance est inférieure ou comparable au libre parcours moyen des phonons dans la matrice, soit environ 100 nm dans un SC, les nano-inclusions empêcheront les phonons de participer efficacement au transport thermique à cause des multiples processus de diffusion. Des inclusions espacées d'environ 10 nm devraient permettre de retrouver des propriétés de type "electron crystal – phonon glass".

Dans ce travail de thèse, nous présentons une étude expérimentale des propriétés thermiques d'un matériau de type "electron crystal – phonon glass" à base de germanium contenant des nano-inclusions. L'objectif de ce travail est de comprendre les mécanismes de diffusion des phonons dans les matériaux hétérogènes monocristallins.

Le chapitre 1 est une introduction générale portant sur le transport des phonons et l'ingénierie thermique à l'échelle nanométrique.

Le chapitre 2 présente la structure du matériau étudié qui se présente sous la forme de films minces composées d'une matrice de germanium monocristalline au sein de laquelle sont intégrées des nano-inclusions de Ge_3Mn_5 réparties de manière aléatoire. Les films minces sont épitaxiés sur un substrat de Germanium-on-insulator (GOI) au laboratoire INAC/CEA à Grenoble. Les nano-inclusions sont quasiment sphériques et leur distribution de diamètres peut varier de 5 à 50 nm en fonction des paramètres de croissance utilisés au cours de l'épitaxie. La matrice de germanium est parfaitement cristalline et dopée de type-p par le manganèse, assurant une forte conductivité électrique.

Le chapitre 3 présente une discussion détaillée sur les techniques expérimentales qui ont été utilisées dans ce travail pour la mesure de la conductivité thermique des films minces de Ge:Mn. Deux techniques de 3-oméga hautement sensibles ont été mises au point à l'Institut Néel pour les mesures sur les matériaux en couches minces, en utilisant une configuration différentielle ou un pont de Wheatstone. La technique 3-oméga basée sur la configuration différentielle permet des mesures précises de conductivité thermique avec une erreur de 14% sur les films minces conducteurs électriques. Par ailleurs, la microscopie thermique à sonde locale (SThM) a également été utilisée pour la caractérisation thermique des échantillons de Ge: Mn au Centre d'Energétique et de Thermique de Lyon

Dans le chapitre 4, les mesures expérimentales de la conductivité thermique de différents échantillons de Ge:Mn sont présentées et discutées. Les mesures 3-oméga à température ambiante ont révélé de fortes réductions de la conductivité thermique, d'un facteur de 4 à 20 par rapport à Ge massif pour des films minces de Ge:Mn contenant différentes concentrations de Mn (6%-14%). Une valeur minimale de $3.3 \text{ Wm}^{-1} \text{ K}^{-1}$ a été trouvée pour le film mince de Ge:Mn contenant 10% de Mn, ce qui est en dessous de la "limite d'alliage" de la conductivité thermique fixée par les alliages de $\text{Si}_{1-x}\text{Ge}_x$ à température ambiante ($6-12 \text{ Wm}^{-1} \text{ K}^{-1}$). Ces faibles valeurs de conductivité thermique à température ambiante ont été confirmées par des mesures SThM. Une approche basique permet d'estimer que cette valeur minimale de conductivité thermique correspond à un libre parcours moyen des phonons d'une valeur de 11 nm dans les films minces de Ge:Mn. Cette valeur est très fortement réduite à température ambiante par rapport au libre parcours moyen des phonons dans le Ge massif qui est d'environ 230 nm

Le chapitre 5 se concentre sur la modélisation numérique, avec l'objectif d'expliquer théoriquement la physique sous-jacente aux résultats expérimentaux présentés dans le chapitre 4. Un modèle de milieu poreux a été testé et des simulations basées sur la résolution de l'équation de transport de Maxwell-Boltzmann ont été effectuées. Différentes solutions inspirées des modèles de Callaway et Holland ont été appliquées pour tenter d'interpréter les résultats expérimentaux et de comprendre l'influence des nano-inclusions sur le transport des phonons dans les couches minces de GeMn. Les résultats des simulations montrent des tendances similaires aux résultats expérimentaux. Ainsi, en utilisant le modèle mis au point par Asen-Palmer et al.[12], une cohérence encourageante avec les résultats expérimentaux a été trouvée, avec des valeurs de conductivité thermique simulées de $7-8 \text{ Wm}^{-1} \text{ K}^{-1}$ pour les films minces de Ge:Mn. Cependant, les modèles utilisés se sont avérés inadéquats pour décrire complètement la faible valeur absolue

de la conductivité thermique de Ge:Mn mesurée à température ambiante.

L'expérience de mesure de conductivité thermique par la méthode 3-oméga construite lors de ce travail de thèse a également été utilisée pour réaliser des mesures de conductivité thermique sur plusieurs autres matériaux thermoélectriques sous forme de films minces. Ainsi les propriétés thermiques de films minces de $\text{Ge}_x\text{Sn}_{1-x}\text{Mn}$ et de membranes de Al_2O_3 remplies de nanofils de Bi_2Te_3 ont été caractérisées. Ces résultats sont présentés et discutés dans le chapitre 6.

Cette thèse a été préparée dans le cadre d'un projet Région Rhône-Alpes COGEETEN et d'un projet européen FET énergie MERGING (<http://merging.eu/>).

1 Thermal engineering in nano-structured materials

Résumé

Dans ce chapitre, nous allons présenter la quasi-particule "phonon" et discuter les principales théories et technologies d'ingénierie des propriétés thermiques liées aux phonons dans la matière condensée. Pour les matériaux semi-conducteurs et isolants, les phonons sont le lien entre les caractéristiques structurales de la matière et ses propriétés de transport thermique. Nous présenterons les propriétés de base des phonons et leur rôle dans le transport de la chaleur. Ensuite, les dernières technologies d'ingénierie des phonons dans les matériaux nano-structurés seront discutées.

In this chapter, we will discuss the principal theories and engineering technologies of phonon-related thermal properties in condensed matters. The focus is on the concept "phonon", which, for non-metals, is the link between the structural features of the matter and its thermal transport properties. We will then present the most developed phonon engineering technologies using nano-structured materials.

1.1 Introduction to phonons and phonon transport

The concept phonon, was firstly introduced by a Russian physicist Igor Tamm back in 1932. The word "phonon" originates from a Greek word which means "sound" (or "voice"). It is by principle a mechanical vibration with a certain frequency. Later, it is believed that low-energy phonons give rise to sound and high-energy ones are responsible for heat.

1.1.1 Phonon

In condensed matter physics specifically, a phonon is defined as a quasi-particle (boson) representing a quantum of lattice vibration in a periodic and elastic arrangement of atoms or molecules. It can also be described as a vibration wave having an energy of $\hbar\omega$ and momentum $\vec{p} = \hbar\vec{q}$, with ω the angular frequency, \vec{q} the wave vector and $\hbar = \frac{h}{2\pi}$, $h = 6.626 \times 10^{-34}$ J·s the

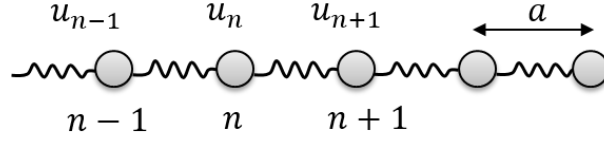


Figure 1.1: Schematic representation of a 1D linear atom chain.

Plank constant.

Dispersion relation

In the first place, it is necessary to introduce the phonon dispersion relation. The generation of phonons (vibration waves) originates from the displacement of atoms from their equilibrium position in the lattice. To simplify the analysis, it is convenient to use a model of one-dimensional infinite periodic linear atom chain, as shown in figure 1.1. In the model, all n atoms are assumed to be point particles (mass M) separated by a distance a , yet connected via an elastic spring (force constant C). $u_i, i = \dots, n-1, n, n+1 \dots$ are the displacements of atoms from their equilibrium position. The minimum possible wavelength is thus twice the inter-atomic distance a between two atoms at equilibrium.

Taking into account only the interaction with nearest neighbor atoms, the equation of motion shows:

$$M \frac{\partial^2 u(x, t)}{\partial t^2} = C(u_{n+1}(x, t) - u_n(x, t)) + C(u_{n-1}(x, t) - u_n(x, t)) \quad (1.1)$$

For harmonic oscillators, a normal vibration mode u_n takes the form:

$$u(x, t) = A e^{i(qx_n - \omega t)} \quad (1.2)$$

where x_n is the equilibrium position of the n -th atom: $x_n = na$. The dispersion relation can be obtained as:

$$\omega(q) = \sqrt{\frac{4C}{M}} \left| \sin \frac{qa}{2} \right| \quad (1.3)$$

This solution gives the dispersion curve in the first Brillouin zone as shown in figure 1.2, with only one branch known as acoustic branch. Phonons in this branch have relatively low frequencies. It is named so because at small q (close to the center of Brillouin zone), $\omega(q)$ shows a linear relation as a sound wave:

$$\omega(q) \approx \sqrt{\frac{C}{M}} qa \quad (1.4)$$

1.1. Introduction to phonons and phonon transport

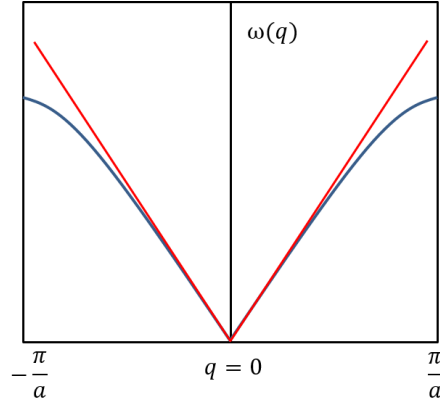


Figure 1.2: Dispersion relation curve for a 1D linear atom chain in color blue; the red lines represent the linear relation at small q .

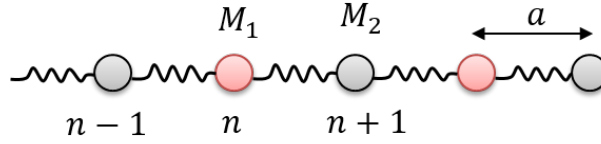


Figure 1.3: Schematic representation of a 1D diatomic linear chain.

with the velocity of the wave propagation:

$$v_g = \frac{\partial \omega}{\partial k} = \frac{\omega}{k} = v_s = a \sqrt{\frac{C}{M}} \quad (1.5)$$

where the group velocity v_g equals to the speed of sound v_s .

At the boundaries of the Brillouin zone, $v_g = 0$, indicating no propagation for these waves (standing wave).

For the case of a diatomic lattice model, being a 1D linear chain with two types of atoms M_1 and M_2 (assuming $M_1 > M_2$) as illustrated in figure 1.3, the two equations of motion are:

$$M_1 \frac{\partial^2 u_n(x, t)}{\partial t^2} = -C(2u_n(x, t) - u_{n+1}(x, t) - u_{n-1}(x, t)) \quad (1.6)$$

$$M_2 \frac{\partial^2 u_{n+1}(x, t)}{\partial t^2} = -C(2u_{n+1}(x, t) - u_{n+2}(x, t) - u_n(x, t)) \quad (1.7)$$

With the vibration modes of the atoms given by:

$$u_n(x, t) = A_1 e^{i(qna - \omega t)} \quad \text{and} \quad u_{n+1}(x, t) = A_2 e^{i(q(n+1)a - \omega t)}, \quad (1.8)$$

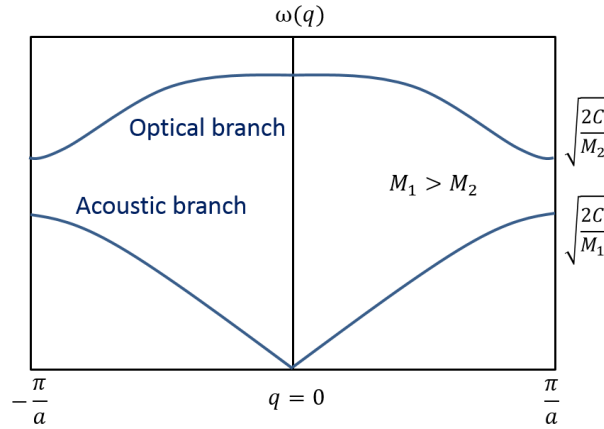


Figure 1.4: Dispersion relation curves for a 1D diatomic linear chain model, showing one optical branch and one acoustic branch. The frequency of phonon modes at the edge of the 1st Brillouin zone depends on the force constant and atom masses.

the dispersion relation $\omega(q)$ is:

$$\omega^2 = C \left(\frac{1}{M_1} + \frac{1}{M_2} \right) \pm C \sqrt{\left(\frac{1}{M_1} + \frac{1}{M_2} \right)^2 - \frac{4 \sin^2 qa}{M_1 M_2}} \quad (1.9)$$

Depending on the sign of the second term in equation 1.9, there are two solutions corresponding to two types of dispersion curves at a given q : acoustic branch and optical branch, as shown in figure 1.4. The optical branch has smaller wavelength vibrations and is responsible for most optical behavior of solids. Optical phonons have higher energy than acoustic ones, so that they are mainly responsible for heat storage (heat capacity) at room temperature. The group velocity of optical phonons is:

$$v_g = \frac{\partial \omega}{\partial k} \approx 0 \quad (1.10)$$

showing that optical phonons are not propagating and thus do not contribute to heat transport in the material.

Depending on the direction of the vibration mode u , both acoustic and optical branches can have two polarizations: longitudinal or transverse. The longitudinal polarization refers to the case where the displacement of the atoms follows the direction of the wave propagation; whereas the transverse polarization means that the vibration of the atoms is perpendicular to the wave propagation direction.

In figure 1.4 for the acoustic branch at $q = 0$, $\omega = 0$ and $A_1 = A_2$, that the two atoms in the cell have the same oscillation amplitude and phase, the dispersion relation is linear with the

1.1. Introduction to phonons and phonon transport

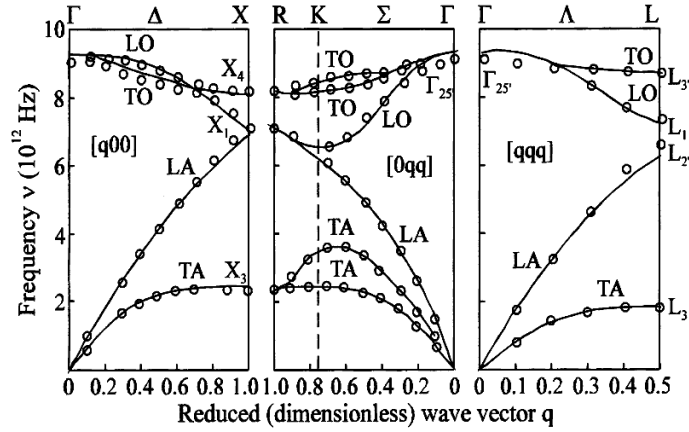


Figure 1.5: Phonon dispersion curves of bulk germanium [13]. Symbol Γ represents the center of the Brillouin zone.

wavenumber:

$$\omega = \nu_s q \quad (1.11)$$

So long wavelength acoustic phonons packets can propagating at the speed of sound in the lattice independently of their frequencies over large distance without breaking apart.

For optical branch at $q = 0$:

$$\omega = \sqrt{2C \left(\frac{1}{M_1} + \frac{1}{M_2} \right)} \quad \text{and} \quad M_1 A_1 + M_2 A_2 = 0 \quad (1.12)$$

where the mass center of the two atoms remains fixed with the two atoms moving out of phase.

At the edges of the Brillouin zone ($q = \pm \frac{\pi}{a}$):

$$\omega = \sqrt{\frac{2C}{M_2}} \quad \text{for optical branch; and} \quad \omega = \sqrt{\frac{2C}{M_1}} \quad \text{for acoustic branch.} \quad (1.13)$$

For a 3D periodic model containing N unit cells with s atoms in each, the dispersion relation is found to have $3s$ solutions, with 3 acoustic branches (one longitudinal mode and two transverse modes), and $3s - 3$ optical branches. Taking Germanium as an example, with a diamond cubic crystalline structure, a typical phonon dispersion curve is as presented in figure 1.5.

Chapter 1. Thermal engineering in nano-structured materials

The Bose-Einstein statistics is used to predict the probability that a boson occupies a specific quantum state in a system at thermal equilibrium. The number of phonons (n_{phonon}) having a frequency ω at temperature T is then given by the probability distribution function:

$$n_{phonon} = \frac{1}{e^{\hbar\omega/k_B T} - 1} \quad (1.14)$$

where k_B is the Boltzmann constant, $k_B = 1.38 \times 10^{-23}$ J/K and T the absolute temperature. It shows that as temperature increases, the number of phonons with frequency ω increases as well.

Then to calculate the total energy of lattice vibrations in the material, one should multiply the phonon number by phonon energy $\hbar\omega$ and sum over all allowed frequencies ($\omega_{\vec{q},P}$), i.e. over all allowed wave vectors (\vec{q}) and the polarizations (P):

$$U = \sum_P \sum_{\vec{q}} \frac{\hbar\omega_{\vec{q},P}}{e^{\hbar\omega_{\vec{q},P}/k_B T} - 1} \quad (1.15)$$

The concept of the phononic density of states $D_{ph}(\omega)$ is thereby introduced, being the number of phonon modes of polarization P within $d\omega$, so that the total energy is:

$$U = \sum_P \int D_{ph}(\omega) \frac{\hbar\omega_{\vec{q},P}}{e^{\hbar\omega_{\vec{q},P}/k_B T} - 1} d\omega \quad (1.16)$$

Phonon wavelength

So to calculate the total energy of phonons and investigate more the properties of phonons, we need to see more into the phonon wavelength.

For the analysis of the phonon wavelength, an approximation based on black-body emission is generally applied. The principle of the black-body radiation is that, in its thermal equilibrium (at a definite temperature), a black-body emits isotropically all possible electromagnetic radiations at every frequency, according to Planck's law. It gives a spectral radiance peaked at a certain wavelength, indifferent of shape or composition but determined by temperature only.

The Plank's law expressed in term of wavelength λ takes the form:

$$B_\lambda(\lambda, T) = \frac{2hc^2}{\lambda^5} \frac{1}{e^{hc/\lambda k_B T} - 1} \quad (1.17)$$

where c is the speed of light.

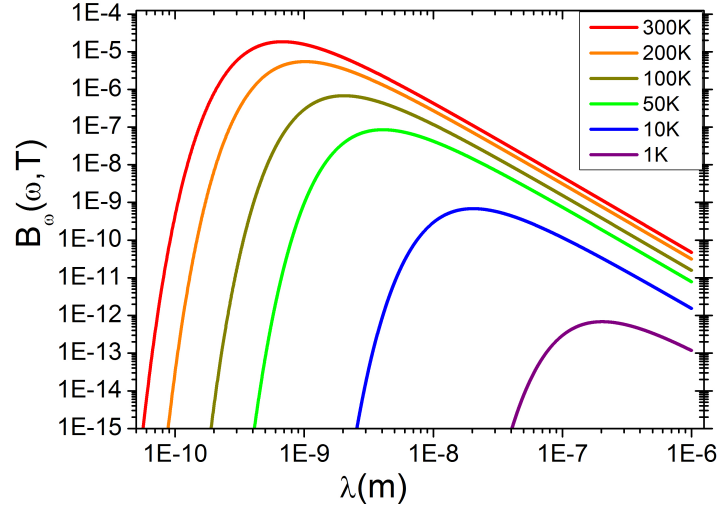


Figure 1.6: Spectral radiance curves of phonons in term of wavelength in germanium at different temperatures (from 1K to 300K). Each curve has a peak which is red-shifting as temperature decreases.

In the limit of very high temperatures ($k_B T \gg h\omega$), the expression can be reduced, expressed in terms of frequencies as:

$$B_\omega(\omega, T) \simeq \frac{\hbar\omega^3}{\pi^2 c^3} \frac{1}{e^{\hbar\omega/k_B T} - 1} \quad (1.18)$$

Similar to electromagnetic radiations, Plank's law can also be applied to phonon wavelength distribution. One can obtain the spectral radiance of phonons at a definite temperature by replacing the speed of light by the speed of sound in the material. Figure 1.6 shows the spectral radiance curves of phonons in germanium (speed of sound 5400 m/s) at different temperatures. As temperature decreases, the maximum peak of wavelength shifts toward higher value (red-shifting).

The maximum peak of phonon wavelength of one spectrum is known as dominant phonon wavelength λ_d :

$$\lambda_d = \frac{v_s}{f_d} = \frac{h v_s}{4.25 k_B T} \quad (1.19)$$

where f_d is the dominant frequency, related to the Plank constant h , the Boltzmann constant k_B and the temperature T . The constant value of 4.25 has been obtained from the experimental measurements of phonons by Klistner and Pohl [14].

Chapter 1. Thermal engineering in nano-structured materials

The signification of this dominant phonon wavelength is that, phonons with this λ_d are the most efficient energy-carriers, that most of the energy in the system is transported by them. It should be noticed that the phonon dominant wavelength is inversely proportional to temperature. As an example, the dominant phonon wavelength in germanium is around 0.2 nm at $T=300$ K and 600 nm at $T=0.1$ K.

Phonon contribution to heat capacity

The heat capacity of a solid was firstly expressed by the empirical Dulong-Petit law, proposed in 1819 by two french scientists Pierre Louis Dulong and Alexis Thérèse Petit. It states that the molar specific heat capacity of many solid elements are close to a constant value.

This constant has been proved later on being $3R$, where R is the ideal gas constant $8.314 \text{ Jmol}^{-1}\text{K}^{-1}$. For a material with number of moles N , the total heat capacity C is expressed as:

$$C = 3RN \quad (1.20)$$

This relation agrees well with high temperature experimental data. However, the Dulong-Petit law fails at low temperature with the fact that the heat capacity goes to zero at absolute zero kelvin.

The first theory stating that the heat capacity of solids due to lattices vibrations, was proposed by Einstein in 1907. The Einstein model assumes that all atoms in solid are independent 3D quantum harmonic oscillators, oscillating at a common frequency. Possible energies of each oscillator are:

$$E_n = \hbar\omega\left(i + \frac{1}{2}\right) \quad (1.21)$$

where $i = 0, 1, 2, \dots$, and the energy levels are evenly spaced by a defined smallest "quantum" of energy $\epsilon = \hbar\omega$.

In a solid containing N atoms, as each atom has three degrees of freedom, there are in fact $3N$ quantum harmonic oscillators. The heat capacity of an system at constant volume V is then defined as:

$$C_V = \left(\frac{U}{T}\right)_V \quad (1.22)$$

where U is the total internal energy of the solid.

1.1. Introduction to phonons and phonon transport

With the temperature T calculated from entropy, the final obtained expression for C_V takes the form:

$$C_V = 3Nk \left(\frac{\epsilon}{kT} \right)^2 \frac{e^{\epsilon/kT}}{(e^{\epsilon/kT} - 1)^2} \quad (1.23)$$

Einstein model of the solid predicts the heat capacity accurately at high temperatures, but at low temperatures the specific heat approaches zero exponentially fast. To correct this low temperature behavior, The Einstein model is then modified by the Debye model, developed by Peter Debye in 1912. In Debye model, "heat" is treated as the sum of energy of all phonons in a box (the solid).

Consider a cubic box of side L , along one axis the wavelength of a phonon can be estimated as:

$$\lambda_n = \frac{2L}{n} \quad (1.24)$$

where n is an integer defined as the mode number. So that the energy of the phonon can be written as:

$$E_n = \frac{hc_s}{\lambda_n} = \frac{hc_s n}{2L} \quad (1.25)$$

in which c_s is the speed of sound in the solid. This estimation of phonon energy also shows that it concerns only low-energy acoustic phonons ($q = 0$), being hence the limitation of the Debye model.

So that in three dimensions, the total energy of all phonon modes with energy E_n :

$$U = \sum_{n_x} \sum_{n_y} \sum_{n_z} E_n N(E_n) \quad (1.26)$$

where $N(E_n)$ is the number of modes with energy E_n .

Further on, the minimum wavelength of phonon should be considered, which is limited by the atomic lattice of the solid, being twice the interatomic distance:

$$\lambda_{min} = \frac{2L}{\sqrt[3]{N}} \quad (1.27)$$

where N is the atom number in the solid cube, and $\sqrt[3]{N}$ the atom number per edge. Taking the phonon number by Bose–Einstein statistics (equation 1.14), and considering three possible

Chapter 1. Thermal engineering in nano-structured materials

polarizations (one longitudinal and two transverse) for one phonon energy, the total phonon number takes the form:

$$N(E_n) = \frac{3}{e^{E_n/kT} - 1} \quad (1.28)$$

So the total energy takes the form:

$$U = \int_0^{\sqrt[3]{N}} \int_0^{\sqrt[3]{N}} \int_0^{\sqrt[3]{N}} E_n \frac{3}{e^{E_n/kT} - 1} dn_x dn_y dn_z \quad (1.29)$$

To approximate the triple integral (n_x, n_y, n_z) spherical coordinates are used:

$$(n_x, n_y, n_z) = (n \sin \theta \cos \phi, n \sin \theta \sin \phi, n \cos \theta) \quad (1.30)$$

Conserving the atom number in the cube solid, the volume of the cube (N unit-cell volumes) is then approximated as an eighth of a sphere with radius R :

$$N = \frac{1}{8} \frac{4}{3} \pi R^3 \quad (1.31)$$

so that:

$$R = \sqrt[3]{\frac{6N}{\pi}} \quad (1.32)$$

To simplify the energy integral expression, the Debye temperature T_D is defined:

$$T_D = \frac{hc_s R}{2Lk} = \frac{hc}{2k} \sqrt[3]{\frac{6N}{\pi V}} \quad (1.33)$$

where the cubic volume $V = L^3$. The Debye temperature T_D can be interpreted as the temperature at which the highest frequency mode is excited ($f_{max} = \frac{kT_D}{h}$), hence all possible modes in the solid are occupied. This hypothesis is valid only if this corresponding minimum wavelength is small compared to the dimensions of the solid (i.e. L).

The energy integral finally gives:

$$U = 9TNk \left(\frac{T}{T_D} \right)^3 \int_0^{\frac{T_D}{T}} \frac{x^3}{e^x - 1} dx \quad (1.34)$$

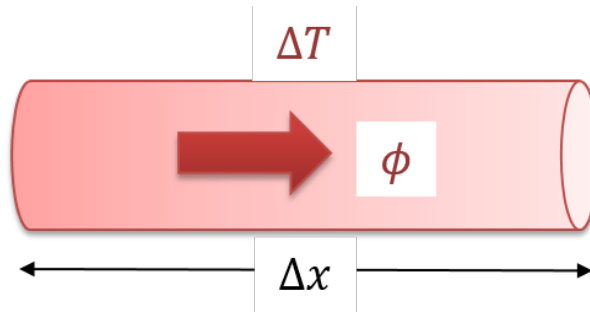


Figure 1.7: Illustration of the heat conduction in a material under a temperature gradient.

So that the heat capacity can be estimated as:

$$C_V = \frac{U}{T} = 9Nk \left(\frac{T}{T_D} \right)^3 \int_0^{\frac{T_D}{T}} \frac{x^3}{e^x - 1} dx \quad (1.35)$$

showing a temperature dependence with T^3 .

This Debye T^3 law correctly predicts the low temperature dependence of heat capacity, with coherence with experiments, meanwhile conserving the Dulong-Petit law at high temperature.

1.1.2 Thermal transport and phonon scattering

To study the thermal transport inside a material, one of the experimental measurable parameter is the thermal conductance. Being a geometry-different parameter, it is defined as the heat quantity transported through a material per unit time under a temperature gradient of one kelvin, via the formula:

$$K = \frac{P}{\Delta T} \quad (1.36)$$

where P is the heat power, ΔT the temperature gradient and K the thermal conductance with unit WK^{-1} .

As shown in figure 1.7, when a temperature gradient ΔT is applied along x on the ends of a material, heat flux is generated inside the material along x direction. In this one-dimensional case, according to Fourier's law of heat conduction, the heat flux density ϕ (defined as the amount of heat energy flows through a unit area per unit time) is proportional to the negative temperature gradient:

$$\phi = -k \frac{\Delta T}{\Delta x} \quad (1.37)$$

Chapter 1. Thermal engineering in nano-structured materials

where k is defined as the thermal conductivity of the material in $Wm^{-1}K^{-1}$, a parameter independent on the material geometry.

One should note that this simple expression is only a linear approximation for heat flux, applicable for cases where the ΔT is small compared to the local temperature, and k is nearly constant.

In different materials the quasi-particles responsible for heat conduction are different. For metals heat carriers are mainly free electrons, while in semi-conductors and insulators, they are mainly phonons.

Boltzmann transport equation

To study the heat transport property of a material and determine its thermal conductivity, the Boltzmann transport equation (BTE) is the most general and powerful method.

The BTE describes the statistical behavior of a thermodynamic system out of equilibrium. Originally developed for the study of thermodynamics in a diluted gas, the BTE has been afterwards extended to describe the change of macroscopic physical quantities in most cases where the transport of particles is involved. The method treats the probability of a particle occupying a very small region of space ($d^3\vec{r}$, \vec{r} is the position), having a small change of momentum (\vec{p}) at an instant of time (t). This is represented by the distribution function $f(\vec{r}, \vec{p}, t)$ in μ -space, which contains all the information of the transport in the system.

The general equation of BTE can be written as:

$$\frac{\partial f(\vec{r}, \vec{p}, t)}{\partial t} = \left(\frac{\partial f(\vec{r}, \vec{p}, t)}{\partial t} \right)_{force} + \left(\frac{\partial f(\vec{r}, \vec{p}, t)}{\partial t} \right)_{diff} + \left(\frac{\partial f(\vec{r}, \vec{p}, t)}{\partial t} \right)_{coll} \quad (1.38)$$

where the first term corresponds to the external force applied on the particles; the second term refers to the diffusion of the particles and the third term represents all collision processes among particle-themselves. As the particle position and momentum are 3D vectors (x,y,z), plus time, the BTE is a 7D problem in general.

Depending on the exact system, the BTE can be classified into two types: semi-classical BTE, which treats particles as points, assumes collisions are instantaneous and $\vec{r}(t)$, $\vec{q}(t)$ are uncorrelated (chaos); quantum BTE which considers quasi-particle states and includes quantum mechanical scattering phenomena.

In semi-classical BTE, if no collision exists, in time dt the particle flow in μ -space goes:

$$f(\vec{r}, \vec{p}, t) \Rightarrow f\left(\vec{r} + \vec{v}dt, \vec{v} + \frac{\vec{F}}{m}dt, t + dt\right) \quad (1.39)$$

1.1. Introduction to phonons and phonon transport

where \vec{v} is the particle velocity, m the particle mass and \vec{F} the external force. The time derivative of $f(\vec{r}, \vec{p}, t)$ is therefore:

$$\left(\vec{v} \nabla_{\vec{r}} + \frac{\vec{F}}{m} \nabla_{\vec{v}} + \frac{\partial}{\partial t} \right) f(\vec{r}, \vec{p}, t) = 0 \quad (1.40)$$

where

$$\vec{v} \nabla_{\vec{r}} \equiv v_x \frac{\partial}{\partial x} + v_y \frac{\partial}{\partial y} + v_z \frac{\partial}{\partial z} \quad (1.41)$$

and

$$\frac{\vec{F}}{m} \nabla_{\vec{v}} \equiv \frac{1}{m} \left(F_x \frac{\partial}{\partial v_x} + F_y \frac{\partial}{\partial v_y} + F_z \frac{\partial}{\partial v_z} \right) \quad (1.42)$$

To add the collision term to the above equation, some assumptions are taken to simplify the situation: (1) only two-body collisions are considered; (2) the influence of container walls are neglected; (3) the influence of possible external force on collision rate is neglected. So that the equation goes as:

$$\left(\vec{v} \nabla_{\vec{r}} + \frac{\vec{F}}{m} \nabla_{\vec{v}} + \frac{\partial}{\partial t} \right) f(\vec{r}, \vec{p}, t) = \left(\frac{\partial f(\vec{r}, \vec{p}, t)}{\partial t} \right)_{coll} \quad (1.43)$$

To solve the BTE, the approach of relaxation time approximation can be used to treat the collision term. The approach assumes that collision processes can be described by a relaxation time $\tau(p)$, being defined as the average time between collision events. It helps to describe how system returns to equilibrium, i.e. how $f(\vec{r}, \vec{p}, t)$ approaches to its equilibrium value $f^0(\vec{p})$. So that the collision term is written as:

$$\left(\frac{\partial f}{\partial t} \right)_{coll} = -\frac{f(p) - f^0(p)}{\tau(p)} \quad (1.44)$$

The relaxation time can be interpreted as the lifetime of the particles, which then refers to the phonon lifetime in the study of phonon transport in a material.

Phonon scattering

In the case of phonon-dominant heat conduction, heat is carried mainly by long wavelength acoustic phonons. However, a sum of scattering mechanisms limit the phonon transport through the material. To describe that, the phonon mean free path (MFP) is defined as the

Chapter 1. Thermal engineering in nano-structured materials

average distance traveled by phonon before being scattered or collided inside the material. The presence of scattering mechanisms can then decrease the phonon MFP in the material.

To calculate the thermal conduction of the material using BTE, all scattering processes should be taken into account in collision term. In a crystalline material, scattering processes for a phonon can include: collision with boundaries, with impurities (point defects, dislocations), electron-phonon interaction, and phonon-phonon interactions (normal process and Umklapp process).

The boundary scattering refers to the processes that a phonon hits either the grain boundaries of crystallites in a polycrystalline material, or the material borders. The roughness of the boundaries can play an important role in certain cases. The impurity scattering is a Rayleigh scattering, as the size of impurities ($\sim 1\text{\AA}$) is much smaller comparing to the dominant wavelength of phonons (1-10 nm).

The electron-phonon scattering process can result in the creation or annihilation of a phonon, or simultaneously the recombination or generation of an electron-hole pair. It is usually assumed that the contribution of phonon-electron scattering to thermal conductivity is negligible. However, highly doped semiconductors are proved to have a reduced thermal conductivity due to phonon-electron scattering.

For phonon-phonon interactions there are two types, as shown in figure 1.8. The normal process refers to a two-phonon interaction where the total phonon momentum is conserved, resulting in a third phonon going in the same direction as the incoming ones and bringing no resistance to thermal transport. The Umklapp process (U-process) involves the case where the created phonon has a wave vector (k'_3) outside the first Brillouin zone. To bring this k'_3 back inside the Brillouin zone a reciprocal lattice vector G is applied, resulting in a created third phonon with a smaller wave vector k_3 , thus smaller phonon momentum (not conserved) going in a turned direction. As a result, the U-process brings strong resistance to thermal transport, and its probability is directly related to the total number of phonons.

The relaxation time τ is used to describe each type of scattering. The reciprocal of relaxation time τ^{-1} is then known as the relaxation rate. To combine the contribution of all scattering processes, as they are independent, an approximation using Matthiessen's rule is applied:

$$\frac{1}{\tau} = \frac{1}{\tau_B} + \frac{1}{\tau_I} + \frac{1}{\tau_e} + \frac{1}{\tau_N} + \frac{1}{\tau_U} \quad (1.45)$$

where τ_B , τ_I , τ_e , τ_N , τ_U stand for relaxation time for boundary scattering, impurity scattering, electron-phonon interaction, Normal and Umklapp phonon-phonon interaction, respectively.

According to the classic kinetic theory, the thermal conductivity of an isotropic material at

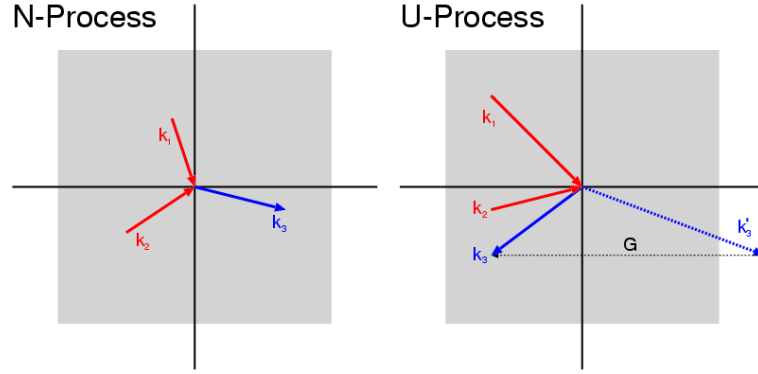


Figure 1.8: Schematic illustrations of normal process and Umklapp process. k_1 and k_2 are wave vectors of the two incoming phonons, k_3 the wave vector of created outgoing phonon; and k'_3 the sum of incoming phonon momentum pointing outside the first Brillouin zone, being equivalent to the k_3 in it after the transformation via a reciprocal lattice vector G .

temperature T is given by [15]:

$$k(T) = \frac{1}{3} C_V(T) v \Lambda(T) \quad (1.46)$$

where $C_V(T)$ is the heat capacity per unit volume at temperature T , v the heat carrier velocity and $\Lambda(T)$ the mean free path of the heat carriers at temperature T in the material.

One should note that in the above relation, the heat capacity $C_V(T)$ has not the same component at different temperatures. At low temperature, $\hbar\omega \approx k_B T$, so only acoustic modes are activated thus contribute to the heat capacity; whereas at high temperature, both acoustic and optical phonons contribute to $C_V(T)$.

As acoustic phonons travel with the speed of sound v_s , the MFP of phonon is:

$$\Lambda(T) = v_s \cdot \tau \quad (1.47)$$

It is clear that the more the scattering processes, the smaller the relaxation time, and the smaller the thermal conductivity.

For crystals with few defects, the relationship between thermal conductivity and the temperature has, theoretically and experimentally, a peaked shape shown in figure 1.9. At very low temperature, phonons are sensitive to boundary scattering, and the thermal conductivity depends on the size and shape of the material. As the heat capacity has a temperature dependence of T^3 according to Debye model, the thermal conductivity increases with T^3 as well.

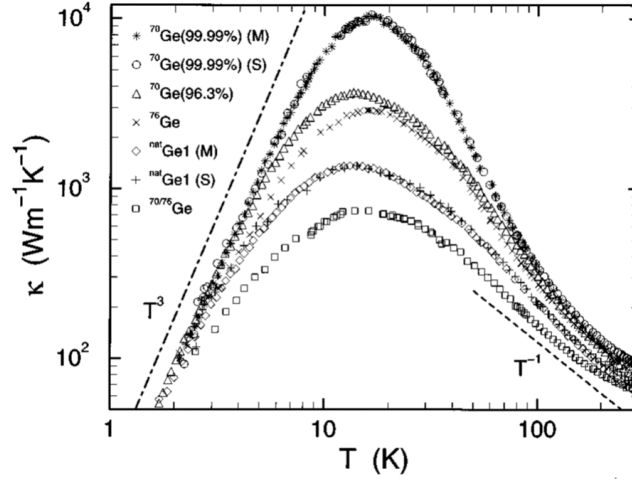


Figure 1.9: Thermal conductivity vs temperature of five germanium single crystals with different isotopic concentrations: ^{70}Ge (99.99%), ^{70}Ge (96.3%), ^{70}Ge (86%), $^{nat}\text{Ge}1$ and $^{70/76}\text{Ge}$. Sample ^{70}Ge (99.99%) and $^{nat}\text{Ge}1$ have been measured with two different experimental setups in Stuttgart (S) and Moscow (M). The dot-dashed line represents a T^3 law expected for pure boundary scattering, while the dashed line shows a $1/T$ dependence for phonon scattering at high temperature [12].

As temperature raises, U-processes begin to appear and gradually decrease the phonon MFP below the sample dimension. At this point, a maximum thermal conductivity is reached near $T \approx 0.05T_D$ (T_D being the Debye temperature), where impurity scattering dominates. Right after the maximum, the number of phonons (equation 1.14) taking part in U-process varies as $n \approx e^{-T_D/T}$, so that $\tau \approx e^{T_D/T}$, and the thermal conductivity begins to fall exponentially with temperature as well.

When temperature goes even higher ($T \gg T_D$), the number of phonons is $n \approx \frac{k_B T}{\hbar \omega}$. As a result, the phonon MFP goes as $1/T$, so as the thermal conductivity (as heat capacity is constant in this temperature range), till the melting temperature.

As for the relation between the phonon MFP and temperature, at very low temperature where only boundary scattering counts, the MFP is equal to the sample dimension. As temperature increases till Debye temperature, the phonon MFP decreases exponentially as $e^{T_D/T}$. And once T_D is bypassed, the MFP varies as $1/T$. As an example, the phonon MFP in crystalline silicon is around 100 nm at 300 K and 1 cm at 4K.

Figure 1.9 shows an example of thermal conductivity in relation with temperature in Ge samples. They are experimental curves of thermal conductivity as a function of temperature for Ge samples with different isotopic composites. Each curve shows a peak at around 15K; furthermore, as the Ge isotopic disorder increases the thermal conductivity shows a drastic decrease [12]. It has been demonstrated that this is because the isotopes increase the point

defect scattering.

As all those phonon scattering processes count for thermal transport properties inside a material, it seems very likely that we would be able to tune phonon transport through modifying scattering processes. This brings the direct motivation of doing thermal engineering using nano-technologies via playing with scatterings.

1.2 Thermal engineering at nano-scale

1.2.1 Introduction

Thermal engineering of a material refers to the study of its heat transport mechanisms, seeking to tune its thermal properties according to application requirements: thermal insulation, thermal diodes, heat harvesting, thermoelectrics and etc.

However, unlike electrical conductivity, the thermal conductivity range of existing materials is very limited. As shown in figure 1.10, electrical conductivities range from 10^{-18} S/cm to 10^8 S/cm; whereas thermal conductivity range only has a width of four order of magnitude: from 10^{-2} $\text{Wm}^{-1}\text{K}^{-1}$ to 10^2 $\text{Wm}^{-1}\text{K}^{-1}$. On the other hand, being weightless and charge-less, phonons are much more difficult to control compared to electrons. Furthermore, comparing to photons, phonons have much smaller and broader wavelengths which brings a lot more difficulties for their manipulation.

With the fast development of various applications based on SC materials, the need of thermal engineering in SCs devices gets stronger. Especially for Si/Ge based microelectronic devices, the integration of cooling system and energy harvesting/conversion systems in CMOS and MEMS devices are very much demanded. With the fact that phonons are the heat carriers in SCs and the thermal conductivity is directly related to phonon MFP, one can predict that by controlling the scale and geometry of the material it is possible to tune its thermal transport properties. Indeed, with nano-technologies, the engineering in phonon-related thermal properties of condensed matters has made dramatic progresses in the last two decades.

1.2.2 Nano-thermoelectrics

Figure of merit ZT

Thermoelectrics (TE) is one of the application domains where phonon engineering plays an important role, especially with nano-structured materials. In the domain of TE nowadays, one of the objectives is the development of SC materials with "electron crystal-phonon glass" (PGEC) features. It refers to a type of material having high electrical conductivity as in crystals and low thermal conductivity as in the glass.

Thermoelectric devices include heat generators and refrigerators. Using Seebeck effect, a

Chapter 1. Thermal engineering in nano-structured materials

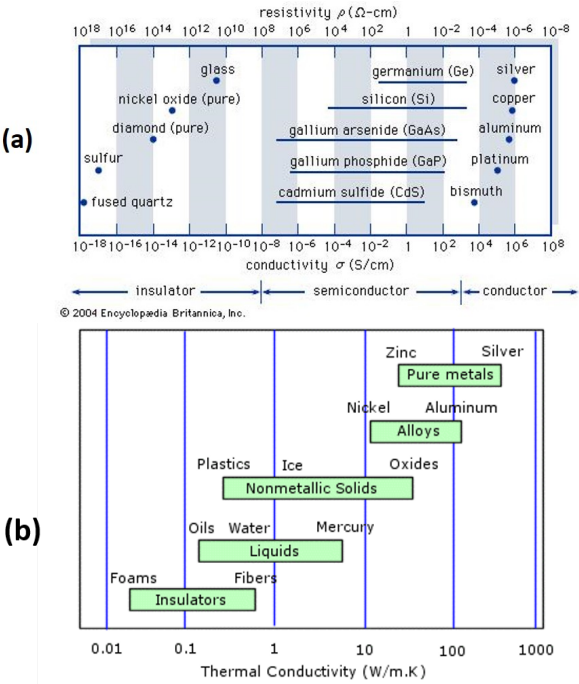


Figure 1.10: (a) Typical range of electrical conductivities for insulators, SCs and conductors; (b) range of thermal conductivities for liquids, nonmetallic solids, and pure metals at normal temperature and pressure.

thermoelectric heat generator converts waste heat into additional electrical power, as an energy recycling system. Based on Peltier effect, a compact refrigerator can be conceived. The efficiency of a thermoelectric device is determined by the temperatures at the hot and cold junctions together with the thermoelectric figure-of-merit (ZT value) of the used material. This dimensionless figure-of-merit is given by:

$$ZT = \frac{S^2 \sigma}{k_l + k_e} T \quad (1.48)$$

where S is the Seebeck coefficient, σ the electrical conductivity, T the absolute temperature, and k the thermal conductivity of the TE material. The thermal conductivity k consists of two parts: the lattice thermal conductivity k_l and the electronic thermal conductivity k_e .

In semiconductors (SCs), the electronic thermal conductivity is generally negligible below RT. However, as temperature raises above the Debye temperature, the electronic thermal conductivity can be of the same order of magnitude as the phonon contribution.

For degenerate SCs, which act more like a metal than as a semiconductor, Wiedemann-Franz law is still valid. The fact is, when highly doped (high impurity concentration though) the doping levels created by individual dopant atoms merge to form an impurity band, which then results in a behavior of increased electrical conductivity as temperature, just like a metal.

In most metals, the relation between the electronic contribution of the thermal conductivity k_e and the electrical conductivity σ is given by the Wiedemann-Franz law, being proportional to the temperature:

$$\frac{k_e}{\sigma} = LT \quad (1.49)$$

where the constant L is known as the Lorenz number:

$$L = \frac{k_e}{\sigma T} = \frac{\pi^2}{3} \left(\frac{k_B}{e} \right)^2 = 2.44 \times 10^{-8} W\Omega K^{-2} \quad (1.50)$$

The relation reports that at low temperature ($T \rightarrow 0K$) the ratio $\frac{k_e}{\sigma}$ stays approximately the same for most metals, originating from the fact that free electrons (or holes) are responsible for both heat and electrical transport in metals. But as temperature increases, deviation of the ratio L can happen due to: (i) other heat carriers such as phonon or magnon, (ii) inelastic scattering, so the law is no longer valid [16]. As temperature goes above Debye temperature, the phonon contribution is constant, the ratio L is then constant as well.

But one should note that, for metals, raising the temperature increases the thermal conductivity while decreasing the electrical conductivity. This is because the increased electron velocity

Chapter 1. Thermal engineering in nano-structured materials

(as temperature increases) favors the forward transport of energy/heat, but also increases the electron-electron collisions thus diverting the electron transport.

This ZT value of the material is directly related to the efficiency of the thermoelectric devices, including power generators based on Seebeck effect and cooling systems using Peltier effect. To optimize the thermoelectric efficiency in TE devices, materials with high ZT values are required.

One of the most efficient bulk thermoelectric materials to date is bismuth telluride (Bi_2Te_3), having a thermal conductivity of $1.2 \text{ W m}^{-1}\text{K}^{-1}$ and a ZT value of ~ 1 at RT. However, currently available thermoelectric devices based on bismuth telluride bulk have shown limited efficiencies, thermoelectric conversion efficiency $< 10\%$, due to limited ZT value and mechanical engineering challenges [17]. Hence, for the realization of RT high-performance thermoelectric devices, being competitive with traditional energy conversion system, new materials with ZT values ~ 3 are required.

Facing the challenge, in the past two decades, great progresses have been made in the development of nanostructured thermoelectric materials, from 3D to 1D, where remarkably enhanced thermoelectric figure-of-merit have been found: nano-crystalline bismuth antimony telluride ($\text{Bi}_x\text{Sb}_{2-x}\text{Te}_3$) bulk alloy [18], Bi_2Te_3 nanowire/graphene layer-by-layer composites [19], quantum-dot superlattice system of PbTe-PbSeTe [8] and of SiGe [20, 21], Si nanowires [22], SiGe nanowires arrays [23] and etc.

1.2.3 Nano-phononics

Phononics refers to studying and designing materials or structures to control, direct, modulate and manipulate lattice vibrations (sound or heat) in all type of materials. It covers all phonon related technical applications over the whole phononic spectrum (figure 1.11), including thermal insulation, noise reducing, earthquake protection, heat harvesting and etc. Advanced development of devices has been achieved in various domains, especially in acoustic and thermal diodes, optomechanics, acoustic and thermal cloaking, phononic crystals, thermoelectrics and etc.

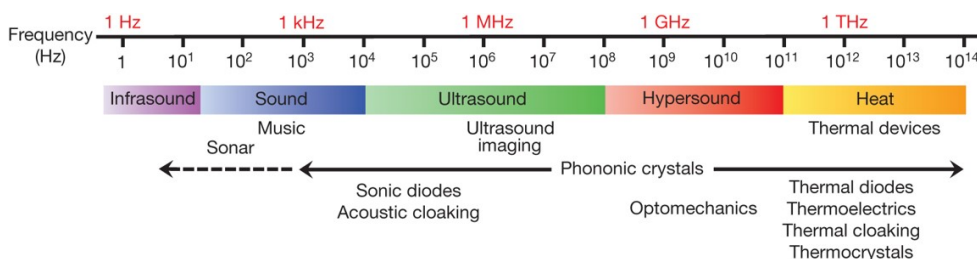


Figure 1.11: The phononic spectrum, with a frequency range of 1Hz-1THz going from infrasound to heat [24].

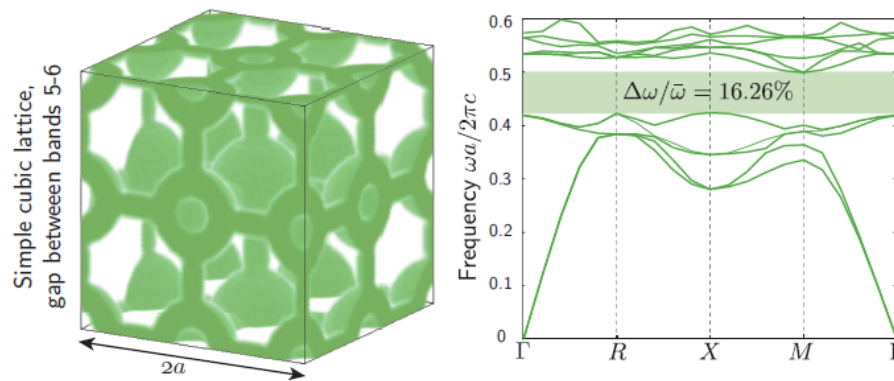


Figure 1.12: Computational phonon dispersion curve of a 3D cubic lattice PC with hollow spheres connected by cylindrical bonds. The curves show a phononic band gap of 16.26 % [31].

For the control and manipulation of sound waves, acoustic metamaterials can be designed and artificially engineered. They gain their properties from structure rather than composition. Through playing with the bulk modulus, mass density, and chirality of the material, a resonant system can be formed and the mechanical (sonic) resonance can be excited by appropriate frequencies. Thermal metamaterials can also be designed, with the function of shielding, concentrating or inverting heat. Theoretical concept on thermal shield is to use concentric layered structures (cylindrical shells for example) to maintain the inner region of the shells always at constant temperature [25]. When using materials arranged along the radial direction, a thermal concentrator can be realized, with thermal energy enhanced within the shell and remaining uniform [26]. And a thermal inverter is made of a spiral arrangement of layers in the shell with two different materials, to change the heat flux direction within the inner region of the shell [27].

Thermal diodes are devices which permit unidirectional transmission of heat. Theoretically, the match–mismatch of the vibrational modes of two coupled 1D lattices provides the unidirectional transmission of thermal energy [28]. Electrical diodes working as thermoelectric heat-pump or cooler are also reorganized as thermal diode, as well as digital electronic circuits of thermal transistor and thermal logic gates [29, 30].

The nano-phononics refers to the use of nanostructures to control and manipulate low-wavelength phonons for heat management applications, where researches are mainly going toward two directions: phononic crystals and phonon-blocking.

Coherent effect: phononic crystals

Phononic crystals (PCs) are artificial fabrication or synthesis of periodically arranged materials. It is expected to enable the manipulation of phonon dispersion properties, e.g. generating

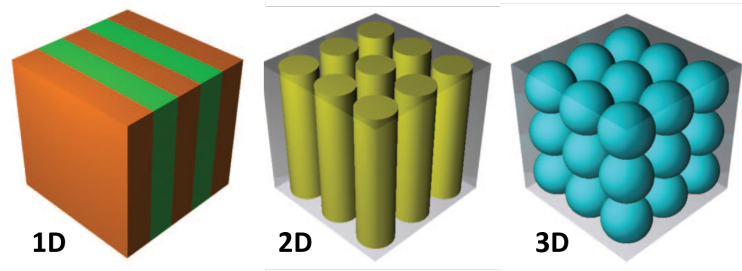


Figure 1.13: 1D, 2D and 3D PCs made of two different elastic materials arranged periodically. Different colours represent materials with different elastic properties [24].

a phononic band gap in phonon density of states, within which frequency range phonon transport is fully prohibited through the material [32, 10, 33]. These PCs can be formed by periodically varying the acoustic properties of the material (i.e. elasticity and mass). A typical phononic band gap is shown in figure 1.12, being a frequency gap between the acoustic and optical branches. It means that no phonon modes exist for these frequencies thus a phononic vibration in this frequency range can not be transported through the material. PCs can bring great opportunities to control over phonons, sound and other mechanical waves in applications of: phonon filter, mirror, resonator, phonon cavity and etc.

The opening of phononic band gap has two types of origins: the Bragg scattering and zero-transmission. Bragg scattering is the multiple scattering of propagating waves at the interfaces of a periodic arrangement of scatterers, under the condition that the structure dimensions and periods are comparable to phonon wavelength. It is a coherent effect and the Bragg's law is applicable to identify the constructive or destructive interferences.

The geometries of PCs can include 1D, 2D and 3D systems, as shown in figure 1.13. A study on a system of 2D arrays of inclusions infinitely extended along the three spatial directions shows that the width of phononic band gap depends strongly on the nature of the constituent materials (solid or fluid), as well as the physical property contrast (density and elastic moduli) between the inclusions and of the matrix [34]. 2D systems composed of parallel cylindrical [10, 35, 36] or square [33] inclusions inside a matrix have also been studied theoretically or experimentally. As for 3D PC systems, they are mainly with inclusions of spherical beads [11] or pores [37, 38] periodically distributed in a matrix. The theoretical studies on 3D PCs with different shapes of pores have found that a critical porosity exists for the formation of the absolute band gaps, and the band gap formation was easier with triangular pores then with square ones [37].

Incoherent effect: phonon-blocking

To reduce the thermal conductivity of materials for TE applications, the ideas can be to enhance the existing scattering processes or to create additional scattering process, in order

to decrease the phonon MFP furthermore and "block" the phonon transport. Practically, two methods are proved to be efficient: enhancing boundary scattering, and introducing impurities or nano-barriers to add new scattering processes.

Boundary scattering enhancement

The most direct way to enhance the phonon boundary scattering is by simply decreasing the sample size. Measurements on free-standing silicon nano-membranes show that [4], as the thickness of the Si membrane decreases from 1 μm to 10 nm, the thermal conductivity decreases dramatically from 148 to $\sim 9 \text{ Wm}^{-1}\text{K}^{-1}$ at RT.

Nanowire is proved as an efficient phonon-blocking system as well. When the phonon MFP is larger than the diameter of the nanowire, boundary scattering dominates and the phonon transport can be strongly inhibited [39, 22]. This can be used to thermally insulate suspended systems. However, in this case, the scattering by surface roughness of the nanowire wall can play an important role as well [22].

Another way of enhancing boundary scattering is to introduce grain boundaries in polycrystalline materials. Researches on a p-type nano-crystalline $\text{Bi}_x\text{Sb}_{2-x}\text{Te}_3$ bulk alloy [18] have shown a reduced thermal conductivity caused by the increased phonon scattering by grain boundaries and defects.

Nano-inclusion scattering

The nano-inclusion scattering refers to the introduction of nanoscaled barriers as phonon scatters. It has been recently demonstrated that, introducing nano-inclusions into the matrix of a thermoelectric bulk material can result in a material system with a reduced thermal conductivity. The example of an oxide inclusion of yttria stabilized zirconia (YSZ), tens of nanometer in size, embedded in the matrix of an Nb-doped SrTiO_3 has shown a reduction of lattice thermal conductivity of the matrix by a factor of two [40]. A reduction of thermal conductivity has also been revealed in an AgSbTe_2 nano-inclusion embedded $\text{Yb}_{0.2}\text{Co}_4\text{Sb}_{12}$ matrix [41]. These nano-inclusions are found to be located mainly in the grain boundaries or junctions.

In crystalline SCs, one of the most interesting systems is an epitaxial InGaAs alloy thin films containing small randomly distributed ErAs nano-inclusions. With the nano-inclusions, 2-3 nm in diameter, the thermal conductivity of the material was found to be reduced by a factor of two below the alloy limit of InGaAs [42, 43]. A lot of attention has been paid on this particular nano-inclusion embedded material in this work, with more details discussed in the following chapter.

1.2.4 Conclusion

To study the thermal properties of condensed matters, phonons are unavoidable. They link the structural features of the material directly to its thermal transport properties. As quasi-particles with quantized energy, the propagation of phonons faces a scattering environment inside the material. For SCs where phonons are the principle heat carriers, the transport of phonon determines directly the transport of heat, as well as the thermal properties of the material. It is then of great interest to study different phonon scattering mechanisms in a condensed matter, to be able to further tune or control the thermal transport. Developments have been advanced intensively in the domain of thermal engineering at nano-scale, including nano-thermoelectrics and nano-phononics. However, the seek of new material models stays still one of the greatest challenges for thermal engineering in condensed matters. Here in this PhD work, we will present a unique nano-inclusion imbedded material model based on crystalline Ge matrix. This epitaxial thin film materials can be one of the most efficient models for the scattering of phonons, resulting in a reduced thermal transport in the matrix. These materials have great interest in thermal engineering applications and thermoelectrics.

Les propriétés thermiques des matériaux isolants et semi-conducteurs sont décrites par le transport des phonons. Les phonons relient directement les caractéristiques structurelles du matériau à ses propriétés de transport thermique. En tant que quasi-particules, ils possèdent une énergie quantifiée. A température ambiante, leur propagation est diffusive à l'intérieur des matériaux. L'étude des différents mécanismes de diffusion des phonons dans la matière peut donc permettre le contrôle du transport thermique. Ces procédés sont actuellement étudiés de manière intensive pour l'ingénierie thermique à l'échelle nanométrique, y compris pour des applications en nano-thermoélectricité et en nano-phononique. Cependant, la recherche de nouveaux matériaux reste l'un des plus grands défis pour l'ingénierie thermique en matière condensée. Dans ce travail de thèse, nous présenterons un matériau modèle unique épitaxié sous forme de film mince de Ge:Mn. Ce matériau est composé d'une matrice de Ge cristalline dans laquelle se trouve une concentration élevée d'inclusions de taille nanométrique, ce qui lui confère des propriétés thermiques singulières. Ces matériaux ont un grand potentiel pour des applications en ingénierie thermique et/ou en thermoélectricité.

2 An "electron crystal-phonon glass" model system based on germanium

Résumé

Face au grand défi de la recherche de nouveaux matériaux SC pour le génie thermique, un nouveau matériau nanostructuré utilisant une matrice de germanium a été développé et étudié pour des applications en thermoélectricité dans le cadre du projet de recherche européen "MERGING". Les matériaux sont élaborés par Mustapha Boukhari et André Barski dans le groupe "Silicon, Nanoelectronics, Photonics and Structures (SINAPS)" dans le laboratoire de INAC/CEA de Grenoble.

Dans ce chapitre, nous allons tout d'abord parler des matériaux PGEC les plus intéressants pour l'ingénierie thermique et les applications TE. Nous présenterons ensuite les films minces épitaxiés de Ge:Mn, qui sont composées de nano-inclusions de Ge_3Mn_5 distribuées de façon aléatoire dans une matrice de germanium de grande qualité. Les processus régissant la croissance de ces films minces de Ge:Mn par épitaxie par jets moléculaires (MBE), ainsi que leur caractérisation structurale en microscopie électronique en transmission (MET) seront discutés en détail.

2.1 Introduction

Facing the great challenge of seeking new SC materials for thermal engineering, a new nanostructured material with germanium matrix has been developed and studied for TE applications within the European research project "MERGING". The materials are elaborated by Mustapha Boukhari and André Barski in group "Silicon, Nanoelectronics, Photonics and Structures (SINAPS)" in the laboratory of INAC/CEA in Grenoble.

In this chapter, we will firstly discuss one of the most interesting 3D PGEC material models for thermal engineering and TE applications: the nano-inclusion embedded semiconductor. We will present an unique Ge:Mn thin film material, composed of an epitaxial germanium matrix embedded with randomly distributed Ge:Mn nano-inclusions. The special growth process of this Ge:Mn thin film by Molecular Beam Epitaxy (MBE), as well as its structural characterization using transmission electron microscopy (TEM) will be discussed.

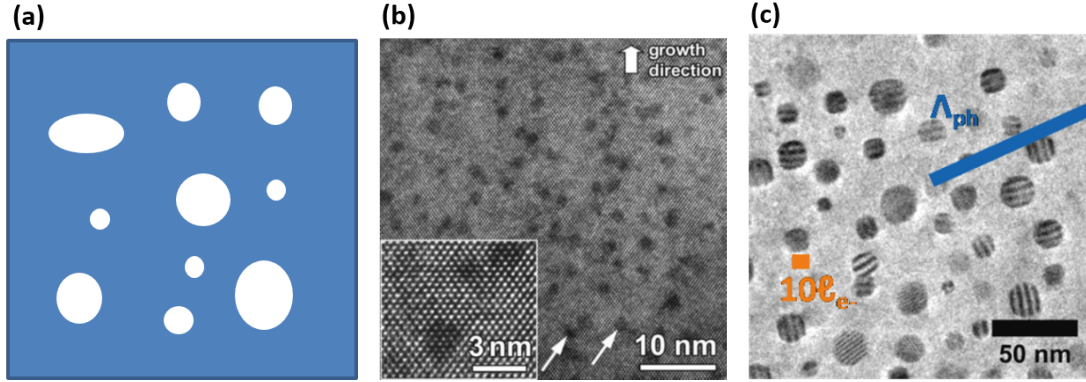


Figure 2.1: (a) Schematic illustration of a typical nano-inclusion embedded material system; (b) High-resolution cross-sectional TEM image of randomly distributed ErAs particles in an epitaxial matrix of InGaAs layer [48]; (c) TEM image of a Ge:Mn thin film containing nano-inclusions (taken by Dimitri Tainoff). In the image the scales of Λ_{ph} and l_e stand respectively for phonon MFP and electron MFP at RT.

2.2 Nano-inclusion embedded SC system for thermoelectrics

To obtain an efficient crystalline PGEC material, the method of "phonon blocking" has been applied in different ways to crystalline SCs, especially III-V and IV group SCs. The idea is to decrease the thermal conductivity using nanostructures. Researches have been done on materials of: GaAs/AlAs super-lattices (SL)[44, 45], Si/SiGe SLs [7], porous silicon [2, 46], meso-pores germanium [47], epitaxial SiGe nanodot superlattices [20, 21] and etc.

For 3D crystalline solid system, one of the most interesting structures is a nanoinclusion-embedded semiconductor matrix, as illustrated in figure 2.1(a). These nano-inclusions, distributed in the matrix, are expected to act as phonon scattering centers and create additional scattering process to inhibit phonon propagation, thus decrease the thermal conductivity of the SC matrix. This inclusion embedded system has shown its "phonon blocking" efficiency with experimental results of reduced thermal conductivity [43, 41, 40], as discussed in chapter 1. One of the most interesting systems is an epitaxial InGaAs alloy thin film ($\sim 1\mu\text{m}$) containing randomly distributed ErAs nanoparticles (2-3 nm in diameter) as shown in figure 2.1(b) [48]. It has been experimentally demonstrated that the thermal conductivity of the material has been reduced by a factor of two below the alloy limit, from $5\text{ Wm}^{-1}\text{K}^{-1}$ to $3\text{ Wm}^{-1}\text{K}^{-1}$ at RT [42, 43]. The corresponding ZT value has been increased by a factor of 2 as well, even approaching 1 at $600\text{ }^\circ\text{C}$ [43]. Further more, some thermoelectric power generator modules based this nano-inclusion alloy have been developed and tested [49, 50]. Similar enhanced thermoelectric properties have also been found in epitaxial TbAs: InGaAs nanocomposites, where TbAs nanoparticles (1nm in diameter) are randomly distributed inside the InGaAs layer [51].

However, in the model of ErAs/TbAs embedded InGaAs alloy, the nano-inclusions have ex-

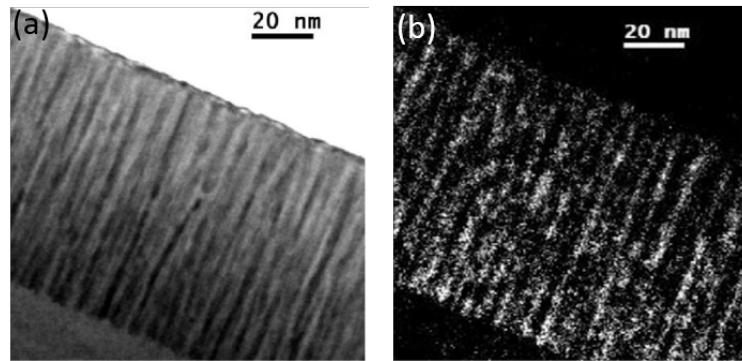


Figure 2.2: Transverse TEM images of a Ge:Mn thin film showing the presence of manganese-rich Ge_xMn_y nanocolumns in a perfect germanium crystalline matrix [53]: (a) bright field; (b) dark field.

tremely small diameters (1-3 nm) within a narrow distribution, which could be mostly efficient for scattering a limited mid-range wavelength phonons [52]. Furthermore, the small inter-inclusion distances also affect the electron transport resulting in a decreased electrical conductivity [48]. Therefore, it can be theoretically predicted that an ideal PGEC model would be a defect-free highly crystalline SC containing nano-inclusions with a relatively wide size distribution and larger inter-inclusion distances. The objective is to most efficiently scatter phonons without affecting electron transport. However, very few crystalline materials practically support this kind of nano-structuration, especially Si/Ge compatible materials, as future TE applications in microelectronics are very much expected.

In this context, we would like to present the unique Ge:Mn thin film, being a Ge based nano-structuration only achievable with manganese.

2.3 Growth of Ge:Mn thin films by MBE

The Ge:Mn thin films studied in this PhD work are composed of, an epitaxial Ge matrix heavily doped with manganese, embedded with randomly distributed nano-inclusions of Ge_3Mn_5 [53]. The fabrication of these Ge:Mn thin films is realized by molecular beam epitaxy (MBE) in the research group of SINAPS/INAC at CEA Grenoble in France. At a certain growth temperature (100 °C in most cases), when the concentration of manganese exceeds about 1% in germanium, Mn atoms segregate in a Mn-rich Ge_xMn_y columnar phase (figure 2.2) [54, 55, 56]. After a thermal annealing process at temperature between 400 and 800 °C, the Ge_xMn_y phase starts to precipitate, leading to the formation of metallic spherical nano-clusters of Ge_3Mn_5 (figure 2.3) randomly distributed in the Ge matrix [54, 57]. To our knowledge, manganese is the only element that leads to this type of nano-structuration in germanium. And reversely, it is a very specific material system based on germanium, very difficult to achieve with other materials. The tests on silicon for example, gave out SiMn alloy phases damaging the quality of Si matrix.

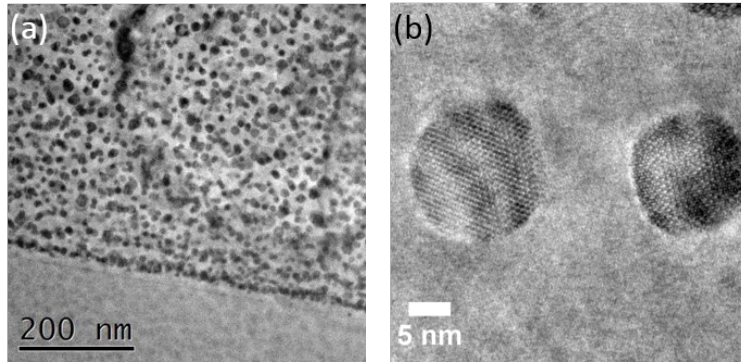


Figure 2.3: In-plane TEM images of Ge:Mn thin films (taken by Eric Prestat): (a) with the presence of Ge_3Mn_5 nano-inclusions in a $1\ \mu\text{m}$ thick Ge:Mn film; (b) showing the crystalline structures in both the Ge matrix and the inclusions.

The Ge:Mn thin film is grown from a $\langle 001 \rangle$ orientation, so that both the Ge matrix and Ge_3Mn_5 inclusions are perfectly crystalline (seen from figure 2.3(b)). The Ge matrix is a standard natural Ge, having five naturally occurring isotopes: ^{70}Ge , ^{72}Ge , ^{73}Ge , ^{74}Ge and ^{76}Ge , with ^{74}Ge the most abundant. The abundances of ^{70}Ge , ^{72}Ge , ^{73}Ge , ^{74}Ge , and ^{76}Ge isotopes are respectively 21.23%, 27.66%, 7.73%, 35.94% and 7.44%.

Depending on the growth parameters (e.x. manganese concentration, growth temperature, annealing temperature, etc.), the diameter distribution of these Ge_3Mn_5 nano-inclusions can spread over the range of 5 to 50 nm, centering at different mean values, and their concentration varies. These structural parameters can be analyzed from in-plan TEM images. From figure 2.3(b) for example, the diameter of the Ge_3Mn_5 nano-inclusions can be estimated to be ~ 10 nm.

Furthermore, the manganese atoms incorporated in the thin film are not only present within the nano-inclusions. A small concentration of Mn atoms ($\sim 10^{18}\text{cm}^{-3}$) has also been found in the Ge matrix, acting as a p-type dopant. This doping of Ge matrix ensures the overall electrical conductivity of the thin film. Thanks to the high mobility of charge carriers in germanium, the electrical conductivity of the Ge:Mn thin film can be expected to be a hundred of $\Omega^{-1}\text{cm}^{-1}$, which is crucial for a final competitive ZT value.

These Ge:Mn thin films can be grown on Ge (001, n-type or p-type) and GaAs (001) substrates. For electrical measurements, in order to avoid the parasitic conduction from the substrate, GaAs semi-insulating substrates have been used. For thermal measurements, beside the Ge substrate (both n- and p-type), a new type of substrate known as Germanium-on-Insulator (GOI), containing a semi-insulating Ge top layer, is used for the growth of Ge:Mn thin films. It is a stacking of thin layers of Ge (104 nm) and SiO_2 (188.5 nm) on top of a silicon substrate ($\sim 750\ \mu\text{m}$), as shown in figure 2.4(a). These substrates are fabricated in LETI/CEA in Grenoble. Figure 2.4(b) shows a transverse TEM image of a Ge:Mn thin film containing Ge_xMn_y nanocolumns

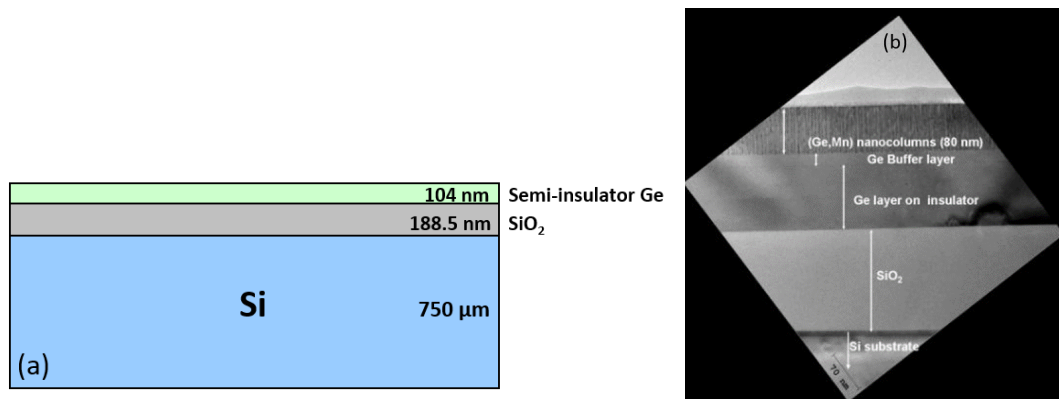


Figure 2.4: (a) Schematic illustration of the Germanium-on-Insulator substrate used for the growth of the Ge:Mn thin films; (b) transverse TEM image of a Ge:Mn thin film (80 nm thick) in Ge_xMn_y nanocolumn phase grown on a GOI substrate (taken by Eric Prestat).

grown on a GOI substrate.

The epitaxy of all Ge:Mn samples is carried out by Mustapha Boukhari and André Barski at the laboratory INAC/CEA in Grenoble, as well as the following TEM characterization work.

2.4 TEM characterization of Ge:Mn thin films

TEM observations have been carried out on different Ge:Mn thin films grown on the GOI substrate. To investigate the influence of Mn concentration on the geometry of the nano-inclusion system (e.x. the diameter distribution and mean diameter of the inclusions, the inclusion concentration), Ge:Mn thin films with different Mn concentrations have been studied. All characterized Ge:Mn films have a thickness of 240 nm, grown with Mn concentrations of 6%, 8%, 10%, 12% or 14%.

Influence of annealing temperature

The influence of annealing temperature on the geometry of nano-inclusions of Ge:Mn sample has also been studied. Ge:Mn samples containing 8% Mn but annealed at two different temperatures have been characterized by TEM. The samples are annealed at 672 or 743 °C, noted as S2 and S6 respectively.

As shown in figure 2.5, it is remarkable that for sample S6 (annealed at 743 °C), the diameter distribution is more Gaussian-like; whereas for sample S2 (annealed at 672 °C) the distribution is more in log-normal. And the mean diameter of inclusions for sample annealed at higher temperature is twice the value for the sample annealed at lower temperature, being 20 nm against 10 nm.

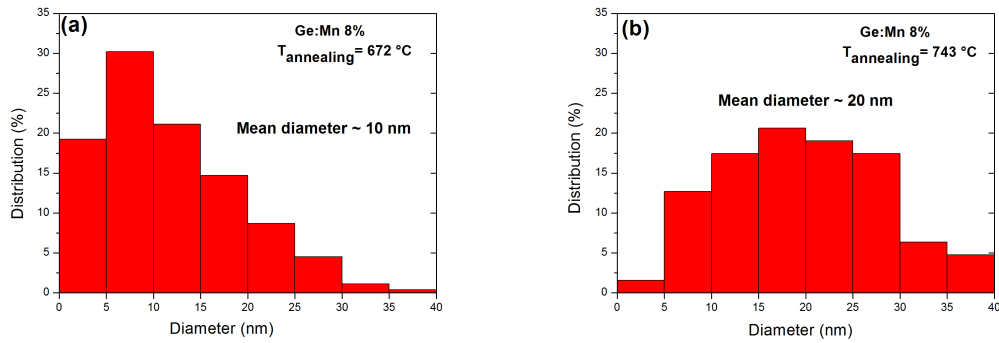


Figure 2.5: Diameter distribution graphs for nano-inclusions in Ge:Mn samples containing 8% Mn, annealed at two different temperatures: (a) at 672 °C; (b) 743 °C.

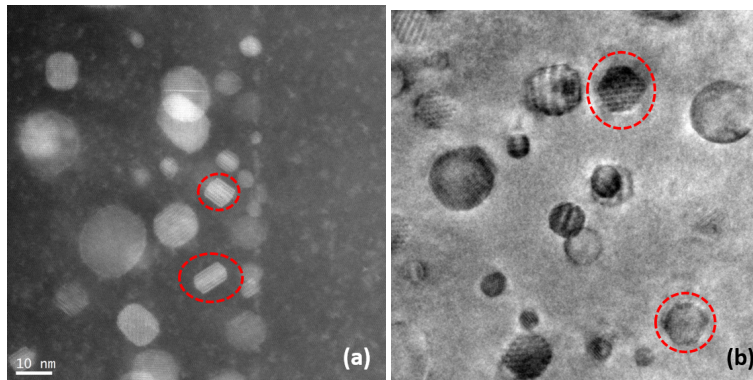


Figure 2.6: TEM images of Ge:Mn thin films showing new inclusion forms besides the form of sphere, from samples containing 8% Mn annealed at two different temperatures: (a) 672 °C; (b) 743 °C.

The annealing temperature seems also an important parameter responsible for the form of the nano-inclusions. As shown in figure 2.6, one can notice that interesting inclusion forms appear among the general spherical one, with cylindrical form in sample S2 (annealed at 672 °C), and hexagonal form in sample S6 (annealed at 743 °C).

Influence of Mn concentration

As shown in figure 2.7, Ge:Mn samples grown with 12 % and 6% Mn present significantly different nano-inclusion geometries. Although both samples are annealed at almost the same temperature, Ge:Mn with 12% Mn appears to have much bigger nano-inclusions.

The diameter distribution graphs of nano-inclusions in Ge:Mn thin films containing different Mn concentrations (8%, 10%, 12% and 14%) were extracted from TEM images. They are

2.4. TEM characterization of Ge:Mn thin films

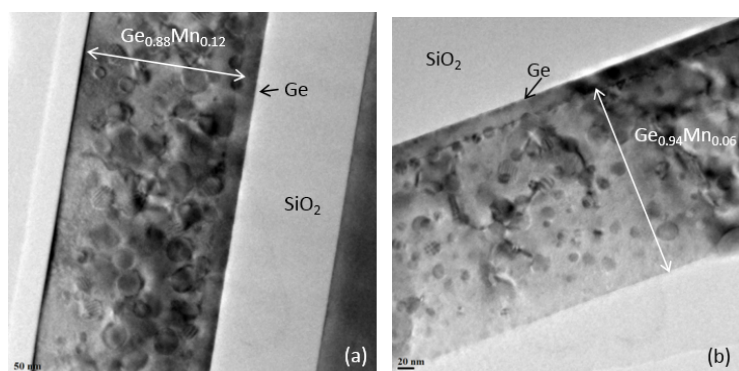


Figure 2.7: Transverse TEM images of Ge:Mn thin films (240 nm thick) grown on GOI substrates: (a) with Mn concentration of 12% and annealing temperature of 703 °C; (b) with Mn concentration of 6% and annealing temperature of 709 °C.

presented in figure 2.8. It can be noticed from figure that all distribution graphs show a more or less log-normal distribution trend. Sharp peak within a small range of diameters is evident for Ge:Mn samples with smaller Mn concentration. However, for Ge:Mn sample with 14% Mn the peak for the mean diameter is lost in the graph, and the inclusion diameter spreads over a large range of 10-80 nm.

Based on the TEM distribution graphs a set of nano-inclusion concentration values can be calculated theoretically, referred to as $C_{cal.}$, using the Mn% and considering the inclusion to be Ge_3Mn_5 . From a Gaussian treatment of the inclusion distribution graphs, the mean diameter (d_{mean}) of inclusions and the standard deviation for each Ge:Mn sample can be obtained. Moreover, another set of inclusion concentrations, C_{TEM} , has been calculated based on front view TEM images of Ge:Mn with the help of a counting software. From a TEM image of $770nm \times 770nm$ taken from a wedge of the Ge:Mn layer (240 nm thick), all visible inclusions in this volume were counted and their volumes calculated as sphere. The fraction of the sum of all inclusion volumes over the observed sample volume then gives the value of the inclusion concentration. Table 2.1 summarizes all above mentioned the structural parameters obtained from TEM characterization of Ge:Mn samples containing different Mn%. And figure 2.9 shows the curves of the two sets of nano-inclusion concentration values C_{TEM} and $C_{cal.}$, as a function of Mn concentration.

From table 2.1 and figure 2.9, it can be noticed that as Mn concentration increases from 8% to 14%, the inclusion diameter and the standard deviation increase as well. Both obtained inclusion concentrations C_{TEM} and $C_{cal.}$ decrease with the increase of Mn concentration. However, the two sets of values do not overlap with each other, with $C_{cal.}$ twice bigger than the ones of C_{TEM} . It is possible that the counting method based on TEM images underestimates the total inclusion volume, due to the ignoring of less visible or shaded inclusions. Both sets of inclusion concentration values were used in the simulation work later on, with the results compared and discussed in chapter 5.

Chapter 2. An "electron crystal-phonon glass" model system based on germanium

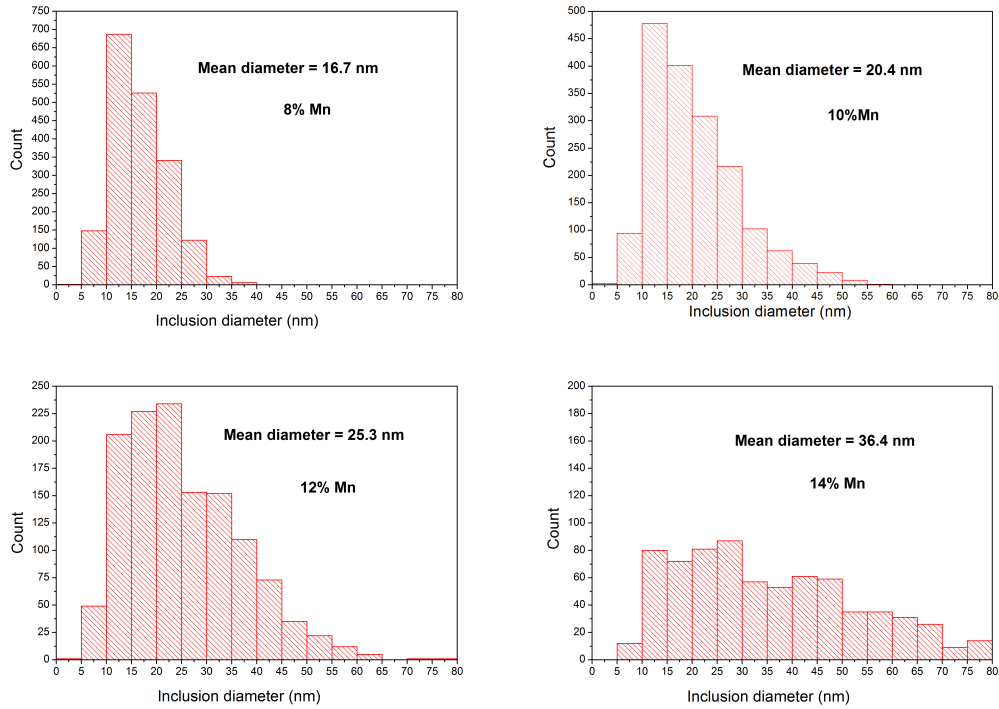


Figure 2.8: Diameter distribution graphs for nano-inclusions in Ge:Mn thin films with different Mn concentrations: 8%, 10%, 12% and 14%.

Sample	%Mn	C_{TEM} (m^{-3})	$C_{cal.}$ (m^{-3})	d_{mean} (nm)	Standard deviation (nm)
S2	8	$1.30 \cdot 10^{22}$	$3.91 \cdot 10^{22}$	16.7	5.4
S3	10	$6.09 \cdot 10^{21}$	$2.19 \cdot 10^{22}$	20.4	8.8
S4	12	$4.50 \cdot 10^{21}$	$1.35 \cdot 10^{22}$	25.3	11.5
S5	14	$2.56 \cdot 10^{21}$	$4.6 \cdot 10^{21}$	36.4	19.0

Table 2.1: Structural parameters extracted from TEM characterization on Ge:Mn samples containing different Mn concentrations. The C_{TEM} is obtained based on TEM images with front view of the sample using a software counting method; $C_{cal.}$ is the inclusion concentration calculated theoretically based on TEM distribution graphs. The inclusion mean diameter (d_{mean}) and its standard deviation are extracted from a Gaussian distribution treatment of the inclusion distribution graphs from TEM imaging.

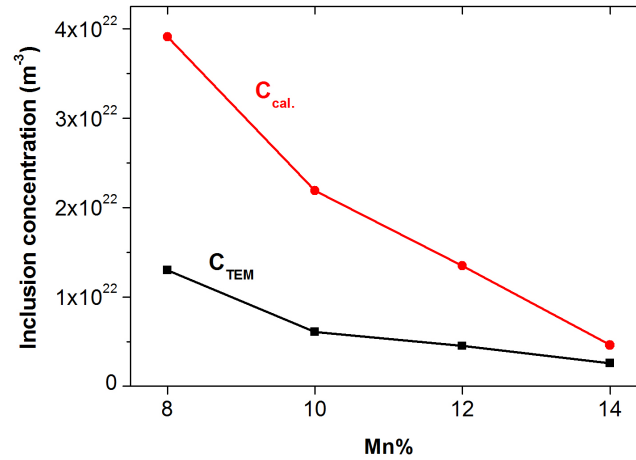


Figure 2.9: Plots of nano-inclusion concentrations C_{TEM} and $C_{cal.}$ as a function of Mn concentration.

2.5 Conclusion

To summarize, with nano-inclusions the Ge:Mn thin films have fulfilled almost all requirements for being a 3D crystalline PGEC material. The thin film is proved to be perfectly crystalline (both the matrix and inclusions) with nearly spherical nano-inclusions. The size distribution of the inclusions is tunable by varying the Mn concentration and the annealing temperature. All our structural studies confirm this Ge:Mn thin film as a promising material model for the study of phonon scattering mechanisms and for potential TE applications.

Pour résumer, ces films minces de Ge:Mn, remplissent toutes les conditions requises pour être un matériau "electron crystal - phonon glass". D'une part, la matrice de Ge est parfaitement cristalline et les nano-inclusions sont presque sphériques. D'autre part, la distribution de taille des inclusions est modifiable en faisant varier la concentration de Mn et/ou la température de recuit sans pour autant détériorer la qualité du matériau. Toutes ces études structurales font de ces film minces de Ge: Mn des matériaux prometteurs pour l'étude des mécanismes de diffusion des phonons, et pour des applications potentielles en TE.

3 Experimental methods for thermal conductivity measurement

Résumé

Pour la caractérisation des propriétés thermiques des matériaux à l'échelle micro / nano, il existe principalement trois technologies de pointe: la méthode 3-oméga, la thermorélectance (TDTR), et la microscopie thermique à sonde locale (SThM). Dans la première partie de ce chapitre, nous allons décrire les principes de ces trois techniques et comparer leurs originalités, leurs similarités et leurs différences. Dans ce travail, des expériences utilisant la méthode 3-oméga et le SThM ont été utilisées pour mesurer la conductivité thermique des films minces de Ge:Mn.

La deuxième partie de ce chapitre est consacrée à la présentation de la méthode 3-oméga conçue pour l'étude des films minces de Ge:Mn, y compris les principes théoriques et le développement de l'expérience. Deux configurations ont été développées et adaptées pour la mesure de la conductivité thermique des films minces conducteurs électriques: la configuration du pont de Wheatstone et la configuration différentielle. Ces deux configurations ont été validées sur des échantillons test. La configuration différentielle a été sélectionnée pour mesurer les échantillons. Les erreurs absolues des valeurs de conductivités thermiques obtenues en utilisant la configuration différentielle, pour des substrats et des films minces, seront analysées à la fin de cette section. Enfin, la technique de SThM, qui a été utilisée pour confirmer les mesures de conductivité thermique effectuées en 3-oméga, sera discutée dans le cas d'une sonde thermique type "Wollaston".

3.1 Introduction

For the experimental measurements of thermal conductivity of bulk materials, there are generally two classes of methods: steady-state and transient techniques. In the steady-state method, the temperature of the material does not change with time and the experimental signal is constant; while in the transient technique the thermal conductivity is deduced from the exponential decay in the temperature difference between a hot side and a cold side of the material.

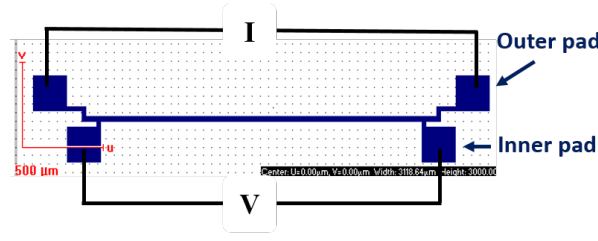


Figure 3.1: Schematic diagram of a transducer metal line in a four-contact geometry, designed for 3ω measurements.

For the characterization of thermal properties of materials at the micro/nano scale, there are mainly three advanced technologies: the 3-omega method, the time-domain thermoreflectance (TDTR), and the scanning thermal microscopy (SThM). In this section, we will describe and compare these three techniques for their originality, similarities and differences, for a comparison.

3.1.1 The 3-omega method

The 3ω method was originally developed by O. Corbino in 1912, for the measurement of the thermal diffusivity of metal filaments for the use in light bulbs. This method was used by Cahill in 1987 [58] for the measurement of thermal conductivity of solids. Later on the differential 3ω method was developed to study the thermal conductivity of thin films of amorphous silicon semiconductor [59] and dielectric material [60], with a sensitivity of film thickness down to 20nm. The measurements of in-plane and cross-plane thermal conductivities of anisotropic films were also done using this method [61, 62]. Further more, with the development of nanotechnology, the 3ω method has been adapted and applied to study the heat transport in various nanostructured materials, suspended nanowires [63, 1], carbon nanotubes [64], suspended membranes [65, 66, 67], etc.

In the principles of the 3ω method, a transducer metal line is required to be deposited on the surface of the sample material, generally in a four-contact geometry as shown in figure 3.1. It serves as both the heater and the thermometer.

In the experiments, under a working temperature T_0 , an alternating current (AC) of frequency f is applied through the two outer pads of the transducer metal line (shown in figure 3.1):

$$I = I_0 \cos(\omega_e t) \tag{3.1}$$

with ω_e the angular frequency of the AC current ($\omega_e = 2\pi f$), and I_0 the amplitude of the sinusoidal current. Heat is then generated and dissipated via the transducer due to the Joule effect, and a temperature oscillation ΔT is generated at the sample surface, which varies as a

function of $2\omega_e$.

$$\Delta T = \Delta T_0 \cos(2\omega_e t + \phi) \quad (3.2)$$

ΔT_0 and ϕ are the amplitude and phase shift of the temperature oscillation, respectively, which are crucial terms as they are directly related to the thermal properties of the material beneath the transducer.

As a result of this temperature oscillation, the electrical resistance R of the transducer also contains a variation component:

$$R = R_0(1 + \alpha\Delta T) \quad (3.3)$$

with R_0 the electrical resistance of transducer at temperature T_0 , and α the temperature coefficient of the transducer material.

The voltage measured at the two inner pads of the transducer (shown in figure 3.1) then takes the form:

$$\begin{aligned} V &= RI \\ &= [R_0 + R_0\alpha\Delta T_0 \cos(2\omega_e t + \phi)] \cdot I_0 \cos(\omega_e t) \\ &= R_0 I_0 \cos(\omega_e t) + R_0 I_0 \alpha \Delta T_0 \cos(2\omega_e t + \phi) \cdot \cos(\omega_e t) \end{aligned}$$

and as

$$\cos(a) \cdot \cos(b) = \frac{1}{2} [\cos(a + b) + \cos(a - b)] \quad (3.4)$$

$$\begin{aligned} V &= R_0 I_0 \cos(\omega_e t) + \frac{R_0 I_0 \alpha}{2} \Delta T_0 \cos(\omega_e t + \phi) + \frac{R_0 I_0 \alpha}{2} \Delta T_0 \cos(3\omega_e t + \phi) \\ &= V_{\omega_e} + V_{3\omega_e} \end{aligned}$$

So the measured voltage signal contains three terms classified in two harmonic components, V_{ω_e} and $V_{3\omega_e}$. The first term in the V_{ω_e} component contains no information of temperature oscillation, however it presents the most important signal in terms of value, at least 1000 times

Chapter 3. Experimental methods for thermal conductivity measurement

bigger than other two terms. The second term in V_{ω_e} relates to the temperature oscillation (ΔT_0 and ϕ), but practically it is truly difficult to distinguish it from the former term. It is indeed the third harmonic component $V_{3\omega_e}$ that can permit the extraction of the temperature oscillation:

$$V_{3\omega_e} = \frac{R_0 I_0 \alpha}{2} \Delta T_0 \cos(3\omega_e t + \phi) \quad (3.5)$$

It is emphasized that this third harmonic voltage component is at least three orders of magnitude smaller than the first harmonic part, thus electronic methods are indispensable to extract and enhanced this $V_{3\omega_e}$ signal for it to be measured. Then from the measured $V_{3\omega_e}$ signal, the temperature oscillation at the sample surface can be analyzed to study the thermal properties of the sample.

The advantage of this technique is its relatively easy implementation compared to TDTR and SThM, with its originality lying in the fact that both heater and thermometer are realized by one same metal line (the transducer). Moreover, the 3-omega method can be adapted for different sample geometries (from 3D to 1D), permitting measurements of thermal conductivity, or thermal conductance or even heat capacity.

However, the 3-omega method has important drawbacks in its application for thin film characterization. One of the major ones is that this method can be applied only when the thermal conductivity of the thin film material is smaller than that of the substrate material. It refers to an addition of a thermal barrier on to the substrate. Furthermore, the determination of the interface thermal resistances between the film and the substrate needs more measurements of specific samples, and it is time-consuming. Otherwise, approximate values are often employed which can bring important errors to the final results. The requirements on the geometries of the samples for thin film characterization are also very strong, mainly on the thickness of thin films, and its relation with the width, length and thickness of the transducer lines (details will be discussed in the later part of the chapter).

The 3-omega method in 3D geometry

In the simplest case where a line heat source is on a 3D semi-infinite isotropic substrate, the transducer can be approximated as a 1D line source under the condition that the thermal penetration depth (λ) is much larger than the half width of the transducer line (b). Cahill and Paul [58] derived the heat flow profile of the line source to be cylindrical, flowing into the sample volume as shown in figure 3.2. Starting from the heat conduction equation, the amplitude ΔT of the temperature oscillation at a distance $\vec{r}(x, y)$ from the line heat source was first obtained by Carslaw and Jaeger [68]:

$$\Delta T = \frac{P}{l\pi k} K_0(qr) \quad (3.6)$$

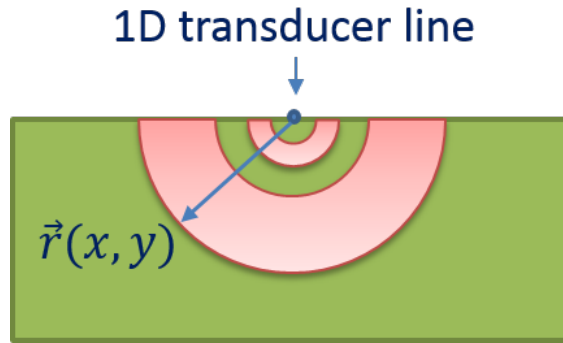


Figure 3.2: Schematic diagram of a cylindrical heat flow from a 1D transducer line into a semi-infinite substrate.

where P/l is the amplitude of the dissipated power per unit length by the transducer due to the Joule effect when applying an AC current of frequency ω_e . k is the thermal conductivity of the substrate underneath the transducer line and K_0 is the zeroth-order modified Bessel function. The complex quantity $1/q$ is the wavelength of the diffusive thermal wave, also known as the thermal penetration depth, defined by:

$$\lambda = \frac{1}{q} = \sqrt{\frac{D}{2\omega_e}} \quad (3.7)$$

where D is the thermal diffusivity of the substrate material, $D = \frac{k}{\rho c_p}$, related to the thermal conductivity k , the density ρ and the specific heat capacity c_p of the substrate. $2\omega_e = \omega_{th}$ is the thermal excitation frequency.

The derived equation 3.6 is valid under the assumptions that: (i) the thickness and the width of the 1D transducer line are negligible, whereas its length is infinite; (ii) the line transducer has no heat capacity and is in perfect contact with the substrate, i.e., there is no thermal boundary resistance between the transducer and the substrate.

The 3-omega method in 1D and 2D geometry

For suspended 1D nanowires, the 3-omega method can be adapted for the measurement of both thermal conductivity and heat capacity of the nanowire. In the case studied by Christophe Blanc in his thesis [1], a transducer line is deposited on a Si nanowire, as shown in figure 3.3. The temperature gradient then has its highest point at the center of the nanowire, and heat flows from the center to the two ends of the wire (the thermal bath).

In this case, under high frequency heating condition, the heat generated in the system does not have time to propagate toward the heat bath. So the temperature of the nanowire stays

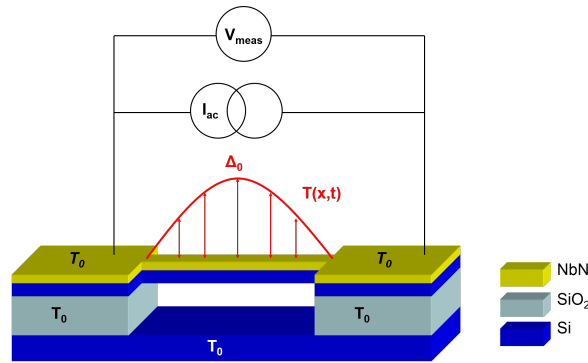


Figure 3.3: Schematic diagram of a suspended nanowire with the transducer line deposited on top for 3ω measurements [1].

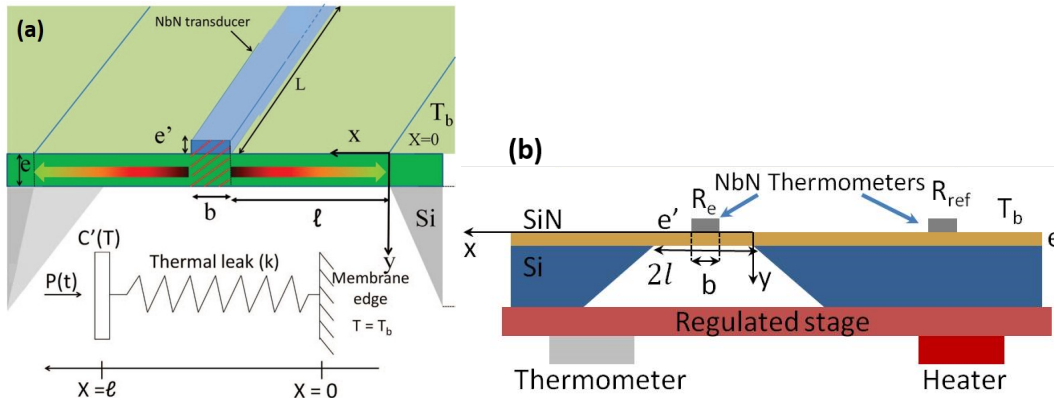


Figure 3.4: Schematic diagrams for the case of a suspended membrane with the transducer line in the center for 3ω measurements: (a) the temperature profile; (b) the sample geometry for the measurement [66].

stable and the signal of $V_{3\omega}$ is related to the heat capacity of the system only. At low frequency, the slow variation of the temperature makes the system sensitive to the propagation of heat, so from the $V_{3\omega}$ signal the thermal conductance can be calculated.

In the case of suspended membranes, the Völklein geometry is coupled with the 3-omega method to measure the in-plane thermal conductivity of the membrane. As studied in the thesis of Hossein Ftouni [67, 66], a transducer is deposited at the center of a SiN membrane (figure 3.4). Heat then propagates from the center to the edges of the membrane (thermal bath). In this case, an identical reference transducer deposited on the same sample but on the bulk region is needed, in order to extract the $V_{3\omega}$ signal from a measurement setup based on a Wheatstone bridge.

The in-plane thermal conductance and heat capacity of the membrane can be obtained from the $V_{3\omega}$. At low frequency, the $V_{3\omega}$ signal is related to the thermal conductance, and

independent of the frequency. Then using the obtained value of thermal conductivity, the heat capacity can be calculated from a fit of $V_{3\omega}$ versus frequency at a higher frequency range.

3.1.2 Time-domain thermo-reflectance

The Time-domain thermal-reflectance (TDTR) is a pump-probe optical technique for the characterization of thermal properties of the material through measurement of changes in the temperature-dependent reflectivity [69, 70, 71]. The time evolution of the surface temperature (i.e. time-domain) is measured through changes in the reflectivity (i.e. the thermo-reflectance). Once a material is heated up, the temperature-dependent change in the optical reflectivity (R_{opt}) of the material is recorded with respect to time:

$$\Delta R_{opt} = \left(\frac{\partial R_{opt}}{\partial T} \right) \Delta T \quad (3.8)$$

From the time-domain reflectivity data the thermal properties of the sample can be interpreted with the help of developed models.

The technique of this method is to use a pulsed laser beam (Gaussian heat source) to locally heat the sample thus induce thermal stress, which then generates acoustic waves at the sample surface. After a delay time, based on the piezo-optic effect a probe laser is used to detect the acoustic waves that are reflected from an interface, which contain the thermal properties of the through-traveled material.

TDTR has a good spatial and time resolution, it is one of the most reliable methods for the measurement of the thermal conductivities of bulk, of thin-film materials (down to hundreds of nanometers thick) [72, 73], and the thermal conductance of interfaces [74]. In thin film measurements, the method is capable of isolating interface thermal conductance from the thermal conductivity of the thin film. The approach permits measurements of thermal conductivities within a large range, and it has been thoroughly validated on a wide range of materials and thin films with known thermal conductivities.

However, the TDTR method has important drawbacks, including: complexity of the equipment and the setup installation, thus vulnerability to errors; low accuracy due to a high dependence on manual skills of the operator; high noise-to-signal ratio especially in high frequencies and etc [75, 76].

3.1.3 Scanning thermal microscopy

Scanning thermal microscopy is a type of scanning probe microscopy developed for local thermal characterization of materials and systems since 1986 [77]. Nowadays it is mainly based on an Atomic Force Microscopy (AFM) configuration. A miniaturized sensitive thermal probe mounted on a cantilever is the essential part of the technique. Different types of SThM probes

Chapter 3. Experimental methods for thermal conductivity measurement

exist using different thermal sensors, including probes with a resistive element [78, 79, 80] and thermocouple probes [81, 82, 83]. In this work, a resistive SThM probe is used in the constant-force and constant-contact modes of AFM.

As shown in figure 3.5, an optical system of detection of the probe deflection is used to adjust and control the force between the probe and sample. Thanks to a mirror at the back of the probe cantilever, as the probe is approaching or scanning the sample surface, the reflection of the laser beam displaces simultaneously on the photodiode. During imaging or measurements, a feedback loop enables to maintain constant the probe-sample force. The piezoelectric element then reacts to adjust the 3D displacement and positioning of the probe. A Wheatstone bridge circuit is integrated with SThM, which constitutes the Thermal Control Unit (TCU). Two modes are available in SThM: Conductivity Contrast Microscopy (CCM) and Temperature Contrast Microscopy (TCM).

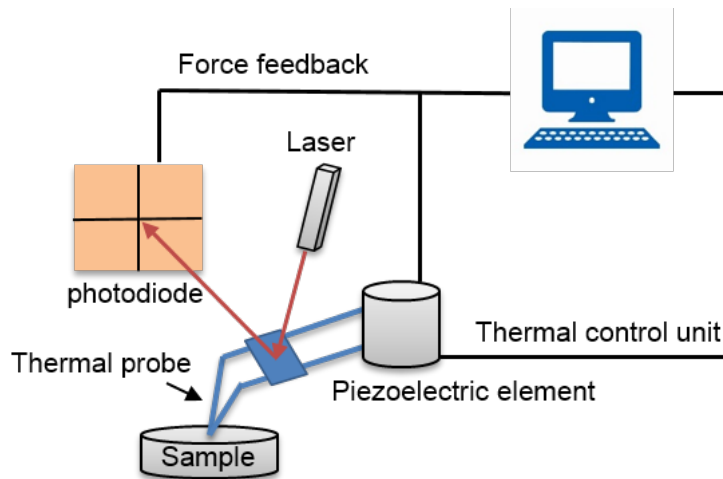


Figure 3.5: Schematic diagram of the principles of a scanning thermal microscopy

In CCM mode, the probe is electrically heated. When the thermal probe is in contact with the sample surface, heat flux goes from the heated tip to the sample causing a decrease of the electrical resistance of the tip. This temperature drop of the tip can be sensed by the Wheatstone bridge thanks to a feedback loop. The bridge voltage is then adjusted to heat more the tip in order to recover its resistance and temperature. In this way the probe is kept at a certain set temperature constantly. This output bridge voltage then represents the thermal properties of the sample.

In TCM mode the tip is firstly put in thermal equilibrium with the sample surface (the same temperature), a variable resistance is adjusted to balance the bridge. Then as the probe scans over the sample surface, its temperature changes, bringing changes in the voltage balance. The voltages are registered and can be used to measure the sample surface temperature when the probe is not heated, and extract the changes of thermal conductivity of the sample surface when the probe is heated.

3.2. Experimental 3-omega setups

Both CCM and TCM modes can be used to generate SThM thermal contrast images.

The tip-sample heat transfer involves different physical mechanisms depending on the type of probe and the sample: tip-to-sample solid-solid conduction, liquid-liquid conduction (water meniscus at the tip), air conduction and radiation. Near-field radiation is often neglected when experiments are performed under ambient conditions, because it is estimated to be less important than other involved thermal mechanisms. The modeling of the heat transfer is often required to extract the absolute thermal conductivity of specific samples, especially for nanostructured sample.

SThM enables thermal measurements and imaging with a micro-nano spacial resolution. Achievable measurements include: surface temperature, thermal conductivity, heat capacity [84], polymer glass transition temperature [85] and etc. The technique permits also time-resolution measurements up to several kHz, depending on the size of the thermal probe. However, it has been proved that the technique had limited resolution for materials of high thermal conductivity [78, 86]. Besides, it also has other important shortcomings: including the dependence on operation manners, vulnerability to environment, and especially the low reliability/repeatability of measurements on nano-structured materials.

Methods	3ω	TDTR	STHM
Cost	Low	High	Medium
Setup installation facility	High	low	Medium
Sensitivity for bulk: high- k	High	High	Low
Sensitivity for bulk: low- k	High	High	High
Sensitivity for thin film: high- k	Low	High	Low
Sensitivity for thin film: low- k	High	High	Medium
Time resolution	10 kHz	MHz	steady-state/kHz
Spacial resolution	macro/micro	micro	micro/nano
Repeatability/reliability	High	High	Medium

Table 3.1: Performance comparison of three main experiment methods for thermal conductivity measurement of both bulk materials and thin films.

A comparison of these three experiment methods (3ω , TDTR and SThM) for thermal conductivity measurements at micro/nano scale, is presented in table 3.1. It compares essentially the cost level, the installation facility, the reliability and the measurement sensitivities for both bulk and thin film materials.

3.2 Experimental 3-omega setups

In this PhD work, we have developed an highly-sensitive experimental instrumentation based on the 3-omega method, for precise measurements of thermal conductivity of electrically conductive epitaxial thin films. All experiments were carried out at room temperature (RT) for the analysis of thermoelectric properties (ZT value) of the Ge:Mn thin films for RT application.

3.2.1 Principles for semi-infinite substrate with a finite-width transducer

Following the 3D geometry in 3-omega method, as the transducer has always a finite width, several approximations have been considered to deduce the temperature oscillation at the sample surface:

- (1) the length l of the transducer must be much longer than its width $2b$, that $l \gg 2b$, and the width must be constant along the length;
- (2) the thermal penetration depth λ must be much smaller than the thickness d of the studied substrate, that $\lambda \ll d$ [87]. And according to the analysis carried out by T. Borca-Tasciuc [88], $\lambda \ll \frac{1}{5}d$ is suggested to keep a good agreement (error within 1%) between the normalized slope value (of the curve $\Delta T(\ln \omega)$) and the exact expression;
- (3) the thickness of the transducer is negligible facing the thickness of the substrate.

In our case, all above conditions are fulfilled with the fact that: sample substrates (either Ge or GOI) are generally much thicker ($\sim 500 \mu\text{m}$) than the transducer line ($\sim 100 \text{nm}$); the aspect ratio of the transducer line is: $l : 2b \approx 67 : 1$. For the second condition, as our substrate is in general more than $500 \mu\text{m}$ thick, we would stay within the measurement frequency range which fulfills the condition $\lambda < 100 \mu\text{m}$.

As described by D. Cahill [87], for a finite-width transducer line, the Fourier transform (in k space) of equation 3.6 has been used, and only the temperature oscillation at the sample surface are considered, so that:

$$\Delta T(k) = \frac{P_l}{2k} \frac{1}{\sqrt{(k^2 + q^2)}} \quad (3.9)$$

And the profile of the heat flux is assumed to take a rectangular function:

$$q(x) = \begin{cases} q_0 & \text{if } -b < x < b \\ 0 & \text{if not} \end{cases} \quad (3.10)$$

Fourier transform of this heat flux is used, and the amplitude of the temperature oscillation ΔT is an average of the temperature rise in the transducer:

$$\Delta T = \frac{1}{2b} \int_{-b}^b T(x) dx \quad (3.11)$$

So the convolution of ΔT in the real space (x space) gives:

$$\Delta T(x) = \frac{P_l}{\pi k} \int_0^\infty \frac{\sin^2(kb)}{(kb)^2 \sqrt{(k^2 + q^2)}} dk \quad (3.12)$$

However, this integration has no direct solution. And D. Cahill proposed the separation of the frequency regimes, and to stay in the regime where the thermal penetration depth is much larger than the half width of the transducer line. So that two frequency regimes are defined by comparing the half width b of the transducer line to the thermal penetration depth λ :

Low frequency regime: $\lambda \gg b$

High frequency regime: $\lambda \ll b$.

Thus in the low frequency regime, the temperature oscillation at the sample surface can be approximated as :

$$\Delta T = \frac{P_l}{\pi k_0} \left(-\frac{1}{2} \ln \frac{\omega}{\Omega} + \eta - i \frac{\pi}{4} \right) \quad (3.13)$$

where P_l is the linear heat dissipation power, $P_l = \frac{R_t r I^2}{l}$, with $R_t r$ the electrical resistance, I the applied AC current and l the length of the transducer; $\Omega = \frac{k_0}{\rho C b^2}$ with k_0 the thermal conductivity of the substrate, ρ the density, C the specific heat and $\eta = 0.9228$ being a constant.

From the solution it can be noticed that, both the frequency-dependent contribution in the real part and the constant imaginary part of ΔT , can help to determine the thermal conductivity of the sample substrate. But experimentally, it is considered more reliable the data from the real part contribution [87].

As described previously, the real part of the temperature oscillation and the real part of the $V_{3\omega}$ signal are related via:

$$V_{3\omega-real} = \frac{1}{2} R I \alpha \Delta T_{real} \quad (3.14)$$

So the thermal conductivity of the sample substrate k_0 can be calculated through the equation:

$$k_0 = -\frac{\alpha R^2 I^3}{4\pi l} \left(\frac{dV_{3\omega-real}}{d \ln \omega} \right)^{-1} = -\frac{1}{2\pi l} \left[\frac{d \left(\frac{\Delta T_{real}}{P} \right)}{d \ln \omega} \right]^{-1} \quad (3.15)$$

where $\frac{d \left(\frac{\Delta T_{real}}{P} \right)}{d \ln \omega}$ is the slope of a linear fit of the curve $\frac{\Delta T_{real}}{P}$ as a function of $\ln \omega$ within the concerned low frequency regime.

3.2.2 Differential 3-omega method for film-on-substrate system

Ever since, the 3-omega method has been widely used for thermal measurements on various materials: from bulk to, later on, thin films. The differential 3-omega method has been

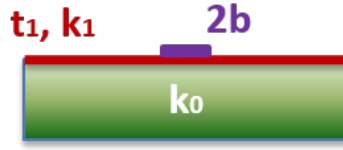


Figure 3.6: Schematic illustration of the profile of a film-on-substrate sample

developed by Cahill in 1994 [59] for film-on-substrate material systems. It is then considered as one of the most powerful methods for thermal measurements of complex 2D systems, especially multilayer samples.

In the differential method, for sample substrates containing a single layer (figure 3.6), under the conditions that the thin film material is less thermal conductive than the substrate, and the thickness of the thin film (t_1) is much smaller comparing to the width of the transducer ($2b$), the heat transport is considered to be only vertical across the film and the heat flux conserved [89, 88, 90, 44].

As a model, the thin film is considered as a thermal barrier resistance R' for the heat flux. It then brings a frequency-independent shift in the real part of the surface temperature oscillation signal deduced previously:

$$\Delta T = \frac{P_l}{\pi k_0} \left(-\frac{1}{2} \ln \frac{\omega}{\Omega} + \eta - i \frac{\pi}{4} \right) + \frac{P_l R'}{2b} \quad (3.16)$$

And if normalized by the dissipated heat power, this shift takes the form of:

$$\Delta \left(\frac{\Delta T}{P_l} \right) = \frac{R'}{2bl} \quad (3.17)$$

This thermal barrier resistance R' is directly related to the thermal conductivity of the thin film through the formula:

$$R' = \frac{t_1}{k_1} + R_c \quad (3.18)$$

where R_c is the effective interface thermal resistance, being the total interface thermal resistance of the thin film sample minus the total one of the sample substrate case.

The obtained thin film thermal conductivity k_1 is, strictly speaking, the cross-plane thermal conductivity. In the case of Ge:Mn thin films, which are isotropic as presented in chapter 2, the obtained cross-plane thermal conductivity is thereby the thermal conductivity of Ge:Mn.

3.2.3 Thermometry

The material of transducer is required to be a resistive thermometric material. Different materials have been considered and tested, including the common thermometric metal gold and platinum, and the unique thermometric material niobium nitride, which has been under development in our laboratory for more than ten years.

For a niobium nitride thermometer, with a negative temperature coefficient its electrical resistance decreases with the temperature raise. This makes it a very sensitive thermometer at low temperature. Depending on the stoichiometry, it can be tailored for the use within a large range of temperature, from RT down to 10 kelvins. At room temperature, the temperature coefficient of NbN has a order of magnitude of 0.1 K^{-1} , and the electrical resistance can be as high as $100 \text{ K}\Omega$.

For metal transducers such as gold and platinum, they have a positive temperature coefficient, and in general the relation between the electrical resistance and the temperature saturates at around 30 kelvin. For platinum thermometer, the temperature coefficient is much smaller than NbN, being around $0.3 \times 10^{-2} \text{ K}^{-1}$ at room temperature. Meanwhile, its electrical resistance is much less important than NbN also, of only hundreds of ohm.

In the work of this thesis, as the study of the thermoelectric properties of this Ge:Mn material aims at potential applications at room temperature, only room temperature 3-omega measurements are predicted. In order to have the signal of $V_{3\omega}$ sufficiently big to be detected (in the order of mV after a magnification of 1000), the dissipated heat through the transducer is required to be several mW. So that for a platinum heater (100Ω in resistance) the required heating voltage is in the range of 0.3V to 1V, whereas for a NBN heater ($100 \text{ K}\Omega$) a voltage source of superior than 10V (up to 30 V) is required, which is difficult to achieve in a laboratory working environment. Hence, the platinum transducer was chosen to do the work.

Standard micro-fabrication processes involving UV lithography and Magnetron sputtering deposition, were applied to deposit the platinum transducer on the sample surface. In the magnetron sputtering process, a target plate is bombarded by energetic ions generated in a plasma situated in front of the target. The bombardment causes the removal of target atoms, which may then condense on a substrate as a thin film. The thickness of the Pt transducer line is 100 nm. With a designed width of $30 \mu\text{m}$ and a length of 2 mm in the geometry shown in figure 3.1, the electrical resistance of the transducer line is around 100Ω , at 300K.

The deposited transducer must be calibrated in vacuum within the working temperature range before all measurements. In this experiment, the sample is stuck to the sample holder using a resin. Thanks to a heating resistance and a standard commercial platinum thermometer (for RT application) stuck at the side of the sample holder, the temperature is estimated and controlled. The sample holder is then mounted in a cryostat, pumped and connected with the electronic devices through cables. For the transducer calibration, the electrical resistance variation of the Pt transducer as a function of temperature (within 280-320 K) is registered,

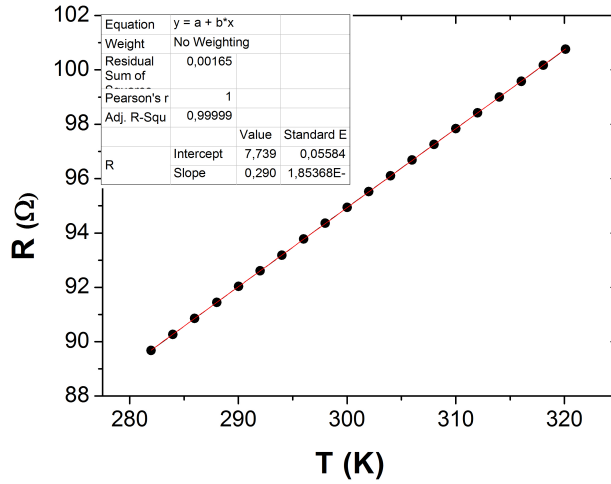


Figure 3.7: Calibration curve (dotted black line) of a Pt transducer showing the evolution of its electrical resistance as a function of temperature in RT range; the straight red line is the linear fit of the experimental curve.

applying a current of 1 mA. The slope of this R(T) curve permits the calculation of the temperature coefficient α , which represents the sensitivity of the transducer as a thermometer. α is given by:

$$\alpha = \frac{1}{R} \frac{dR}{dT} \tag{3.19}$$

A typical calibration curve of Pt transducer in the work is shown in figure 3.7.

The precision of the temperature coefficient α is very crucial for the sensibility of the determination of sample substrate's thermal conductivity k_0 as described in formula 3.15. Thus in this work, it's decided to always take five effective numbers for the value of α obtained from the calibration for each transducer.

3.2.4 Introduction of insulating layer for electrical conductive thin films

For the case of electrical conductive thin film on a semi-infinite substrate, an insulating thin layer is required on top of the sample before the deposition of transducer to electrically isolate the transducer metal line and the conductive thin film sample (figure 3.8). Different oxides can be considered, among which SiO₂ and Al₂O₃ are mostly used. In this work, the Al₂O₃ layer deposited by Atomic Layer Deposition (ALD) is chosen to serve as the insulating layer [91].

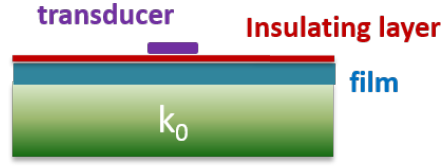


Figure 3.8: Schematic illustration of the profile of a film-on-substrate sample with an insulating layer.

In this case, the effective interface thermal resistance R_c can be written as:

$$R_c = (R_{metal/oxide} + R_{oxide/film} + R_{film/sub.}) - (R_{metal/oxide} + R_{oxide/sub.}) \quad (3.20)$$

As for our Ge:Mn thin film samples grown on germanium (in layer within GOI or bulk) substrates, with platinum transducer and Al_2O_3 insulating layer, R_c can be deduced as:

$$R_c = (R_{Pt/Al_2O_3} + R_{Al_2O_3/Ge:Mn} + R_{Ge:Mn/Ge}) - (R_{Pt/Al_2O_3} + R_{Al_2O_3/Ge}) \quad (3.21)$$

As the thin film of Ge:Mn is grown from the Ge substrate using MBE, the germanium matrix of Ge:Mn thin film is proved to be perfectly crystalline as its Ge substrate. So that the interface thermal resistance between Al_2O_3 and Ge is considered to be equal to the one between Al_2O_3 and Ge:Mn:

$$R_{Al_2O_3/Ge:Mn} \cong R_{Al_2O_3/Ge} \quad (3.22)$$

So that:

$$R_c = R_{Ge:Mn/Ge} \quad (3.23)$$

The value of this interface thermal resistance between the epitaxial Ge:Mn and Ge, $R_{Ge:Mn/Ge}$, is down to the order of $10^{-9} \text{ Km}^2\text{W}^{-1}$ [60, 92]. So R_c is determined to be:

$$R_c \approx 10^{-9} (\text{Km}^2\text{W}^{-1}) \quad (3.24)$$

In the work, different thicknesses of Al_2O_3 layers have been tested. The objective is to achieve a perfect insulation result using the thinnest layer possible. Al_2O_3 layers of 20nm, 50nm and 100nm have been deposited on GaAs substrates. After the deposition of metal contacts, the efficiency of electrical insulation of the oxide layer can be tested using simply a multimeter.

Chapter 3. Experimental methods for thermal conductivity measurement

The test results showed that with the layer of 20nm, the isolation condition was not obtained, and random existence of dust on the sample surface may disturb importantly the insulation efficiency. As a consequence, the thickness of the insulating Al_2O_3 layer has been decided to be 50nm.

3.2.5 Experimental setups

To realize the measurements using the $V_{3\omega}$ technique, facing the fact that the $V_{3\omega}$ signals are at least three orders of magnitude smaller comparing to the first harmonic part V_ω , two types of setups have been considered: the differential method and the Wheatstone bridge. Principles of the both methods are to cancel the V_ω part of signal with the help of a variable pure resistance (as a reference resistance for the transducer on sample), then to enable the amplification of the signal $V_{3\omega}$ so that it can be measured using a lock-in amplifier.

Setup with differential method

The differential method is very much used for complex sample systems including 1D, 2D and super lattice samples [87, 59]. As shown in the diagram of electrical circuit (figure 3.9), a home-made differential electronic device is used [91]. The pure resistance R_{ref} (highly stable with temperature and precise to 0.001 Ω) is adjusted to have the same value of resistance as the transducer line on top of the sample at the working temperature. Once applying an AC current, the V_ω signal from this R_{ref} is used to subtract the same quantity of V_ω from the sample transducer. The 3ω component from the sample can then be extracted, amplified 1000 times by a pre-amplifier and finally acquired by a digital lock-in amplifier. The AC current is generated at a frequency ordered by the lock-in amplifier. With the help of the LabVIEW platform, the signals of the $V_{3\omega}$ at different frequencies within a chosen range are registered, both the magnitude and the phase.

The lock-in amplifier used in the experiments is the signal recovery model 7230 DSP fabricated by Ametek. The variable resistance R_{ref} is the programmable resistance substituter model IEEE-4858 by IET, with a precision to 0.001 Ω . The thermal conductivity of the substrate can be calculated from the frequency dependence of the $V_{3\omega}$ using equation 3.15.

Setup with Wheatstone bridge

Another method to realize 3ω measurements is by using a Wheatstone bridge. With the help of an extra fixed resistance R_0 , connected in the circuit as shown in figure 3.10, the 1ω component from the sample transducer can also be subtracted, and the $V_{3\omega}$ extracted. In this case, pre-amplified or not, the small signal of $V_{3\omega}$ (around μV in our cases) can already be detected by the lock-in amplifier.

In our experiments no pre-amplifier is used, and the current in the circuit is generated by an

3.2. Experimental 3-omega setups

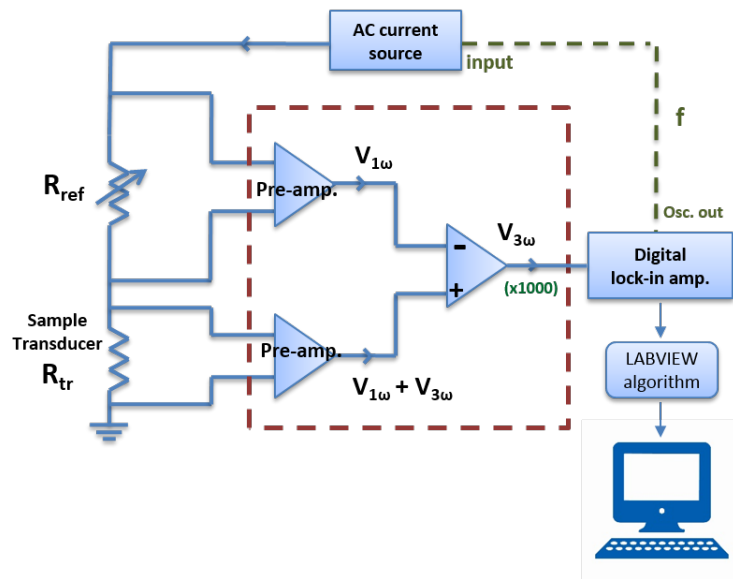


Figure 3.9: Schematic diagram of the electrical circuit for a 3ω measurement setup using differential method.

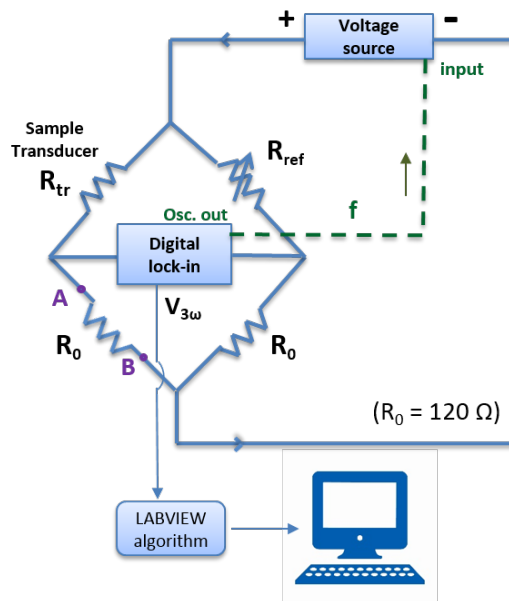


Figure 3.10: Schematic diagram of the electrical circuit for a 3ω measurement setup using Wheatstone bridge.

ultra low distortion function generator (model DS360, Stanford research system). The current in the transducer is then calculated from the voltage measured at the sides of the transducer (V_{AB} in the figure): $I = V_{AB}/R_0$. The R_0 is chosen to be 120Ω as our transducer has a resistance

of around 100 Ω at RT in general cases.

In this Wheatstone bridge method, attention should be paid to the modification of the equation 3.15 for the thermal conductivity calculation of the sample substrate:

$$k_0 = -\frac{\alpha R_{tr}^2 I^3}{4\pi l} \left(\frac{dV_{3\omega-real}}{d\ln\omega} \right)^{-1} \frac{R_0}{R_{ref} + R_0} \quad (3.25)$$

3.2.6 Validation of setups on test samples

In order to verify the performance of the two mounted setups, measurements on test samples have been performed. GaAs substrate, a good electrical insulator having a value of thermal conductivity close to that of Ge bulk, has been chosen as the test substrate for both semi-infinite system and film-on-substrate system.

Tests on GaAs sample

The 3ω measurements on an intrinsic GaAs substrate were carried out using both the differential setup and the Wheatstone bridge setup. The thickness of the sample was around 0.5 mm. By calculating the thermal penetration depth into the GaAs, whose thermal diffusivity is $2.58 \times 10^{-5} \text{ m}^2 \text{ s}^{-1}$, the working electrical frequency (f) was decided to be a range between 50 – 1500 Hz. Once the reference resistance is adjusted to the same value of the calibrated transducer, before the frequency dependence measurements of $V_{3\omega}$, the signals $V_{3\omega}$ were registered applying different currents, from 1 to 7 mA in general, to verify if the $V_{3\omega}$ is indeed in linear relation with the cubic current, obeying:

$$V_{3\omega} = AI^3 \quad (3.26)$$

Conditions are considered proper for further measurements only when this linearity is obtained, as shown in figure 3.11.

From the data of the $V_{3\omega}$ signals (magnitude and phase) as a function of frequency (in $\ln\omega$ where $\omega = 4\pi f$), both the real part and the imaginary part of $V_{3\omega}$ can be calculated. In figure 3.12, from both the differential method setups and the Wheatstone bridge, measurement curves of $V_{3\omega}(\ln\omega)$ by applying different currents (in different colors) are plotted, and normalized with respect to the curve obtained with 4 mA. The fact that all those curves overlap after normalization, confirms the linear relation of $V_{3\omega}(I^3)$. From the graphs, one can clearly observe a linear behavior of the real part signal of $V_{3\omega}$ as a function of $\ln\omega$, in both setups, which permits the calculation of the thermal conductivity of the GaAs substrate in both methods using their corresponding formula (equation 3.15 or 3.25). The obtained values of thermal conductivity of GaAs are within the range of $46\text{-}48 \text{ Wm}^{-1}\text{K}^{-1}$ at 300K, for both methods, which are in agreement with the literature.

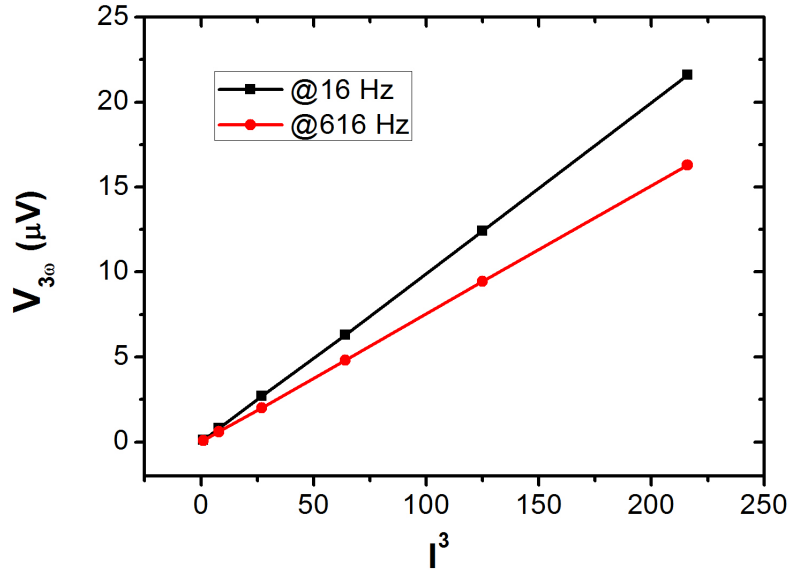


Figure 3.11: Experimental graph showing the linear relation between the $V_{3\omega}$ and the cubic current on test sample GaAs using the differential method.

It is worth noticing that, by comparing the $V_{3\omega}(\ln \omega)$ curves at 4 mA from both the differential setup and the Wheatstone bridge (figure 3.13), the factor $\frac{R_0}{R_{ref}+R_0}$ associated with the Wheatstone bridge (equation 3.25) was confirmed by the signal difference between the two curves. And as it can be noticed that the signals from the differential method are clearer than that from the Wheatstone bridge method, especially regarding the divergence at higher frequencies for the case of Wheatstone bridge. Accordingly, the setup based on the differential method was selected for the following tests and all the measurements.

Tests on Al_2O_3 -on-GaAs sample

To validate the film-on-substrate model in the 3-omega method, measurements were carried out on a test sample of GaAs substrate containing on top a thin layer of Al_2O_3 (50 nm) deposited by ALD, as illustrated in figure 3.14. The signals of $V_{3\omega}$ as a function of frequency from this sample were registered. Then the real part of the temperature oscillation signals from both the sample GaAs substrate (tested precedently) and the Al_2O_3 /GaAs sample, were calculated and plotted as a function of $\ln \omega$. The comparison of these two temperature oscillation curves obtained applying an AC current of 4 mA is presented in figure 3.15. This clearly shows that there is a vertical shift between the two curves, whereas the slope of the curve is conserved.

According to the theories previously discussed, with the value of this vertical shift from the curve of substrate GaAs to the one of the sample Al_2O_3 /GaAs, the equation 3.17 and equation

Chapter 3. Experimental methods for thermal conductivity measurement

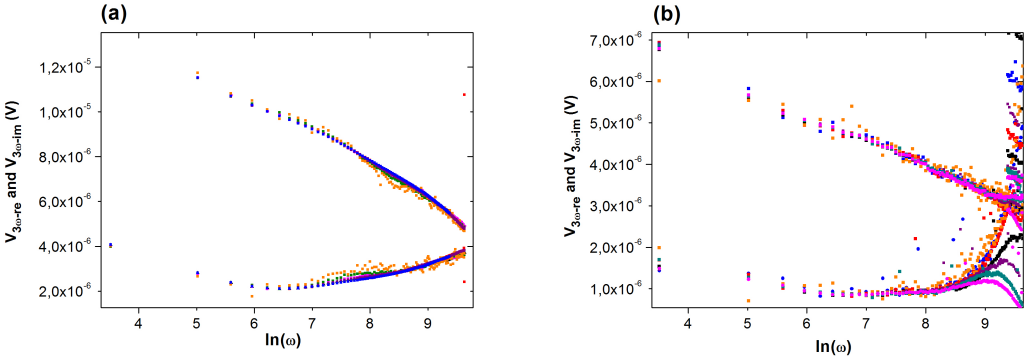


Figure 3.12: Experimental curves of signal $V_{3\omega}$ from test sample GaAs substrate using: (a) differential method; (b) Wheatstone bridge.

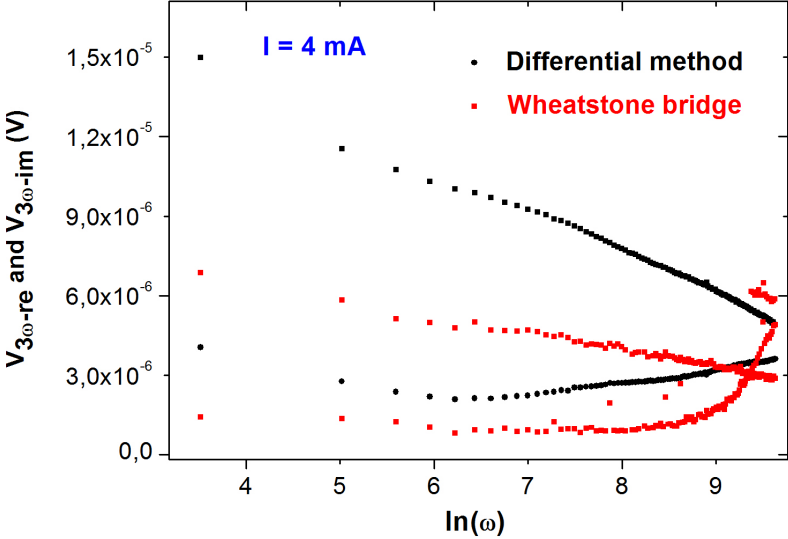


Figure 3.13: Comparison of the experimental curves at 4 mA on sample GaAs using differential method and Wheatstone bridge.

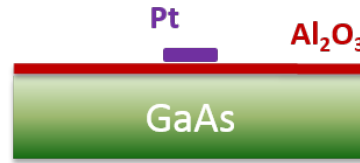


Figure 3.14: Illustration of the cross view of a test sample containing a thin layer of Al_2O_3 (50 nm) on top of a GaAs substrate. The Pt transducer is deposited on the oxide layer.

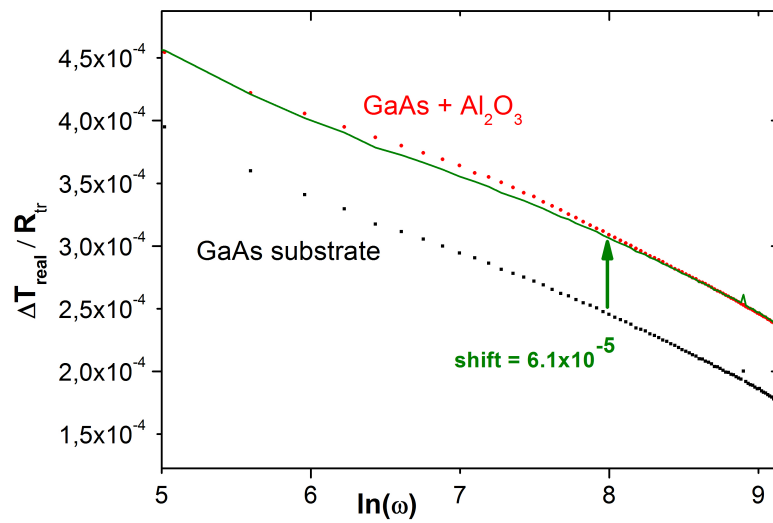


Figure 3.15: Curves (the real part) of the temperature oscillation signals as a function of frequency ($\ln \omega$) recorded from both the GaAs substrate sample and the $\text{Al}_2\text{O}_3/\text{GaAs}$ test sample, applying an AC current of 4 mA. The curves show the same slope, while a vertical shift is observable between them, which permits the calculation of the thermal conductivity of the Al_2O_3 layer.

3.18 were applied to calculate the thermal conductivity of the Al_2O_3 thin film. The effective thermal contact resistance in this case is identified as:

$$R_c = R_{\text{Pt}/\text{Al}_2\text{O}_3} + R_{\text{Al}_2\text{O}_3/\text{GaAs}} - R_{\text{Pt}/\text{GaAs}} \approx 10^{-8} \text{Km}^2\text{W}^{-1} \quad (3.27)$$

Then with the other parameters as: $2b = 30\mu\text{m}$, $l = 2\text{mm}$ and $t_1 = 50\text{nm}$, the thermal conductivity of this Al_2O_3 thin film is calculated to be $0.87 \text{Wm}^{-1}\text{K}^{-1}$. This value is consistent with the literature [93, 94].

3.2.7 Analysis of error and sensitivity of 3ω measurements

Error analysis of the determination of substrate thermal conductivity k_0

According to equation 3.15, the substrate's thermal conductivity is calculated via:

$$k_0 = -\frac{1}{2\pi l} [Slope]^{-1} \tag{3.28}$$

Here "Slope" is used to represent $\frac{d\left(\frac{\Delta T_{real}}{P}\right)}{d\ln\omega}$.

To process error analysis of the "Slope", experimental curves of $\Delta T/P$ as a function of $\ln\omega$ measured at different currents from sample S8 (Ge:Mn 240 nm on n-type Ge substrate) are used. As shown in figure 3.16, the values of the maximum and minimum slopes of the linear fitting of the $\Delta T/P$ curves permit the calculation of the slope error:

$$\frac{\Delta\langle Slope \rangle}{\langle Slope \rangle_{mean}} = \frac{1.293 - 1.244}{(1.293 + 1.244)/2} \approx 3.9\% \tag{3.29}$$

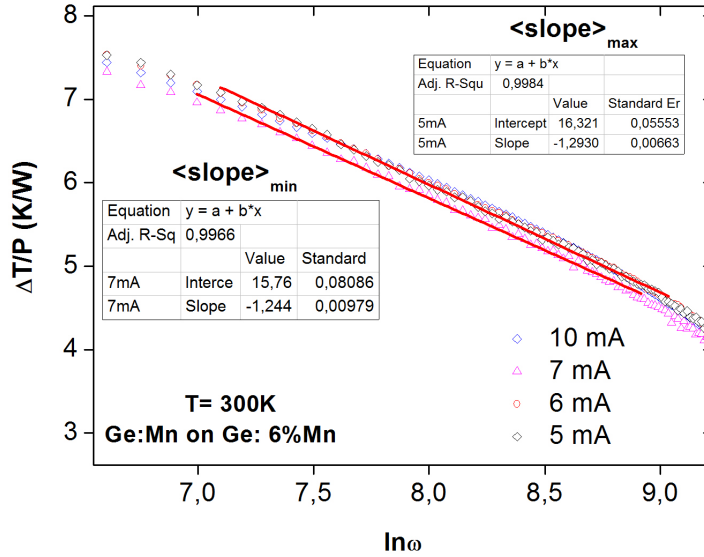


Figure 3.16: Experimental curves of $\Delta T/P$ as a function of $\ln\omega$ measured at different currents from sample S8 (Ge:Mn 240 nm on n-type Ge substrate). The maximum and minimum values of the slope of the $\Delta T/P$ curves are identified for the analysis of the slope error in the 3-omega measurements.

The slope error is mainly attributed to the error in temperature coefficient α . The error of the calculated thermal conductivity of the substrate is then the addition of the slope error and the error of the transducer length:

$$\frac{\Delta k_0}{k_0} = \frac{\Delta l}{l} + \frac{\Delta \langle Slope \rangle}{\langle Slope \rangle_{mean}} = \frac{(2 - 1.98)\text{mm}}{2\text{mm}} + 3.9\% = 4.9\% \quad (3.30)$$

This error of 4.9% applies to all measurement results on substrate thermal conductivity.

Error analysis of the determination of thin film thermal conductivity k_1

For the characterization of thermal conductivity of a thin film, a temperature oscillation shift (referred to as "Delta" in the following analysis) is identified and used in the calculation as described in equation 3.17. Following equation 3.17 and equation 3.18, the thermal conductivity of the thin film k_1 is calculated from:

$$k_1 = \frac{t_1}{\langle Delta \rangle \cdot 2b \cdot l - R_c} \quad (3.31)$$

As the first term in the denominator has a value of around 10^{-8} , and the R_c for Ge:Mn/Ge case has an order of magnitude of 10^{-9} , the later term had then been neglected in the following error estimation. For the error of the shift "Delta", as it concerns a subtraction between two curves of $\Delta T(\ln \omega)$, the error for the "Delta" is twice the "slope" error that has been analyzed above.

The error of k_1 can then be analyzed as:

$$\begin{aligned} \frac{\Delta k_1}{k_1} &= \frac{\Delta t_1}{t_1} + \frac{\Delta l}{l} + 2 \times \frac{\Delta b}{b} + \frac{\Delta \langle Delta \rangle}{\langle Delta \rangle_{mean}} \\ &= \frac{1\text{nm}}{100\text{nm}} + \frac{(2 - 1.98)\text{mm}}{2\text{mm}} + 2 \times \frac{(30.69 - 30)\mu\text{m}}{30\mu\text{m}} + 2 \times \frac{\Delta \langle Slope \rangle}{\langle Slope \rangle_{mean}} \\ &= 1\% + 1\% + 2 \times 2.3\% + 2 \times 3.9\% = 14.4\% \end{aligned}$$

This error of 14.4% should then be applied to all measurement results on film-on-substrate samples in the work, that will be presented in the following chapters.

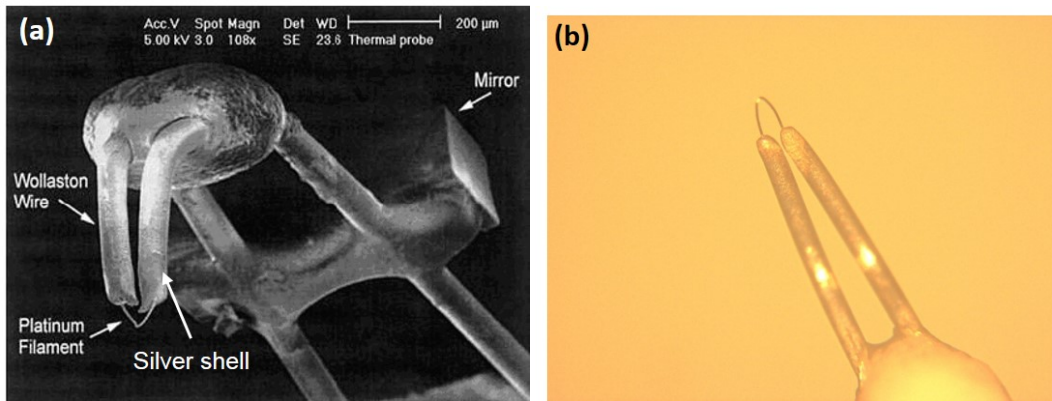


Figure 3.17: (a) Scanning electron microscopy image of the Wollaston probe showing the composition of a Pt/Rh filament, the silver shell around the filament, and a mirror at the top of the wire arms; (b) Optical microscope image of the tip of a Wollaston probe used in the work.

3.3 Scanning Thermal Microscopy (SThM)

The SThM experiments on Ge:Mn samples have been carried out at the Centre d’Énergétique et de Thermique de Lyon (CETHIL). The SThM equipment used in this work is a system from ThermoMicroscopes, Autoprobe, CP-Research. Commercial Wollaston thermal probes were used for all measurements.

3.3.1 Principles for thermal conductivity measurement

The Wollaston probe is a bended Pt 90%/Rh 10% wire coated by a silver shell. The tip of the probe is a Pt/Rh resistive element shaped in "V", obtained by electrochemical etching of the silver shell. The Pt/Rh wire is 5 μm in diameter and 200 μm in length (L). As shown in figure 3.17(a), similar to an AFM tip, the cantilever of the Wollaston probe carries a mirror at the back, which reflects the laser beam to help to adjust the position and force between the tip and the sample with the help of the force feedback loop and the piezoelectric support.

In our experiments we have used the Conductivity Contrast Mode (CCM) of SThM. In this mode the resistive element of thermal probe is used as a heater. As shown in figure 3.18, the Wheatstone bridge is composed of two fixed resistances and one variable resistance R_v , integrated with a detection system which helps to adjust the bridge voltage to adjust the probe temperature simultaneously.

When the probe is out of contact with the sample (in air), the voltage at the probe required to keep the set temperature is noted as V_{out} . As the heated probe contacts the sample surface, heat flows from the probe to the sample, resulting in the cooling of the probe and a decrease of the electrical resistance of the probe. The feedback loop senses this change and adjusts the bridge voltage (V_{AB}) to restore the probe’s resistance (thus temperature) to its preset value.

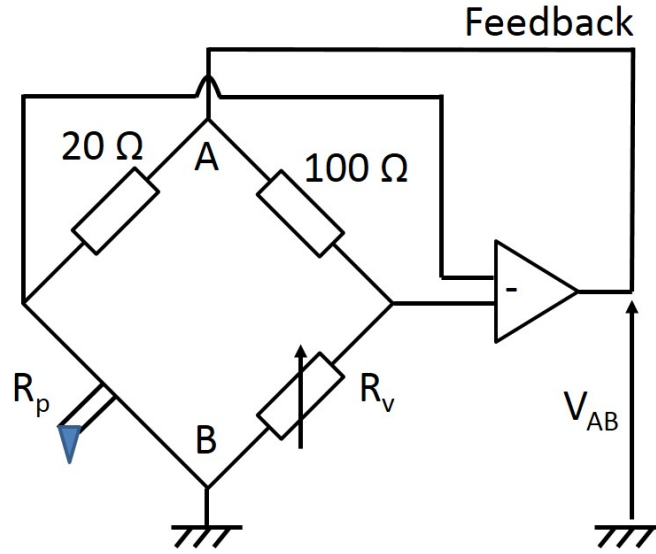


Figure 3.18: Schematic diagram of the CCM mode in SThM with a feedback circuit added to the Wheatstone bridge. In our experiments the two fixed resistances are 100Ω and 20Ω. R_p is the total probe resistance and R_v refers to a variable resistance that is required to balance the bridge.

The probe voltage now is V_{in} . As the heating of the sample surface by the tip is extremely local, the temperature of the sample mass remains unchanged so that the changes in heat flow result only from changes in thermal conductivity of the sample. So the energy (voltage V_{in}) required to maintain the reset temperature when the probe is in contact with sample, can be used to extract the thermal conductivity of the sample.

The total resistance of a Wollaston probe is R_p in the discussion, and the resistance of the Pt/Rh tip is R_{tip} . The commercial Wollaston probes we used are supplied with the parameters of: $R_{tip}=1.9353 \Omega$ at RT, and the temperature coefficient $\alpha = 1.66 \times 10^{-3} \text{ K}^{-1}$.

As the probe needs to be heated in the CCM mode, its total resistance R_p can be written as:

$$R_p = R_{tip}(1 + \alpha\Delta T) + R_{connection} \quad (3.32)$$

where the sum of resistance $R' = R_{tip} + R_{connection}$ at RT can be obtained by a simple measurement using a multimeter.

The heating of the probe is also required to eliminate the water meniscus adhesion [95, 96]. For this purpose, in our experiments, the tip is heated to keep a 100 °C temperature difference with the ambient temperature, so that:

$$\Delta T = T_p - T_{amb.} = 100 \quad (3.33)$$

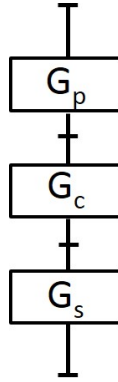


Figure 3.19: Schematic diagram of the thermal conductance network of the in-contact probe-sample system in STHM experiments.

According to the Wheatstone bridge relation $\frac{R_v}{R_p} = \frac{100}{20}$, the variable resistance can then be calculated:

$$R_v = 5R_p = 5 [R_{tip}(1 + \alpha\Delta T) + R_{conn.}] \quad (3.34)$$

In our experiments, R_v has often a value of around 20 Ω .

The voltages at the sides of the probe are measured and recorded when the probe is in-contact (V_{in}) and out-of-contact (V_{out}) with the sample. Multiple measurements can be done in order to obtain mean values of V_{in} and V_{out} for the purpose of precision. The comparison of the heat dissipation (P) of the probe when in-contact (P_{in}) and out-of-contact (P_{out}) with the sample can be done through the calculation of $\frac{\Delta P}{P}$:

$$\frac{\Delta P}{P} = \frac{P_{in} - P_{out}}{P_{in}} = \frac{V_{in}^2 - V_{out}^2}{V_{in}^2} \quad (3.35)$$

For the Wollaston probe, the $\frac{\Delta P}{P}$ is expressed as a function of various parameters: the sample conductance G_s , the probe conductance G_p , the probe-sample contact conductance G_c , as shown in figure 3.19. It can be written as:

$$\frac{\Delta P}{P} = F(G_s, G_p, G_c, h) \quad (3.36)$$

where the factor h is a heat transfer coefficient, which defines the heat losses from the probe to the environment, through mechanisms of convection, conduction and radiation. When the dimension goes down to micro-scale, it has been proved that the heat convection becomes smaller as the buoyancy force decreases, thus the heat loss to the environment is mainly due

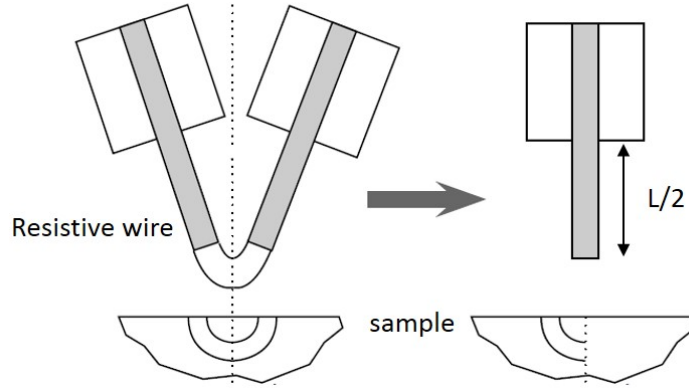


Figure 3.20: Schematic diagram of the Lefèvre model to solve the probe-sample system problem in SThM experiments [98].

to the mechanism of conduction. In this case, according to the evaluation of h carried out by Chapuis [97], the factor h for a Wollaston probe is estimated to be around $3000 \text{ Wm}^{-2}\text{K}^{-1}$. As in our case with a temperature different of $100 \text{ }^\circ\text{C}$ between the probe and the environment, the heat convection is negligible compared to conduction, thus the value $h = 3000 \text{ Wm}^{-2}\text{K}^{-1}$ is taken into account.

The probe conductance G_p is calculated via [98, 99]:

$$G_p = \frac{k_p S}{L} \quad (3.37)$$

where k_p , S and L are respectively the thermal conductivity, section and the total length of the resistive Pt/Rh wire of the probe.

Consider the heat source (probe-sample thermal contact surface) as an isoflux circular area, the sample conductance G_s can be described by the sample thermal conductivity k and an equivalent radius of thermal exchange between the tip and the sample b , through [100]:

$$G_s = \frac{3\pi^2}{8} b k \quad (3.38)$$

b represents the equivalent radius of the thermal contact area between the tip and sample, in a circular form. It takes into account all heat transfer mechanisms between the tip and the sample. Ali Assy [101] has recently shown in his PhD work that $b = b_{air}$, where b_{air} is a parameter of the thermal exchange through air. It is revealed that thermal exchange through air is dominant for Wollaston probes.

To analyze the probe-sample system, according to the model proposed by Lefèvre [98] as

Chapter 3. Experimental methods for thermal conductivity measurement

Reference samples	SiO ₂	ZrO ₂	Ge
k (Wm ⁻¹ K ⁻¹) @ RT	1.2	2.5	58.6
Uncertainty	5%	10%	2%

Table 3.2: List of calibration samples used in our SThM experiments (the values of thermal conductivity and of the uncertainty are given by the material supplier NEYCO).

shown in figure 3.20, the heat equation can be written as:

$$\frac{\partial^2 \theta}{\partial x^2} - \frac{hp}{kS} \theta + \frac{\rho I^2}{kS^2} (1 + \alpha \theta) = \frac{1}{a} \frac{\partial \theta}{\partial t} \quad (3.39)$$

where p and ρ are respectively the perimeter and electrical resistivity of the Pt/Rh tip; $\theta = T - T_{amb}$. and it is assumed that $\theta = 0$ at $x = 0$; the term $(1 - \alpha \theta)$ can be replaced by $(1 - \alpha \bar{\theta})$ in a first approximation.

In DC regime (probe heated by a DC current), the equation is exploited in details by Ali Assy in his thesis [101]. The probe dissipation power when the probe is in-contact with the sample is:

$$P_{in} = \frac{kSL^2 m^3 \bar{\theta} [2mLch(\frac{mL}{2}) + \Omega sh(\frac{mL}{2})]}{mL [-4sh(\frac{mL}{2}) + 2mLch(\frac{mL}{2})] + \Omega [4(1 - ch(\frac{mL}{2})) + mLsh(\frac{mL}{2})]} \quad (3.40)$$

and when out-of-contact, is:

$$P_{out} = \frac{2kSL^2 m^3 \bar{\theta} ch(\frac{mL}{2})}{2mLch(\frac{mL}{2}) - 4sh(\frac{mL}{2})} \quad (3.41)$$

where $m^2 = \frac{hp}{kS}$ and $\Omega = \frac{G_s G_c}{G_p(G_s + G_c)}$.

MATLAB was used for the above calculations. For the determination of G_c and b_{air} , the data of $\frac{\Delta P}{P}$ for reference samples having known thermal conductivity are required. From then on, unknown thermal conductivities of experimental samples can be determined. The calibration samples in our experiments are shown in table 3.2.

3.3.2 Effective thermal conductivity for multi-layer samples

In SThM experiments, the thermal exchange radius b_{air} can be recognized approximately as the "probing depth" of the thermal probe for the measurement. That is to say, the obtained thermal conductivity value from the calculation represents the overall contribution of the sample material deep down to b_{air} maximum from the sample surface. This parameter is also tightly related to the sample thermal conductivity. As shown in figure 3.21, a less thermal

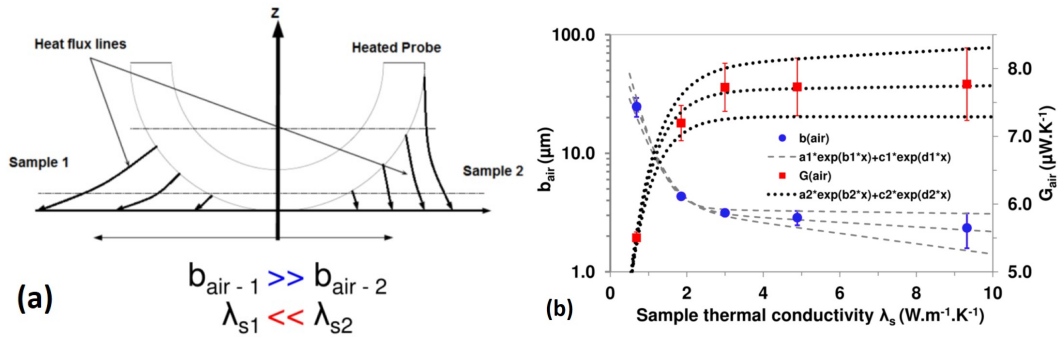


Figure 3.21: (a) Schematic illustration of the heat flux lines for two samples of different thermal conductivity λ_s . For less thermal conductive sample (λ_{s1}) the heat flux lines reach farther, thus giving a larger b_{air} . (b) Experimental data of b_{air} and G_{air} (thermal conductance through air, equals to G_c) as a function of λ_s (colored points), together with their corresponding fitting curves (in dots) [101].

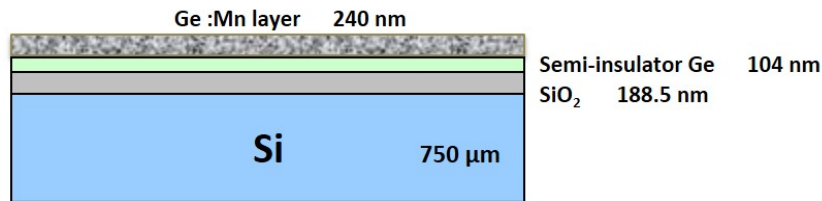


Figure 3.22: Schematic illustration of the multi-layer structure of a Ge:Mn thin film grown on the Germanium-on-Insulator substrate, with the thickness of each layer indicated in the graph.

conductive sample results in a larger b_{air} , and using a Wollaston probe the thermal exchange radius b_{air} can go up to $\sim 10 \mu\text{m}$ depending on the sample thermal conductivity. Figure 3.21 (b) also shows that the probe-sample contact conductance G_c depends also on the sample thermal conductivity, varying between $5 - 8 \mu\text{W}\cdot\text{K}^{-1}$. And both b_{air} and G_c show important variation for samples with low thermal conductivity ($k < 3 \text{ Wm}^{-1}\text{K}^{-1}$).

As to our Ge:Mn/GOI samples, due to the special GOI substrate the samples are all in a multi-layer structure shown in figure 3.22 (as presented in chapter 2). It can be noticed from the graph that the overall thickness of the multi-layers are only 500 to 600 nm. It then becomes possible that the "probing depth" being superior compared to the total thickness of all layers on Si substrate. In this case, the characterized thermal conductivity for Ge:Mn samples can only be recognized as an effective thermal conductivity, to which all probed materials (Ge:Mn, Ge, SiO₂ and Si) contribute. Hence, further development of a multi-layer model would be required for the extraction of the absolute thermal conductivity of Ge:Mn thin films.

3.4 Conclusion

To experimentally study the thermal properties of the epitaxial Ge:Mn thin films, we have chosen to use principally the 3-omega method. We have developed highly sensitive differential 3-omega experimental setups for the measurement of thermal conductivity of the Ge:Mn thin films with a thickness of $\sim 200\text{nm}$, at RT. 3-omega setups using the differential method and the Wheatstone bridge have both been developed and tested. The differential configuration has been chosen for all measurements of thin film samples in this work. Platinum transducers were used in the work in a four-contact geometry. The absolute error of the thin film thermal conductivity obtained using this experimental technique is about 14 %. The Thermal conductivity measurements using the scanning thermal microscopy have also been considered. The intention of using two experimental techniques is to ensure a better characterization of the thermal conductivity of the Ge:Mn materials.

Pour étudier expérimentalement les propriétés thermiques des films minces de Ge:Mn épitaxiés, nous avons choisi d'utiliser principalement la méthode 3-oméga. Nous avons ainsi développé deux montages expérimentaux hautement sensibles, basés sur la méthode 3-oméga, en utilisant une méthode différentielle ou un pont de Wheatstone. Ces configurations 3-oméga, ont toutes les deux été développées et testées. La configuration différentielle, plus facile à mettre en œuvre, a été choisie pour toutes les mesures d'échantillons de films minces à température ambiante. L'erreur absolue de la conductivité thermique d'un film mince obtenue en utilisant cette technique expérimentale a été estimée à environ 14%. Le SThM a également été utilisé pour les mesures de conductivité thermique pour comparaison

4 Experimental results on Ge:Mn thin films

Résumé

Afin de comprendre l'influence de nano-structures sur les mécanismes de la diffusion des phonons, les propriétés de transport thermique de plusieurs couches minces de Ge:Mn présentant des distributions d'inclusions différentes ont été étudiées. Grâce à leur caractéristiques structurales uniques présentées dans le chapitre 2, les films minces de Ge:Mn avec les nano-inclusions sont un système très intéressant pour étudier la diffusion des phonons et son influence sur le transport thermique. En effet, le diamètre et la distribution des nano-inclusions dans les films minces de Ge:Mn sont modifiables en faisant varier la température de recuit et la concentration de Mn pendant la croissance. Cela offre la possibilité d'étudier la façon avec laquelle les géométries des inclusions affectent le transport des phonons à l'intérieur des films minces de Ge:Mn.

Dans ce chapitre, nous allons présenter tous les résultats expérimentaux de mesure de conductivité thermique des films minces de Ge:Mn, en utilisant à la fois la méthode 3-oméga et la microscopie thermique à sonde locale comme décrit dans le chapitre 3. Les mesures 3-oméga sur un échantillon de Ge:Mn fabriqué sur un substrat Ge dopé de type-n, ont été réalisées afin de tester la faisabilité de l'expérience. Ce test s'avérant concluant, la conductivité thermique des couches minces de Ge:Mn ont été étudiées en fonction de la concentration de Mn et de la température de recuit. La dépendance en température de la conductivité thermique de différents échantillons de Ge:Mn (Ge:Mn/GOI et Ge:Mn-sur-Ge) a été étudiée par des mesures 3-oméga autour de la température ambiante.

In order to understand the influence of nano-structures on the phonon scattering mechanisms, the Ge:Mn nano-inclusion system was intensely studied in this work. Having unique growth processes and structural features as presented in chapter 2, the nano-inclusion embedded Ge:Mn thin film is one of the most interesting systems for the study of phonon scattering and thermal transport. Indeed, the diameter and distribution of nano-inclusions in Ge:Mn thin films are tunable by varying the annealing temperature and Mn concentration, which offers the possibility to study how exactly the inclusion geometries affect the phonon transport

inside the Ge:Mn thin films. It has then driven us to perform experimental measurements and numerical studies of this material.

In this chapter, we will present all experimental results of thermal conductivity measurements of Ge:Mn thin films, using both the 3-omega method and the scanning thermal microscopy as described in chapter 3. The 3-omega measurements on a Ge:Mn sample grown on a n-type doped Ge substrate have been carried out as tests. The variations of Ge:Mn thermal conductivity with Mn concentration and with annealing temperature have been studied. The temperature-dependency of thermal conductivity of different Ge:Mn samples (Ge:Mn/GOI and Ge:Mn-on-Ge substrat) have been studied through 3-omega measurements around RT.

4.1 Preparation for 3ω measurements

Once the Ge:Mn thin films are grown by MBE, several steps of sample preparation should be carried out to enable the thermal conductivity measurements using the 3ω method. The preparation includes the deposition of the insulating layer of Al_2O_3 by ALD, the lithography and the deposition of the Pt transducers, the wire-bonding of the sample, the mounting of the sample holder into the cryostat and etc. Measurement tests have been done on a Ge:Mn sample grown on a n-type Ge substrate, where different widths of transducer lines were tested and compared. The results helped us to decide the best transducer width for the measurements afterward.

4.1.1 Sample preparation and measurement setups

After the MBE growth, the Ge:Mn samples should be prepared for the 3ω measurements. As the Ge:Mn thin films are electrically conductive, an insulating layer should be deposited before the transducer metal line. In our work we have chosen to put a 50 nm thick Al_2O_3 layer deposited by ALD.

The Al_2O_3 was deposited by ALD in continuous mode, at a chamber temperature of 250 °C. The high chamber temperature can thermally help the construction of the layers during the deposition. The deposition rate is ~ 0.1 nm/cycle, so that with 500 cycles the thickness of Al_2O_3 obtained is ~ 50 nm. The ALD equipment is Savannah by Cambridge NanoTech Inc.(USA). After the ALD deposition a smooth and clean surface finish is obtained for the deposition of the transducer lines.

A standard UV-lithography was used to define the four-contact geometry of the transducer line, with the help of a mask shown in figure 4.1. The width ($2b$) of the transducer is designed to be 30 μm , the length 2 mm, and the size of the square contact 200 μm . After lift-off, the samples are cleaned using a plasma cleaner in order to remove resist residues. The cleaning process is with O_2 and Ar gases in 5:2 composition, applying a radio-frequency power of 200 W during 100s. The deposition of platinum transducer is done by a home-made Plasma-enhanced

4.1. Preparation for 3ω measurements

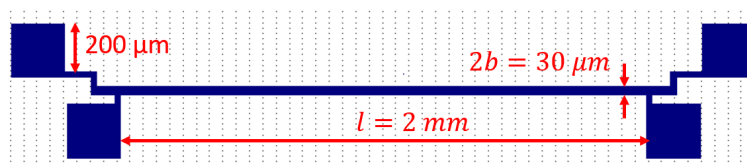


Figure 4.1: The designed mask of transducer line in four-contact geometry, with the width ($2b$) of the transducer $30 \mu\text{m}$, the length 2 mm , and the size of the square contact $200 \mu\text{m}$.

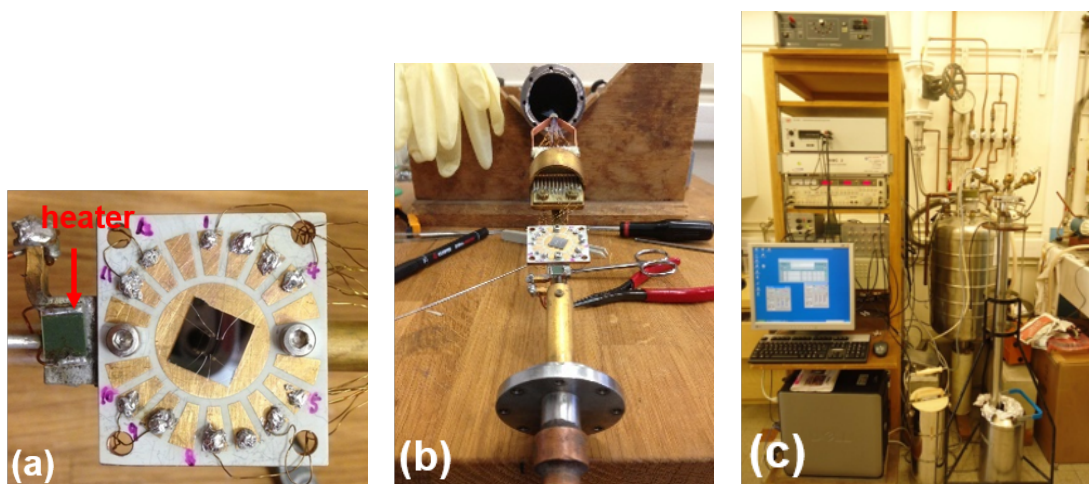


Figure 4.2: Experimental setups for differential 3ω technique: (a) sample holder with the sample stuck at the center and micro-bonded to the metallic pads around for connection; the temperature of the sample holder is controlled thanks to a heater and a standard commercial platinum thermometer (behind the heater in the image); (b) sample holder connected and ready to be mounted into a cryostat; (c) a view of the whole setups with a connected sample inside the cryostat.

Magnetron Sputtering Deposition system. The thickness of Pt deposition is in most cases 100 nm (a few tests with 150 nm) with a 5 nm adhesion layer of tungsten-titanium (WTi). The deposition rate is $6\sim 8 \text{ \AA/s}$, with the chamber at RT. During the deposition the sample holder was heated up to $70 \text{ }^\circ\text{C}$.

To guarantee the identical quality of the Al_2O_3 and Pt depositions for Ge:Mn sample and its reference substrate, as well as for a better accuracy of the differential 3ω technique, we have always proceeded the preparation steps of sample pairs (Ge:Mn samples and their reference GOI substrates) together.

Once the transducer lines are deposited, the sample is ready for the 3ω measurements. The differential-bridge 3ω setup was used for all the measurements on Ge:Mn samples. As shown in figure 4.2, the sample is stuck with a resist at the center of the sample holder, where metallic pads are around and connected with cables. The temperature of the sample holder is con-

trolled thanks to a heater and a standard commercial platinum thermometer stuck at the back side of the sample holder, which permits a temperature range of 30K-350K. The temperature regulator TRMC-2, an electronic system developed at Institut Néel and commercialized by CNRS (Centre National de la Recherche Scientifique, FRANCE) later on, has been used as the temperature controller system.

The contacts of the transducer line on the sample can be bonded with the metallic pads on the sample holder, either via micro-bonding or through manual manipulation using silver paint and thin aluminum wires. The micro-bonding system is a wedge-wedge manual wire bonder from West-Bond, Inc. The application of ultrasonic power and force is required to form the bonds, using aluminum wires with $25\mu\text{m}$ in diameter. In the case of Ge:Mn samples, where only a 50 nm thick Al_2O_3 insulating layer is present between the conductive Ge:Mn thin film and the transducer line, attention was paid to make sure that the bonding does not break through the oxide layer. For this reason, very low ultrasonic power (270 W during 30 ms) and low force (with 30g weight) have been applied for the bonding on contacts of transducer. However, later on, preference was given to manual wire-bonding using silver paint, to avoid completely the risk of breaking-through with the wedge touching. In this manner, very small drops of silver paint have been applied manually on to the contacts of transducer, then the same aluminum wires have been put carefully on to the drops. Once the drops are dried, the other sides of the Al wires can be bonded to the bigger pads with silver paint as well.

Afterward, the sample holder is connected, mounted inside a cryostat and pumped to a vacuum level of 10^{-5} mbar. The cryostat permits also the use of a commercial germanium thermometer, which is efficient at temperatures down to 4K, so that measurements within the temperature range of 4K-350 K are possible. However in our experiments, only the RT range of 260-320K has been studied.

4.1.2 Tests on a Ge:Mn sample grown on a n-type Ge substrate

To determine the width of the transducer lines for the differential 3-omega measurements, transducer patterns with different widths were designed, deposited and tested on a Ge:Mn sample. The width of the transducer was chosen to be $20\mu\text{m}$, $30\mu\text{m}$ or $50\mu\text{m}$ [58, 87, 59, 102]. The objective was to decide the best transducer width which permits the most stable and reliable 3ω measurements. However, it has been noticed that slightly rough borders may present after the lift-off process for transducers $20\mu\text{m}$ wide. Measurements with Pt transducer width of $30\mu\text{m}$ and $50\mu\text{m}$ were then carried out on a Ge:Mn sample grown on a n-type Ge substrate at RT.

The Ge:Mn sample used for tests is a Ge:Mn thin film of 6% Mn and 240 nm thick, grown on a n-type Ge substrate, noted as "S8". Measurements via a $50\mu\text{m}$ wide, 150 nm thick Pt transducer have been done. The transducer's resistance $R_{tr} \sim 36\Omega$ at 300K, with a calibrated $\alpha = 0.00317\text{ K}^{-1}$. Firstly, it is important for us to test and acquire the exact value of the thermal conductivity of the Ge substrate. From the variation of $\Delta T/P$ as a function of frequency ($\ln \omega$),

4.1. Preparation for 3ω measurements

the thermal conductivity of the substrate (k_0) can be extracted following equation 3.15:

$$k_0 = -\frac{1}{2\pi l} \left[\frac{d\left(\frac{\Delta T_{real}}{P}\right)}{d \ln \omega} \right]^{-1}$$

The thermal conductivity value of Ge substrate was extracted from the experimental curves of $\Delta T/P$ presented in figure 4.3, and results are presented in table 4.1. It can be noticed from the results that, with a $50 \mu\text{m}$ wide transducer, the extracted thermal conductivities of Ge substrate spread over a very large range, between 47 and $74 \text{ Wm}^{-1}\text{K}^{-1}$ at RT. A cross point of all curves appears at frequency $\sim 150 \text{ Hz}$, for which no fair explanation has been found.

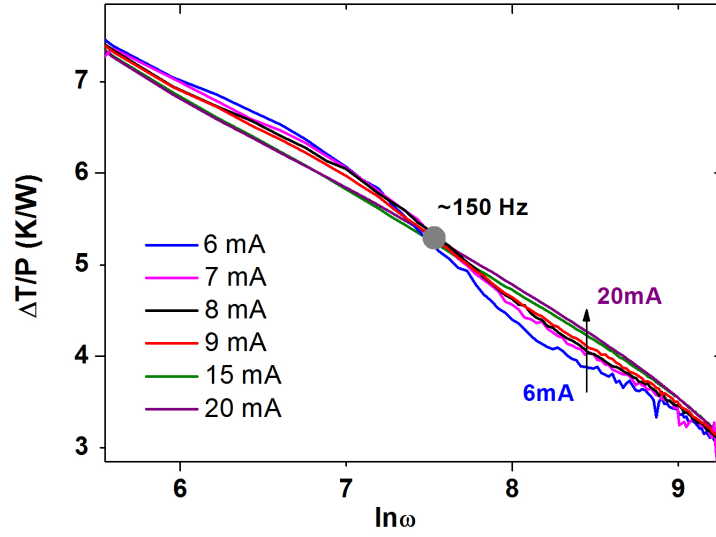


Figure 4.3: Experimental curves of normalized temperature oscillation ($\Delta T/P$) as a function of frequency ($\ln \omega$) recorded from a $50 \mu\text{m}$ wide transducer applying different AC currents, from a sample Ge:Mn on a n-type Ge substrate. The black arrow indicates the increase of current, and curves from different currents are distinguished by color.

T=300K, $\alpha=0.00317 \text{ K}^{-1}$, $R_{tr}=36 \Omega$, $2b=50 \mu\text{m}$						
Current (mA)	6	7	8	9	15	20
Linear heat dissipation power P_l (W/m)	0.648	0.882	1.152	1.458	4.05	7.2
k_{Ge} ($\text{Wm}^{-1}\text{K}^{-1}$)	47	51	54	59	72	74

Table 4.1: Experimental results of thermal conductivity of Ge substrate measured via a $50 \mu\text{m}$ wide transducer at different AC current, for a sample Ge:Mn on n-type Ge substrate. The values of k_{Ge} are extracted from experimental curves of $\frac{\Delta T}{P}$ presented in figure 4.3.

The same experiments have then been done on a $30 \mu\text{m}$ large transducer deposited at the

Chapter 4. Experimental results on Ge:Mn thin films

T=300K, $\alpha=0.0032\text{ K}^{-1}$, $R_{tr}=60\ \Omega$, $2b=30\ \mu\text{m}$					
Current (mA)	5	6	7	10	12
Linear heat dissipation power P_l (W/m)	0.75	1.08	1.47	3	4.32
k/k_{ref}	0.97	1.00	1.02	1.06	1.06

Table 4.2: Experimental results of thermal conductivity of Ge substrate measured at different AC currents normalized regarding the value obtained with $P_l = 1\text{ W/m}$ (k_{ref}). The results were obtained from a Ge:Mn sample on n-type Ge substrate via a $30\ \mu\text{m}$ wide transducer.

Temperature	260	280	290	300	310	333
k_{Ge} ($\text{Wm}^{-1}\text{K}^{-1}$)	67.6	62.2	57.8	57.0	56.4	51.6

Table 4.3: Experimental results of thermal conductivity of Ge substrate measured at different temperatures with a dissipation power of 1 W/m . The results were obtained from a Ge:Mn sample on n-type Ge substrate via a $30\ \mu\text{m}$ wide transducer.

same time (150 nm thick) on to the same sample. The results are shown in table 4.2, which presents a much more stable variation of thermal conductivity of Ge substrate compared to results from a $50\ \mu\text{m}$ large transducer at RT. In these experiments, with heating current varying from 5 mA to 12 mA , the corresponding linear power dissipation varies from $\sim 1\text{ W/m}$ to 4 W/m . When the dissipation power is too high, the transducer will be heated too much, thus the local temperature of the sample is no longer the regulated one. This overheating can bring significant errors in the measurement results. In this work, it has then been preferably decided to dissipate a linear heat dissipation power of $P_l \sim 1\text{ W/K}$ [102] using a Pt transducer with a width of $30\ \mu\text{m}$, for all measurements afterward.

The temperature dependent thermal conductivities of the Ge substrate have then been measured within the range of $260\text{-}330\text{ K}$, with a linear heat dissipation power of $\sim 1\text{ W/m}$ and a $30\ \mu\text{m}$ wide transducer. The results are presented in figure 4.3, which show very good coherence with the experimental curves presented previously in figure 1.9 (chapter 1).

The extraction of thermal conductivity of Ge:Mn thin film has been done, with the help of extra data measurement from a bare Ge n-type substrate sample. The experimental curves of $\Delta T/P$ as a function of $\ln\omega$ from both samples obtained at 300K , are presented in figure 4.4. A shift of 0.5 K/W can be identified from the curves and the calculated thermal conductivity of this Ge:Mn thin film gives a value of $10.4\text{ Wm}^{-1}\text{K}^{-1}$ at RT. This thermal conductivity value brings a dramatic reduction by a factor of 6 from that of a standard Ge material. This was the first demonstration of a significant reduction of thermal conductivity in nano-inclusion embedded Ge:Mn thin film. The result encouraged us to carry out more systematic measurements on different Ge:Mn samples, with different %Mn or $T_{annealing}$. These systematic studies permitted us to investigate the influence of nano-inclusion geometry on the thermal transport properties of Ge:Mn material.

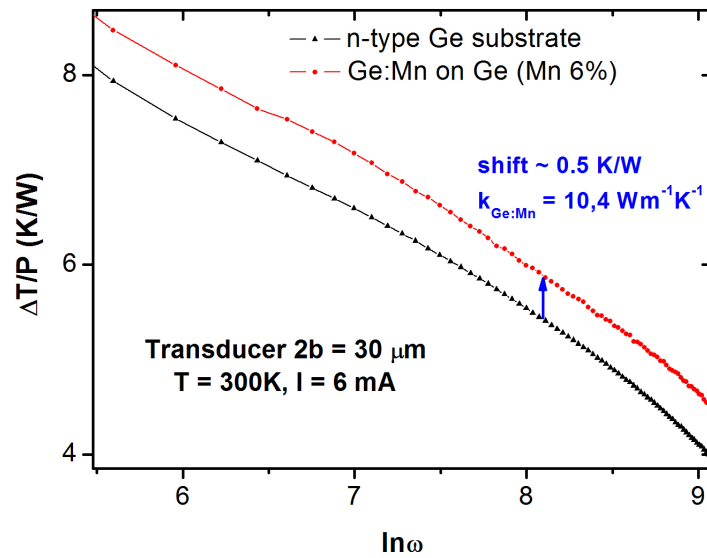


Figure 4.4: Experimental curves of $\Delta T/P$ as a function of $\ln \omega$ obtained from both the 6% Ge:Mn sample and its Ge substrate (n-type) at 300K. The transducer line is $30 \mu\text{m}$ wide and applied AC current 12 mA.

4.2 3ω measurements on a series of Ge:Mn/GOI samples

After the promising measurement results on the Ge:Mn sample grown on a n-type Ge substrate, interest is now focused on Ge:Mn samples grown on GOI substrates with different Mn concentrations or annealed at different temperatures.

The Germanium-on-Insulator substrates (structure shown in chapter 2, figure 2.4 (a)) used for the growth of Ge:Mn have been specifically developed and produced by CEA-LETI. The wafers were accessible to CEA-INAC in the framework of the European research project "MERGING". The project focuses on the development of thermoelectric modules using different TE materials, especially Si, Ge and related SC materials. The Ge top layer in the GOI substrate is semi-insulating. Rare for Ge materials, this semi-insulating property permits measurements of the electrical conductivity and the Seebeck coefficient of the Ge:Mn samples. Most importantly, the presence of the oxide layer of SiO_2 in GOI enables the elaboration of suspended Ge membranes for further development of different types of suspended TE modules. Using a new approach that has been implemented in Institut Néel, the SiO_2 layer can be successfully etched by HF vapor while the Ge layer is protected from oxidation thanks to a protecting layer of polymer. The suspended Ge membrane can have a slice geometry as shown in figure 4.5 with different aspect ratios.

Figure 4.6 presents an illustration of a series of $\Delta T/P$ curves as a function of frequency ($\ln \omega$),

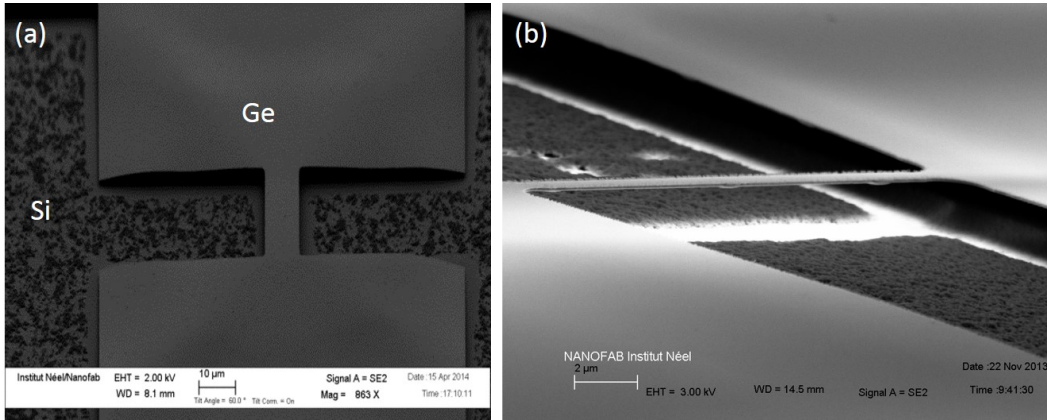


Figure 4.5: Scanning electron microscopy images of Ge membranes suspended between two contact pads from a GOI structure: (a) front view, the Ge membrane has $20\mu\text{m}$ in length and $10\mu\text{m}$ in width; (b) side view.

corresponding to each addition of layers from the Si substrate in a Ge:Mn/GOI sample. For a bare Si substrate, the $\Delta T/P$ curve locates at the lowest position in the graph. With the addition of the SiO_2 layer (188.5 nm), the $\Delta T/P$ curve gains an extra signal and shifts upwards. The addition of the Ge layer (104 nm) brings only a negligible shift compared to the one brought by SiO_2 , due to the high thermal conductivity of Ge. The position of the $\Delta T/P$ curve for a GOI substrate is then colored in blue in the graph. Then, with a Ge:Mn layer which potentially has a low thermal conductivity, another shift is introduced from which the thermal conductivity of the Ge:Mn layer can be extracted. It is clear that, from the $V_{3\omega}$ signals of GOI, it is impossible to extract the thermal conductivities of each component of the multi-layer. Only the thermal conductivity of the Si substrate can be calculated using the slope value of the curve, as well as the Ge:Mn thermal conductivity from the last shift of the $\Delta T/P$ curve.

Intensive measurements were performed on a series of Ge:Mn/GOI samples grown with Mn concentrations of: 6%, 8%, 10%, 12% and 14%. All Ge:Mn thin films of these Ge:Mn/GOI samples are 240 nm thick. The variations of the Ge:Mn thermal conductivity with Mn concentration and with annealing temperature were studied. All measurements on these samples have been done using transducer lines $30\mu\text{m}$ in width, and with a power dissipation of 1 to 4 W/m.

Firstly, the thermal conductivity of the Si substrate of a GOI was studied at different temperatures. The thermal conductivities of different Ge:Mn/GOI samples were measured at RT. The influence of the $T_{annealing}$, and of the Mn% on the Ge:Mn thermal conductivity have been studied. Finally, the variation of the thermal conductivities with temperature for different Ge:Mn/GOI samples were studied within RT range.

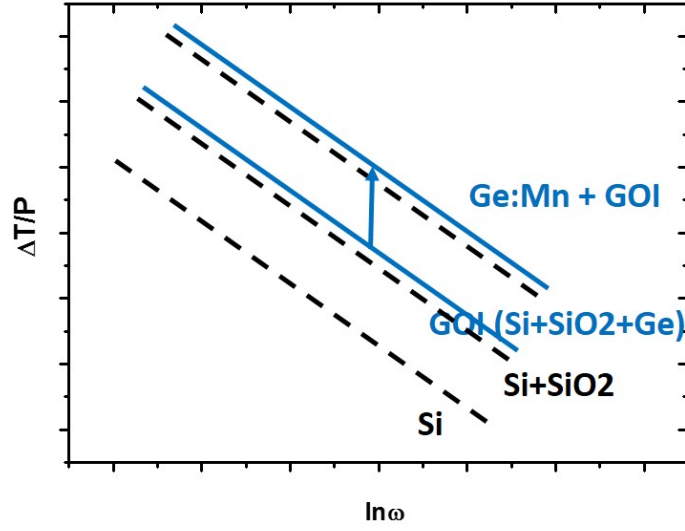


Figure 4.6: Illustration of a series of $\Delta T/P$ curves as a function of frequency ($\ln \omega$), corresponding to the addition of each layers on the Si substrate in a Ge:Mn/GOI sample.

4.2.1 Measurements of Si thermal conductivity from GOI substrate at different temperatures

A reference sample of GOI substrate was firstly prepared and measured. Experimental data of $V_{3\omega}$ as a function of frequency ($\ln \omega$) was recorded, at different temperatures within the RT range. The frequency range is 50-1000 Hz, which corresponds to a thermal penetration depth of 45 to 203 μm into the silicon substrate (following equation 3.7). The curves of $\Delta T/P$ as a function of $\ln \omega$ were then obtained, as shown in figure 4.7. From the slope of each curve, the thermal conductivity of the substrate (i.e. Si) can be calculated. The values of Si thermal conductivity obtained at different temperatures are presented in table 4.4.

GOI substrate						
T (K)	280	300	310	320	340	350
k_{Si} ($\text{Wm}^{-1}\text{K}^{-1}$)	134	130	126	106	104	98

Table 4.4: Experimental results of the Si substrate thermal conductivity at different temperatures from a bare GOI substrate sample, extracted from figure 4.7.

From table 4.4, it is evident that the thermal conductivity of Si shows a decrease as temperature increases within RT range. The value of $130 \text{ Wm}^{-1}\text{K}^{-1}$ at 300K for Si thermal conductivity also shows a good coherence with the literature, compared to the experimental values obtained from high purity intrinsic silicon single crystals [103]. Hence, our 3-omega measurement setups are once more validated.

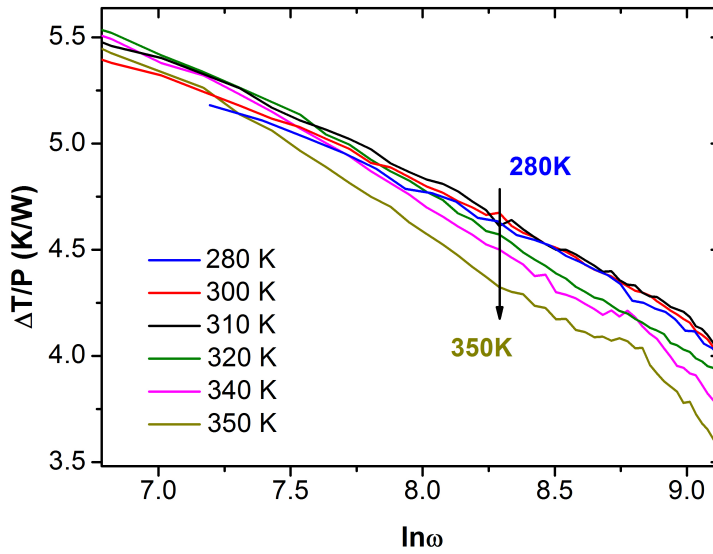


Figure 4.7: Experimental curves of $\Delta T/P$ as a function of frequency ($\ln \omega$) from a GOI substrate sample, measured at different temperatures. The black arrow indicates the increase of temperature. Curves for different temperatures are distinguished by color.

4.2.2 Extraction of Ge:Mn thermal conductivity

Figure 4.8 presents the experimental curves of $\Delta T/P$ as a function of frequency ($\ln \omega$) obtained from a Ge:Mn/GOI sample with 10% Mn (S7) and a bare GOI substrate, at 300K. From the shift between the two curves, the thermal conductance of the Ge:Mn layer can be extracted. Then knowing the thickness of the thin film, equation 3.17 and equation 3.18 permit the extraction of the thermal conductivity of the film. For the case involved in figure 4.8, a value of $3.3 \text{ Wm}^{-1}\text{K}^{-1}$ for the thermal conductivity of Ge:Mn at RT can be extracted.

Measurement results on the whole series of Ge:Mn/GOI samples at RT are presented in table 4.5, concerning seven different Ge:Mn thin films labeled as S1-S7, grown with different Mn% or annealed at different temperatures.

Sample Ge:Mn/GOI	S1	S2	S6	S3	S7	S4	S5
%Mn	6	8	8	10	10	12	14
$T_{annealing}$ ($^{\circ}\text{C}$)	709	672	743	709	757	703	716
$k_{3\omega}$ ($\text{Wm}^{-1}\text{K}^{-1}$)	15.0	8.2	7.4	3.5	3.3	7.6	13.0

Table 4.5: Experimental results of thermal conductivity of different Ge:Mn thin films on GOI (with different Mn% or annealed at different temperatures), obtained from 3ω measurements at RT. The error of each experimental value is 14.4%.

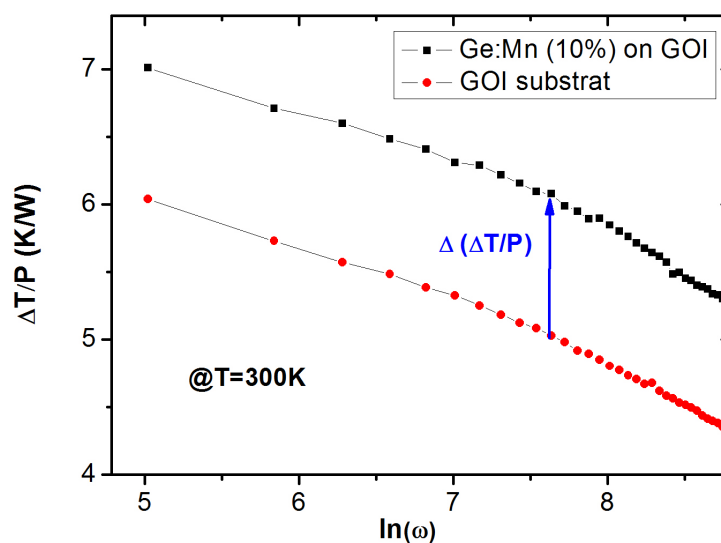


Figure 4.8: Experimental curves of $\Delta T/P$ as a function of frequency from a Ge:Mn/GOI sample with 10% Mn (S7) and a bare GOI substrate, at 300K.

4.2.3 Influence of $T_{annealing}$ on Ge:Mn thermal conductivity

Comparing the measurement results of Ge:Mn sample S2 and S6 (table 4.5) both grown with 8% Mn but annealed at different temperatures, their thermal conductivity values are very close. It can then be concluded that, within the range of 672 to 743 °C, the annealing temperature has no significant effect on the thermal conductivity of Ge:Mn thin films. However, it should be reminded that as shown in figure 2.5 and figure 2.6 (chapter 2), the annealing temperature does have significant effects on the diameter distribution and the geometries of nano-inclusions in these two samples. Hence, it can be concluded that the geometries of the nano-inclusions do not have a prominent effect on the Ge:Mn thermal conductivity.

4.2.4 Influence of %Mn on Ge:Mn thermal conductivity

A plot of the thermal conductivity values in table 4.5 as a function of Mn concentration is presented in figure 4.9. It can be observed from the plot that the thermal conductivities of Ge:Mn thin films show significantly reduced values, by a factor of 4 to 20 depending on the Mn concentration compared to that of a standard bulk Ge at RT ($60 \text{ Wm}^{-1}\text{K}^{-1}$). A "V" shape is remarkable from 6% Mn to 14% Mn with a minimum value of thermal conductivity $3.3 \text{ Wm}^{-1}\text{K}^{-1}$ found for Ge:Mn thin film grown with 10% Mn. It should also be noticed that as the Mn concentration varies from 6% to 10% the thermal conductivity of Ge:Mn is reduced by a factor of 5.

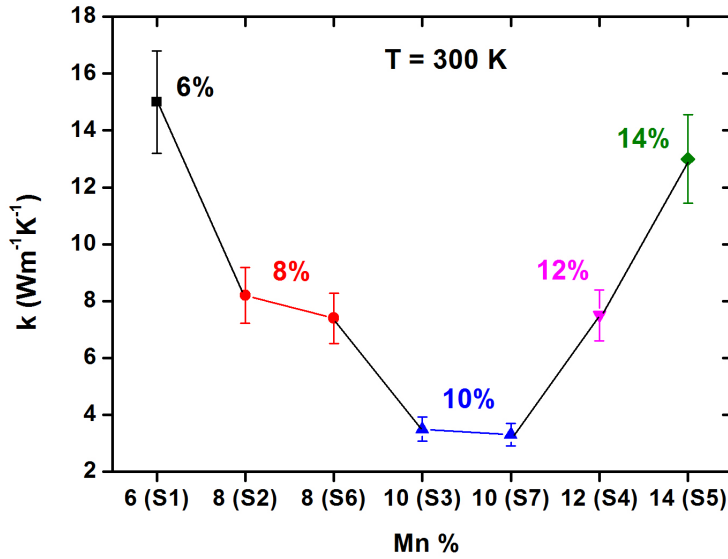


Figure 4.9: Experimental curve showing the RT thermal conductivity results of Ge:Mn thin films as a function of Mn concentration (from data in table 4.5). The error bar of each data is 14.4%. The "V" shape of the curve gives the minimum value at Mn concentration of 10%.

This strong reduction of thermal conductivity due to the presence of nano-structures in a 3D SC matrix has so far not been revealed in any other materials, especially not in Si/Ge based SCs. These results on Ge:Mn samples make the most important discussion in this thesis. The presence of nano-inclusions in the Ge matrix indeed has significant effects on the thermal transport properties of the matrix, i.e. the phonon transport processes. It can be surmised that the nano-inclusions create more scattering centers for phonons thus reducing dramatically the phonon MFP [3]. Furthermore, the thermal conductivities of $\text{Si}_{1-x}\text{Ge}_x$ alloys have been found to be $\sim 6\text{-}12 \text{ Wm}^{-1}\text{K}^{-1}$ (for $0.2 < x < 0.85$) at RT, according to the literature ([104, 105]). Hence, it has been demonstrated that all measured Ge:Mn thin films have the thermal conductivities in the same range as $\text{Si}_{1-x}\text{Ge}_x$ alloys at RT. Even more, the 10%Mn Ge:Mn with a thermal conductivity value of $\sim 3 \text{ Wm}^{-1}\text{K}^{-1}$ at RT has beaten the "alloy limit" set by $\text{Si}_{1-x}\text{Ge}_x$ by a factor of two. This is quite remarkable because the Ge:Mn thin film has a perfect single crystalline matrix. Despite the fact that the impurity phonon scatterings do exist in Ge:Mn due to the presence of natural Ge isotopes (see chapter 2), they are still much less important than in the case of an alloy.

Regarding these experimental results, further discussions are required to exclude other possible factors which could participate to the strong reduction of thermal conductivity in Ge:Mn. The discussion concerns mainly three aspects:

- (1) the contribution of the thickness error of SiO_2 layer (thermal conductivity $1.2 \text{ Wm}^{-1}\text{K}^{-1}$) in

4.2. 3ω measurements on a series of Ge:Mn/GOI samples

GOI to the $\Delta T/P$ shift for Ge:Mn/GOI samples;

(2) the contribution of the electronic thermal conductivity in Ge:Mn;

(3) the contribution of the film thickness.

Let us firstly discuss point (1). It is indeed imaginable that the SiO_2 layer (thickness 188.5 nm) in one GOI wafer is not perfectly uniform everywhere. As SiO_2 has a very small thermal conductivity $\sim 1.2 \text{ Wm}^{-1}\text{K}^{-1}$ at RT, a small difference in the thickness of SiO_2 between different samples may contribute to the shift in the temperature oscillation in differential 3-omega measurements. Considering the error bar of the thickness of SiO_2 in GOI to be about 1 nm, by calculation the corresponding $\Delta T/P$ shift is 0.031 K/W. On the other hand, the $\Delta T/P$ shifts that yielded the thermal conductivity results for different Ge:Mn thin films are in the range of 0.3 to 1 K/W. Hence, the existence of the 1 nm error in SiO_2 layer brings a maximum of 10% uncertainty for the result corresponding to the Ge:Mn thin film grown with 6% and 14% Mn, and only 3% for Ge:Mn thin film containing 10% Mn with a measured thermal conductivity of $3 \text{ Wm}^{-1}\text{K}^{-1}$. So the presence of the thickness error of the SiO_2 layer should not contribute significantly to the absolute error of the estimation of the Ge:Mn thermal conductivity.

Concerning the second point, as the Ge:Mn thin film has a p-type Ge semi-conductor matrix, the electronic thermal conductivity (k_e) of the material should indeed be considered. The electrical conductivities (σ) of Ge:Mn thin films at RT have been measured by Mustapha Boukhari at INAC/CEA, and values around $100 \Omega^{-1}\text{cm}^{-1}$ have been revealed for Ge:Mn films containing 8% and 10% Mn. Then applying Wiedemann-Franz law (equation 1.49) for a temperature of 300K, the electronic thermal conductivity of Ge:Mn was calculated to be $\sim 0.073 \text{ Wm}^{-1}\text{K}^{-1}$. As compared to the overall thermal conductivity values of $3\text{-}15 \text{ Wm}^{-1}\text{K}^{-1}$ measured for Ge:Mn thin films, the contribution of k_e is then neglected.

Regarding the point (3), it is indeed very important to know the value of thermal conductivity of a 240 nm thick pure Ge film and to compare the results of Ge:Mn thin films with that of a Ge film. With the differential 3-omega technique, it is conceivable to carry out 3ω experiments on a 240 nm thick Ge layer grown on a GOI substrate as shown in figure 4.10. However, according to the calculation using equation 3.17 and 3.18, considering $R_c = 10^{-9} \text{ Km}^2\text{W}^{-1}$ for the Ge-Ge interface a shift of $\Delta T/P \approx 0.084 \text{ K/W}$ was found for a Ge layer of 240 nm. This shift is equivalent to the contribution of a SiO_2 layer of $\sim 4.8 \text{ nm}$, which is very difficult to be distinguished in the practical measurements. As a result, it was decided not to carry out thermal conductivity measurements on a 240 nm thick Ge film.

Hence, the question was asked, is the phonon MFP in a 240 nm thick Ge film the same compared to that in the Ge bulk at RT? According to a recent experimental work on suspended silicon membranes [4] (figure 4.11 (a)), the thermal conductivity of a 200 nm thick Si membrane has only a reduction of $\sim 40\%$ compared to the value for a bulk Si ($148 \text{ Wm}^{-1}\text{K}^{-1}$). As Si has a thermal conductivity almost three times that of Ge at RT, the phonon MFP in Ge should be smaller than that in Si. According to the simulation work of Singh et al. [106] the phonon MFP in Ge bulk is evaluated to be around 200 nm at RT (against $\sim 270 \text{ nm}$ in Si). Numerical

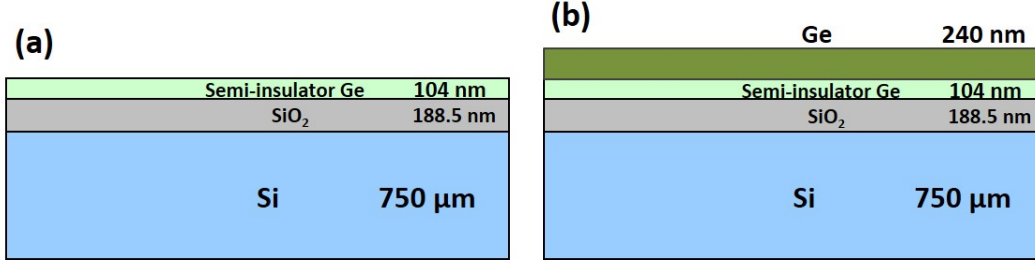


Figure 4.10: Schematic illustration of: (a) the Germanium-on-Insulator substrate used for the growth of the Ge:Mn thin films; (b) a Ge layer (240 nm) grown on the GOI substrate.

Ge:Mn sample	S2	S3	S4	S5
Mn%	8	10	12	14
$k_{3\omega}$ ($\text{Wm}^{-1}\text{K}^{-1}$)	8.2	3.3	7.6	13
$\Lambda_{3\omega}$ (nm)	27	11	25	43

Table 4.6: Calculation results of the phonon MFP ($\Lambda_{3\omega}$) in Ge:Mn thin films grown with different Mn concentrations using the kinetic relation based 3ω experimental results. The Ge phonon MFP at RT is taken to be 200 nm.

studies of Jean Valentin in his PhD thesis [107] also obtained a value of ~ 230 nm for Ge bulk material at RT, as shown in figure 4.11(b). According to the simulation curve in figure 4.11(b) the spectrum of the Ge phonon MFP centers around 230 nm at RT. Consequently, in our next discussions the value of 200 nm is taken as a reference value for the phonon MFP in Ge bulk.

Let us take a further look at the reduction of phonon MFP corresponding to the experimental thermal conductivity results. According to the classic kinetic theory discussed in chapter 1, at a certain temperature, the thermal conductivity of a material is in linear relation (equation 1.46) with the phonon MFP. Taking the experimental results of $k_{Ge:Mn}$ from 3ω measurements, their reduction factors from the value of Ge thermal conductivity k_{Ge} should correspond to the reduction of phonon MFP in Ge:Mn thin films as compared to Ge:

$$\frac{k_{Ge}}{k_{Ge:Mn}} = \frac{\Lambda_{Ge}}{\Lambda_{Ge:Mn}} \quad (4.1)$$

Taking the phonon MFP in Ge bulk $\Lambda_{Ge} = 200$ nm at RT, the values of phonon MFP in Ge:Mn can be calculated using equation 4.1 based on 3ω measurement results for Ge:Mn thin films grown with different Mn concentrations. The obtained Ge:Mn phonon MFP values, referred to as $\Lambda_{3\omega}$, are presented in table 4.6.

From table 4.6 it can be seen that, the phonon MFP in Ge:Mn thin films are strongly reduced by a factor of 4 to 20 compared to Ge bulk. The values of phonon MFP in Ge:Mn are within the range of 10-50 nm, way below the thickness of the Ge:Mn thin films (240 nm). A remarkable

4.2. 3ω measurements on a series of Ge:Mn/GOI samples

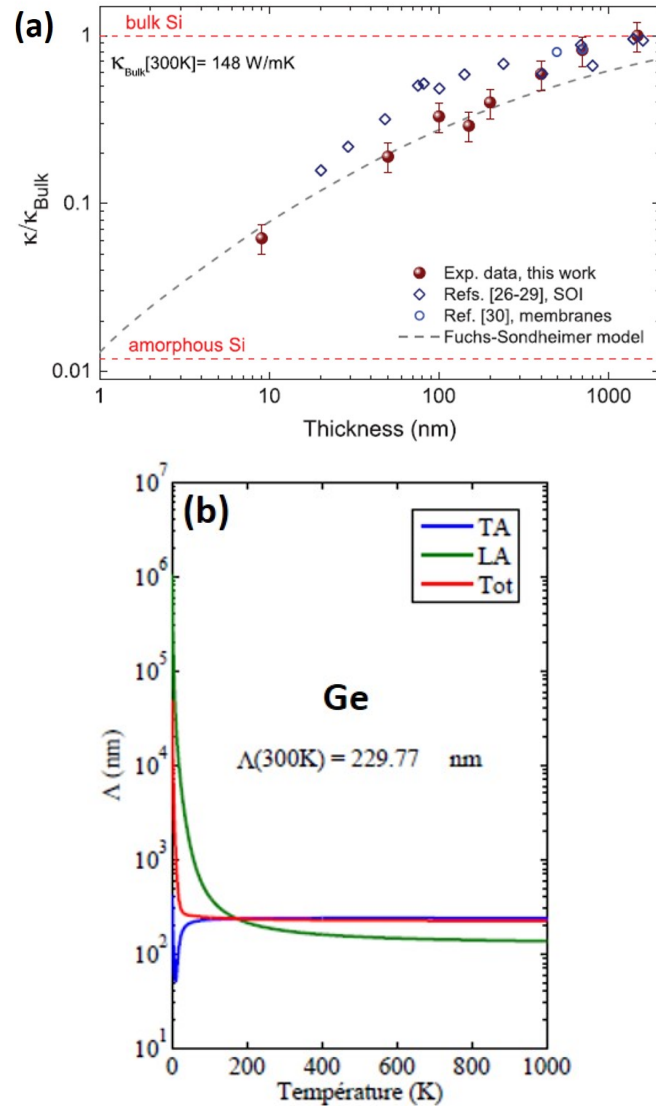


Figure 4.11: Thermal conductivities of the Si membranes, k/k_{bulk} , normalized to the bulk Si value as a function of the thickness are shown in solid red symbols, in comparison with previous works on SOI and membranes. The amorphous Si (a-Si) limit is also shown in dotted-dashed line [4]. (b) Simulation curves of the phonon MFP as a function of temperature for Ge [107]. The curve in color blue is for transverse acoustic phonons and color green for longitudinal acoustic phonons. The average Ge phonon MFP is the curve in red.

minimum value of 11 nm corresponds with the minimum value of Ge:Mn thermal conductivity of $3.3 \text{ Wm}^{-1}\text{K}^{-1}$. Hence it can be concluded that, even the thermal conductivity of a 240 nm thick Ge film could already have a certain reduction compared to that of Ge bulk (following the studies on Si), this reduction does not have a chance to contribute to the strong reduction of thermal conductivity by a factor of 4 to 20 in 240 nm thick Ge:Mn thin films.

As a consequence, it is believed that the significant reduction of thermal conductivity in Ge:Mn thin films results only from the presence of the nano-inclusions, which affect directly the phonon MFP in Ge.

4.2.5 Discussions

Reduction of thermal conductivity using nano-structuration in condensed matters has already been revealed experimentally in various systems. As to ErAs-embedded InGaAs thin films, the reduction of the thermal conductivity by two below the alloy limit has been demonstrated to be the contribution of both the nano-inclusions and the alloy matrix [43]. The nano-inclusions were found to be efficient to scatter mid-to-long-wavelength phonons, while alloy matrix contribute importantly to the scattering of short wavelength phonons. For the case of Si/Ge based nanodot superlattices (SLs), low cross-plane thermal conductivities ($\sim 2 \text{ Wm}^{-1}\text{K}^{-1}$) have also been found for SLs with short period length (2 nm) [21]. However, the effect of nanodots on the thermal transport was found to be comparable with that produced by planar wetting layers, which was used to relax the strain due to the lattice mismatch. Enhanced TE device performance has been revealed for PbSe nanodot embedded 3D PbTe matrix, with a ZT value of 1.6 against the 0.34 for the bulk alloy at RT [8]. The decrease of thermal conductivity by a factor of > 2 was found to be entirely due to the high density of quantum nanodots.

Nanowires are also one of the most efficient systems to decrease the thermal conductivity. Studies on rough Si nanowires with diameters of 50 nm revealed a 100-fold reduced thermal conductivity compared to Si bulk, attributed to small diameter, surface roughness and impurities [22]. Furthermore, amorphous Si (*a*-Si) and Ge (*a*-Ge) thin films have been demonstrated to have very low thermal conductivities. Experiments on *a*-Si thin films, having thicknesses of 0.2-1.5 μm , revealed thermal conductivity values $< 2 \text{ Wm}^{-1}\text{K}^{-1}$ for temperature range of 50-500K [59]. Low thermal conductivities ($< 1 \text{ Wm}^{-1}\text{K}^{-1}$) in temperature range of 30-300K have also been found for 50 μm thick *a*-Ge film [108]. For *a*-Ge films with thicknesses of 20-150 nm, thermal conductivity values $< 0.64 \text{ Wm}^{-1}\text{K}^{-1}$ at RT have also been revealed experimentally [109]. However, these amorphous materials can not be applied as thermoelectric materials due to their low electrical conductivities [110].

In comparison with all above systems, for Ge:Mn thin films, the dramatic reduction of the thermal conductivity by a factor up to 20 from a single-crystalline Ge matrix has been demonstrated to be only due to the Ge_3Mn_5 nano-inclusions. This remarkable reduction of thermal conductivity at RT makes the Ge:Mn thin films among the most interesting materials for thermal engineering, and the most promising 3D TE materials for RT applications. The dramatic reduction of phonon MFP in these Ge:Mn thin films also stimulates us to understand what are the scattering mechanisms behind, and how exactly the nano-inclusions affect the phonon transport. To try to answer these questions, an elaborated numerical model is required to theoretically explain the physics behind the experimental results.

4.2.6 Conclusion

The experimental measurements at RT on the series of Ge:Mn/GOI samples, having different %Mn or annealed at different temperatures, have shown dramatically reduced thermal conductivity values compared to that for Ge bulk, with a reduction of 4 to 20. A minimum thermal conductivity of $\sim 3 \text{ Wm}^{-1}\text{K}^{-1}$ has been found for Ge:Mn thin film grown with 10% Mn, beating the "alloy limit" set by $\text{Si}_{1-x}\text{Ge}_x$ at RT. The annealing temperature has no significant influence on the thermal properties of the Ge:Mn thin films, although it does have influences on the geometry of the nano-inclusions. The strong reductions of thermal conductivities in Ge:Mn thin films containing 6%-14% Mn show that the presence of nano-inclusions in the crystalline Ge matrix has indeed a significant influence on the phonon transport in the matrix. It can be predicted that the nano-inclusions create more scatterings for phonons in Ge, resulting in a strong reduction of the phonon MFP. From a general point of view, it also paves a way to a real control of the thermal conductivity of these SC Ge:Mn thin films.

4.3 Variation of Ge:Mn thermal conductivity with temperature

Further studies on the temperature-dependence of Ge:Mn thermal conductivity have been done on different Ge:Mn samples, within a temperature range of 260K-340K. It includes three Ge:Mn/GOI samples with 240 nm thick Ge:Mn layer (S2, S6, S7), and one special Ge:Mn/GOI sample (named REC07, 8% Mn) with a Ge:Mn film of only 80 nm thick.

The temperature-dependence curves of the thermal conductivities of different Ge:Mn/GOI thin films are plotted together in figure 4.12. It can be seen from the figure that, in general, the thermal conductivities of Ge:Mn samples decrease with temperature raise. The increase of the thermal conductivity with temperature for sample Ge:Mn grown with 10% Mn, stays an exception. However, the strong decrease of the thermal conductivity with temperature for sample "REC07" stays still difficult to understand.

From the temperature-dependence curves of thermal conductivity of Ge shown in figure 1.9, it can be estimated that for Ge the variation between the thermal conductivity values from 260K to 320K does not exceed 5%. It is then reasonable to expect the degree of variation for Ge:Mn materials, and the thermal conductivity curves are awaited to be more or less flat in this temperature range. To confirm these expectations more experiments are required to be performed at a larger temperature range. It is also extremely interesting to carry out measurements at much lower temperatures to see if the $k(T)$ curve for Ge:Mn has the same form as the one for Ge, which contains a peak at $\sim 10\text{K}$. These temperature studies would permit us to thoroughly understand the thermal transport properties of the Ge:Mn materials.

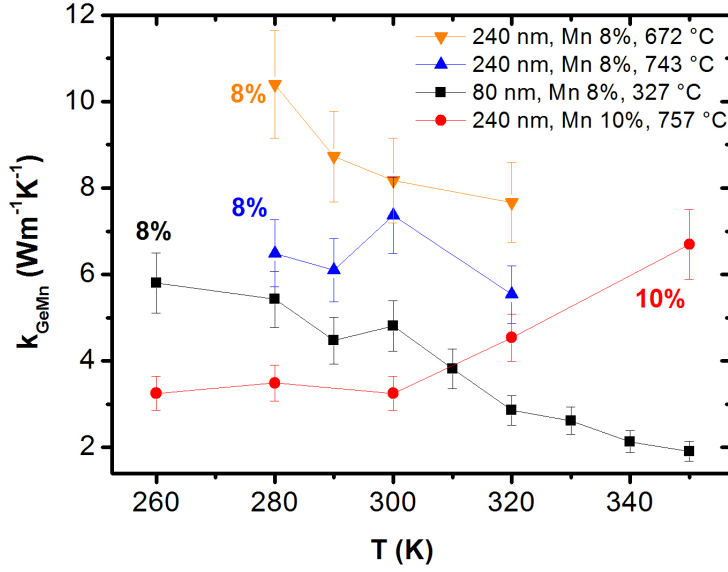


Figure 4.12: Experimental curves showing the temperature-dependent variation of the thermal conductivity of different Ge:Mn/GOI samples (i.e. containing different Mn concentrations or treated at different annealing temperatures).

4.4 SThM measurements: effective thermal conductivity of Ge:Mn

The experiments of SThM were carried out on the same Ge:Mn/GOI samples (that were measured previously by 3ω method), at CETHIL in Lyon with the help of Ali Assy. An extra Ge:Mn sample (6% Mn and $1 \mu\text{m}$ thick, noted as S0) grown on a Ge substrate, fabricated specifically for the SThM experiments, was measured as well.

Two sets of measurement have been done at different time with the same Wollaston probe at RT. They are mentioned as M1 and M2 in the following discussion. During each experiment, the probe voltages of V_{out} and V_{in} were registered when the probe is in air and in-contact with the sample surface, to calculate $\frac{\Delta P}{P}$ following equation 3.35, as

$$\frac{\Delta P}{P} = \frac{P_{in} - P_{out}}{P_{in}} = \frac{V_{in}^2 - V_{out}^2}{V_{in}^2}$$

Ge:Mn samples were measured together with the calibration samples. Each measurement includes the recording of the V_{out} value when the probe is in air with a fixed tip-sample distance of $400 \mu\text{m}$, and the recording of V_{in} once the probe is in contact with the sample surface. The recording of V_{out}/V_{in} pair has been repeated for around 10 times for each sample, and it is the mean values of V_{out} and V_{in} that will be used in further calculation.

Table 4.7 presents the experimental $\frac{\Delta P}{P}$ data for SThM calibration in experiment M1, using

4.4. SThM measurements: effective thermal conductivity of Ge:Mn

calibration sample	k (Wm ⁻¹ K ⁻¹)	$\frac{\Delta P}{P}$
SiO ₂	1.2	0.14563
ZrO ₂	2.5	0.16266
Ge	58.6	0.17013

Table 4.7: SThM experimental data for the calibration in experiment M1, using bulk SiO₂, ZrO₂ and Ge as reference samples.

Ge:Mn sample	S0	S2	S3	S7	S4	S5
Mn%	6	8	10	10	12	14
$T_{annealing}$ (°C)	-	672	709	757	703	716
M1: $k_{eff.}$ (Wm ⁻¹ K ⁻¹)	5.4	4.4	3.7	8.0	4	-
M2: $k_{eff.}$ (Wm ⁻¹ K ⁻¹)	-	7.6	3.9	5.1	5.1	4.3
$k_{3\omega}$ (Wm ⁻¹ K ⁻¹)	-	8.2	3.3	3.5	7.6	13

Table 4.8: SThM experimental thermal conductivity results (measurement M1 and M2) on different Ge:Mn samples (Ge:Mn/GOI series and sample S0) at RT, in comparison with 3ω measurement results on the same samples.

bulk SiO₂, ZrO₂ and Ge as reference samples. From the MATLAB calculation of equation 3.40 and 3.41, the mean values of probe-sample contact conductance \bar{G}_c and the tip-sample thermal exchange radius \bar{b}_{air} are obtained:

$$\bar{G}_c = 5.79 \times 10^{-6} \text{W/K} \quad \text{and} \quad \bar{b}_{air} = 5.88 \mu\text{m}$$

It should be noticed that as $\bar{b}_{air} = 5.88 \mu\text{m}$, the "probing depth" of the measurements is indeed larger than the total thickness of the top layers on Si substrate for a Ge:Mn/GOI sample, as well as for sample S0 where the thickness of Ge:Mn is $1 \mu\text{m}$. It shows that the thermal conductivities of Ge:Mn that obtained from the SThM experiments are in fact effective thermal conductivities.

Both sets of SThM experimental results are presented in table 4.8, and plotted in figure 4.13 together with the "V" shape curve of 3ω results for comparison. It can be noticed that the two sets of results show quite good coherence between them. Reduced effective thermal conductivities were found for all Ge:Mn samples, having values all below $6 \text{Wm}^{-1}\text{K}^{-1}$ at RT. These results confirmed the low thermal conductivity of Ge:Mn samples containing 10% Mn, that revealed by the 3ω experiments. However for Ge:Mn samples containing 6% or 14% Mn, important discrepancy can be noticed between the values found by SThM and that by 3ω measurements. This may due to the complexity of the SThM technique itself and the difficulties of the measurements: including the environmental influences, the deformation and pollution of the probe, the operation and etc. Further measurements using a new Wollaston probe would help to confirm the present results.

Even though the two sets of SThM results have dispersion and the absolute contribution of the

Ge:Mn layer can not be identified directly, the results still show that the Ge:Mn/GOI samples have very low thermal conductivities, and the Ge:Mn thin film maybe dominant as it is the very top layer that directly in contact with the thermal probe of SThM. Further work would be done to extract the absolute thermal conductivity values of Ge:Mn thin films, based on a multi-layer modeling. More SThM measurements using other type of micro-probes would be considered as well.

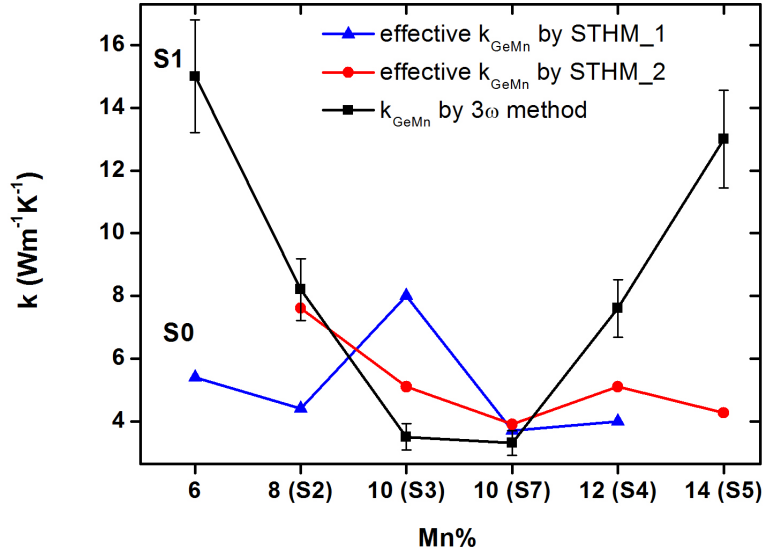


Figure 4.13: Plot of the SThM experimental thermal conductivity results of different Ge:Mn samples (Ge:Mn/GOI series and sample S0) as a function of Mn% (data in table 4.8), together with results of 3ω measurements (data in table 4.5).

4.5 Conclusion

Experimental measurements of the thermal conductivities of different Ge:Mn samples have been done using a differential 3-omega measurement setup and the scanning thermal microscopy. Systematic measurements have been performed at RT on a series of Ge:Mn/GOI samples, having different %Mn or annealed at different temperatures. The measurement results show dramatically reduced thermal conductivity values for all studied Ge:Mn samples, with a reduction of 4 to 20, compared to the value for Ge bulk at RT. A minimum thermal conductivity of $\sim 3 \text{ Wm}^{-1}\text{K}^{-1}$ has been found for Ge:Mn thin film grown with 10%Mn, beating the "alloy limit" set by $\text{Si}_{1-x}\text{Ge}_x$ at RT. It has also been evidenced that the annealing temperature has no significant influence on the thermal properties of the Ge:Mn thin films. However, these strong reductions of the thermal conductivity in Ge:Mn (compared to Ge) show that, the presence of nano-inclusions in the crystalline Ge matrix has indeed a significant influence on the phonon transport in the matrix. It can be predicted that the nano-inclusions create

more scatterings for phonons in Ge, resulting in a strong reduction of the phonon MFP. The studies on temperature-dependence of the Ge:Mn thermal conductivities reveal a remarkable decrease of thermal conductivity with temperature from 260K to 320K. The results should be confirmed by more temperature-dependent measurements, especially down to low temperatures. The SThM experimental results give the effective thermal conductivities for the studied Ge:Mn/GOI samples. The results show also small values of thermal conductivity for all Ge:Mn samples, below $6 \text{ Wm}^{-1}\text{K}^{-1}$ at RT, confirming the 3-omega measurement results in general sense.

To thoroughly understand the effect of nano-inclusions on the thermal transport properties of Ge:Mn thin film, and theoretically explain the physics behind all experimental results, numerical studies based on model simulation are required.

Des mesures expérimentales de la conductivité thermique de différents échantillons de Ge:Mn ont été effectuées en utilisant une configuration de mesure 3-oméga différentielle et la microscopie thermique à sonde locale. Des mesures systématiques ont été effectuées à la température ambiante sur une série d'échantillons de Ge:Mn sur substrat de GOI, ayant différents % de Mn ou recuit à des températures différentes. Les résultats de mesure montrent des valeurs de conductivité thermique considérablement réduites pour tous les échantillons de Ge:Mn étudiés, avec une réduction d'un facteur 4 à 20 par rapport à la valeur de Ge massif à température ambiante. Une conductivité thermique minimum de $\sim 3 \text{ Wm}^{-1}\text{K}^{-1}$ a été trouvée pour des films minces de Ge:Mn avec 10% de Mn. Cette valeur est en dessous de la limite d'alliage donnée par la conductivité thermique de $\text{Si}_{1-x}\text{Ge}_x$ à température ambiante.

Il a également été mis en évidence que la température de recuit n'a pas d'influence significative sur les propriétés thermiques des films minces de Ge: Mn. Cependant, ces fortes réductions de la conductivité thermique en Ge:Mn (par rapport au Ge) montrent que la présence de nano-inclusions a en effet une influence significative sur le transport des phonons dans la matrice cristalline de Ge. Les nano-inclusions créent ainsi plus d'événements de diffusion pour les phonons dans la matrice, ce qui implique une forte réduction du libre parcours moyen des phonons. Les études sur la dépendance en température de la conductivité thermique de Ge:Mn révèlent une diminution remarquable de conductivité thermique avec la température de 260K à 320K. Les résultats doivent être confirmés par d'autres mesures en température, en particulier à basses températures. Les résultats expérimentaux SThM montrent des valeurs de conductivité thermique effectives pour les échantillons de Ge:Mn/GOI étudiés. Ces résultats montrent également les petites valeurs de conductivité thermique pour tous les échantillons de Ge:Mn, à savoir des valeurs en dessous de $6 \text{ Wm}^{-1}\text{K}^{-1}$ à température ambiante, ce qui confirment les résultats de mesure 3-oméga.

Pour bien comprendre l'effet des nano-inclusions sur les propriétés de transport de chaleur dans les films minces de Ge:Mn, et pour expliquer théoriquement la physique sous-jacente aux résultats obtenus expérimentalement, une étude numérique basée est nécessaire.

5 Interpretation of the experimental results on Ge:Mn thin films

Résumé

Pour explorer théoriquement les propriétés de transport thermique des couches minces de Ge:Mn et pour essayer de comprendre les fortes réductions de la conductivité thermique des films minces de Ge:Mn présentées au chapitre 4, différents modèles théoriques existants ont été étudiés et appliqués. Dans ce chapitre, nous utiliserons d'abord un modèle purement géométrique développé par Minnich, pour les matériaux poreux. Puis, des modélisations numériques basées sur la solution de l'équation de transport de Boltzmann grâce au modèle de Callaway, seront adaptées au cas des couches minces de Ge:Mn.

To theoretically explore the thermal transport properties of the Ge:Mn nano-inclusion system, and to try to understand the dramatically decreased thermal conductivities for Ge:Mn thin films presented in chapter 4, different existing theoretical models have been studied and applied. In this chapter, discussion will include a first essay using a purely geometric model developed by Minnich, for porous materials. Then numerical modelings will be used based on the solution of the Boltzmann transport equation, including Callaway's model, Holland's model and refined Callaway/Holland's models.

5.1 Modeling of Ge:Mn thin film as a porous material

Considering the Ge:Mn thin film as a porous medium, a simple model developed by A. Minnich and G. Chen [111] has been firstly applied. Take a porous bulk medium containing organized identical spherical pores with a radius of $R = d/2$, while the diameter d is much smaller than the phonon MFP in the bulk medium. The porosity (ϕ) of a cubic volume L^3 of this material can be calculated using the relation:

$$\phi = \frac{4\pi R^3}{3L^3} \implies L^3 = \frac{\pi d^3}{6\phi} \quad (5.1)$$

Chapter 5. Interpretation of the experimental results on Ge:Mn thin films

Phonons are scattered at the surface of the pores, so the phonon MFP in this medium is actually the mean distance between two pores. The scattering of a phonon by a pore can be characterized through the effective scattering cross section σ , which is $\sigma = \pi R^2$ for a spherical pore. Then the phonon MFP can be expressed as:

$$\Lambda = \frac{L^3}{\sigma} = \frac{L^3}{\pi R^2} \quad (5.2)$$

With equation 5.1, the phonon MFP takes a final form of:

$$\Lambda = \frac{2d}{3\phi} \quad (5.3)$$

However, this formula is not correct as it does not give a value of zero for the maximum porosity of $\phi = 1$. Indeed, it needs to be corrected for a medium composed of two different materials [112], the matrix and the pore like in our case. Then the phonon MFP should be written as:

$$\Lambda_{matrix} = (1 - \phi)\Lambda_{ext} + \phi\Lambda_{int} \quad (5.4)$$

where Λ_{ext} and Λ_{int} are respectively the phonon MFP in the external material and the internal material, in the sense that the "internal" one is filled into the "external" one. So the ϕ can stand for porosity for porous medium, or the filling factor of the "internal" material for a matrix containing two materials.

For the porous medium, the Λ_{ext} takes the form of equation 5.5 and the Λ_{int} equals to zero as it refers to the air, so that the final phonon MFP in the material is:

$$\Lambda_{matrix} = \frac{2d}{3\phi}(1 - \phi) \quad (5.5)$$

This model has been then applied to Ge:Mn materials, being a matrix of Ge containing Ge_3Mn_5 nano-inclusions. In this case, the external material is Ge and the internal one is Ge_3Mn_5 , and the phonon MFP of the model can be written as:

$$\Lambda_{\text{Ge:Mn}} = (1 - \phi)\Lambda_{\text{Ge}} + \phi\Lambda_{\text{Ge}_3\text{Mn}_5} = \frac{2d}{3\phi}(1 - \phi) + \phi\Lambda_{\text{Ge}_3\text{Mn}_5} \quad (5.6)$$

Here ϕ is the filling factor of Ge_3Mn_5 nano-inclusions inside the Ge matrix.

As the diameter distribution of Ge_3Mn_5 nano-inclusions are within the range of 10 to 50 nm (smaller than the 200 nm for Λ_{Ge}), the phonon MFP inside the inclusions ($\Lambda_{\text{Ge}_3\text{Mn}_5}$) can

5.1. Modeling of Ge:Mn thin film as a porous material

Ge:Mn sample	S2	S3	S4	S5
Mn%	8	10	12	14
d (nm)	16.7	20.4	25.3	36.4
ϕ_{TEM} (%)	4.22	4.45	6.47	12.33
$\Lambda_{Minnich-TEM}$ (nm)	252.7	292.0	243.8	172.5
ϕ_{cal} (%)	12.8	16.4	19.7	23.2
$\Lambda_{Minnich-cal}$ (nm)	75.8	69.3	68.8	80.3
$k_{3\omega}$ ($\text{Wm}^{-1}\text{K}^{-1}$)	8.2	3.3	7.6	13
$\Lambda_{3\omega}$ (nm)	27	11	25	43

Table 5.1: Calculation results of phonon MFP for Ge:Mn thin films grown with different Mn concentrations, using Minnich model ($\Lambda_{Minnich}$) and the kinetic relation (equation 4.1) with 3ω experimental results ($\Lambda_{3\omega}$). $k_{3\omega}$ refers to experimental values of thermal conductivity for Ge:Mn samples obtained by 3ω measurements.

be estimated to be the inclusion diameter at a first approximation. However, as the nano-inclusion concentration is extremely small ($\sim 10^{21}$ - 10^{22} m^{-3} for all measured samples), the contribution of $\Lambda_{\text{Ge}_3\text{Mn}_5}$ in equation 5.6 can be neglected. So equation 5.5 is taken for the calculation for Ge:Mn cases.

For Ge:Mn/GOI samples, the values of inclusion mean diameter d are obtained from TEM observations (chapter 2). As to the inclusion filling factor, in our estimation, two sets of values are considered that have been obtained in different ways. From the TEM images the filling factor can be obtained by counting all visible inclusions inside a square of $700 \text{ nm} \times 700 \text{ nm}$. This filling factor will be referred to as ϕ_{TEM} in the following, and the phonon MFP of Ge:Mn calculated using ϕ_{TEM} in Minnich model is then $\Lambda_{Minnich-TEM}$. Another way is by calculation, taking the value of Mn concentration (8%, 10%, 12% or 14%) and the TEM distribution graph of each Ge:Mn sample. The obtained filling factor in this way and phonon MFP using Minnich model, are respectively ϕ_{cal} and $\Lambda_{Minnich-cal}$.

As has already been discussed in chapter 4, a set of Ge:Mn phonon MFP has been calculated using the kinetic theory (equation 4.1) based on the 3ω experimental results (referred to as $\Lambda_{3\omega}$). Hence, the three sets of above mentioned Ge:Mn phonon MFP values have been compared all together in table 5.1. The values of $\Lambda_{Minnich-TEM}$ are found to be around 200 nm for all Ge:Mn samples, in the range of Ge phonon MFP at RT, whereas the values of $\Lambda_{Minnich-cal}$ are three to four times smaller.

The plots of the results $\Lambda_{Minnich-cal}$ and $\Lambda_{3\omega}$ as a function of Mn concentration are then presented in figure 5.1. Surprisingly, from the plots, a "V" shape is also found for phonon MFP values $\Lambda_{Minnich-cal}$ by Minnich model, similar to the trend of experimental results $k_{\text{Ge:Mn}}$ as well as the calculated $\Lambda_{3\omega}$ based on the results. However, the $\Lambda_{Minnich-cal}$ and $\Lambda_{3\omega}$ results still do not match themselves. The $\Lambda_{Minnich}$ presents values about three times higher than the $\Lambda_{3\omega}$ extracted from the measurement results. It is then evident that the Minnich model for porous media does not represent correctly the Ge:Mn nano-inclusion system. The fact

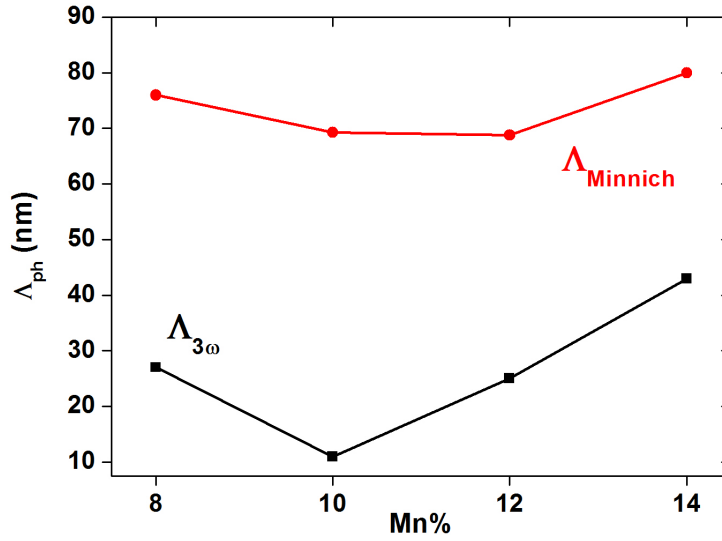


Figure 5.1: The plots of calculated phonon MFP values as a function of Mn concentration, using Minnich model ($\Lambda_{Minnich}$) and the kinetic relation with 3ω measurement results ($\Lambda_{3\omega}$).

seems even that, the Ge:Mn inclusion material appears to be a more efficient medium for reducing the phonon MFP, compared to an arranged porous system with pores in one unique diameter. This may be due to the fact that the nano-inclusions in Ge:Mn material are not uniformly tailored, they have a diameter distribution spread within a certain range. As a result, the distance between two nano-inclusions may also have a distribution, resulting in a better efficiency for the scattering of phonons within a relatively large phonon wavelength range.

5.2 Modeling of thermal conductivity of Ge:Mn based on Boltzmann transport equation

In order to simulate the influence of the diameter distribution of Ge_3Mn_5 nano-inclusions on the overall phonon transport properties, numerical modeling on Ge:Mn samples have been done based on the resolution of the Boltzmann transport equation.

As demonstrated in chapter 1, explanations using phonon scattering for the temperature dependence of the thermal conductivity of a material, correspond well with experimental results (figure 1.9). However, to refine and expand the theory in order to make quantitative calculation, assumptions and approximations have been introduced. Besides the relaxation time approximation introduced to the BTE (see chapter 1), the calculation of the scattering cross section is required. Difficulties are also present in developing relaxation time expressions for each scattering process, with their own temperature and frequency dependences.

5.2. Modeling of thermal conductivity of Ge:Mn based on Boltzmann transport equation

Especially for phonon-phonon scatterings (N- and U-processes), the relaxation times are strongly dependent on phonon branch and on the dispersion of the phonon spectrum. As a result, approximated relaxation time expressions may only be valid for limited phonons or limited temperature ranges.

One more thing to note is that, the simple addition of reciprocal relaxation time using Matthiessen rule may not be necessarily true, that is to say, the scattering processes are not necessarily independent eventually .

In this chapter, we will discuss two principle modeling methods for the simulation of phonon transport in a material: Callaway's model and Holland's model. The refinement of the two models will be discussed as well, and two modified Callaway/Holland models will be presented. For the simulation work of the Ge:Mn system, both Holland's model and one of the modified Callaway/Holland model have been applied. An additional relaxation rate introduced specifically by nano-inclusions was considered as well in the model, which has been proposed by Kim and Majumdar in their studies on ErAs/InGaAs nano-inclusion system.

5.2.1 Callaway's model

Basic description

This model has been developed by Callaway in 1959 [113], as an analytical solution for the expression of lattice thermal conductivity in isotropic materials at low temperature. It is assumed that each phonon scattering process can be represented by relaxation times which depend on frequency and temperature. Four scattering processes have been considered: impurity scattering (I), boundary scattering (B), normal process (N) and Umklapp process (U). The relaxation times for the four scattering processes is then noted as: τ_I , τ_B , τ_N and τ_U in the calculation.

The model also assumes:

- (1) no distinction of phonon polarization (between longitudinal and transverse);
- (2) one average sound velocity v_B ;
- (3) the relaxation rate $\tau_N^{-1} = B_1\omega^2 T^3$ considered in the calculation is only valid for low-frequency longitudinal phonons;
- (4) the U-process has a relaxation rate similar to the one for N-process: $\tau_U^{-1} = B_2\omega^2 T^3$, with B_1 containing an exponential temperature factor.

One special investigation of this model focuses on the role of the N-process. When all reciprocal relaxation times are summed up (τ_C^{-1}) to represent all phonon scattering processes according to Matthiessen rule, this total scattering rate τ_C^{-1} cannot be used as a whole for a calculation of a finite thermal conductivity of the material, due to the fact that the N-process is not resistive for phonon transport, thus does not contribute to the thermal resistance. The τ_C^{-1} should be identified as the sum of the non-resistive (elastic) relaxation rate τ_N^{-1} , and the resis-

Chapter 5. Interpretation of the experimental results on Ge:Mn thin films

tive (non-elastic) relaxation rate τ_R^{-1} . The latter is the sum of all resistive scattering processes including impurity scattering, boundary scattering and U-process, so that:

$$\tau_C^{-1} = \tau_N^{-1} + \tau_R^{-1}, \quad \text{and} \quad \tau_R^{-1} = \tau_I^{-1} + \tau_B^{-1} + \tau_U^{-1} \quad (5.7)$$

The total thermal conductivity k of the material is then written as:

$$k = k_1 + k_2 \quad (5.8)$$

where k_1 and k_2 are defined as:

$$k_1 = CT^3 \int_0^{T_D/T} \tau_C(x) J(x) dx \quad (5.9)$$

$$k_2 = CT^3 \frac{\left[\int_0^{T_D/T} \frac{\tau_C(x)}{\tau_N(x)} J(x) dx \right]^2}{\int_0^{T_D/T} \frac{\tau_C(x)}{\tau_N(x)\tau_R(x)} J(x) dx} \quad (5.10)$$

with

$$J_x = \frac{x^4 e^x}{(e^x - 1)^2}, \quad \text{and} \quad \frac{1}{\tau_C(x)} = \frac{1}{\tau_N(x)} + \frac{1}{\tau_R(x)}, \quad (5.11)$$

and

$$x = \frac{\hbar\omega}{k_B T}, \quad m = \frac{k_B}{\hbar}, \quad C = \frac{k_B m^3}{2\pi^2 v_B} \quad (5.12)$$

Here the k_1 counts all scattering processes as if they were entirely resistive; whereas k_2 permits the exclusion and the correct treatment of the N-process counting its non-resistive nature. It should be noted that, in the majority of cases the resistive scattering processes dominates, that $\tau_N \gg \tau_R$ and $\tau_C \approx \tau_R$, so $k_2 \ll k_1$ and only k_1 term is used. This is only acceptable for crystals with important impurity concentration and defects. However, for isotopically pure and defect-free samples, the N-process becomes comparable to resistive processes even dominant, that $\tau_N \approx \tau_R$, k_2 then contribute significantly to the total thermal conductivity. So the magnitude of k_2 is essentially controlled by the concentration of impurities in the crystal.

k_1 counts all scattering processes as inelastic, including N-process. But as energy is conserved in a N-process, it is in fact an elastic scattering. Then it is important to use k_2 to correct the over-estimated inelastic scatterings in k_1 .

5.2. Modeling of thermal conductivity of Ge:Mn based on Boltzmann transport equation

Relaxation rates determination

The relaxation rates for different scattering processes are then identified. For impurity (I) scattering, either from atoms of different mass, different isotopes, or different elements with similar force constant, the scattering rate is analyzed by Klemens [114] based on the Rayleigh scattering theory for photons:

$$\tau_I^{-1} = A\omega^4, \quad A = \frac{gV}{4\pi\nu_B^3} \quad (5.13)$$

where A is a constant depending on: the mass variance g , the volume per atom V and the sound velocity ν_B .

Boundary scattering dominates at low temperature. It is determined by the geometrical size and the surface condition of the sample. Its scattering rate can be written as [115]:

$$\tau_B^{-1} = \frac{\nu_B}{L_E} \quad (5.14)$$

where L_E is the effective phonon mean free path, which represents the effect of sample size, geometry, aspect ratio (length-to-thickness) and surface roughness, etc. It can be determined from low temperature experimental data.

Relaxation rates for N-process and U-process are assumed to be:

$$\tau_N^{-1} = B_2\omega^2 T^3, \quad \text{and} \quad \tau_U^{-1} = B_1\omega^2 T^3 \quad (5.15)$$

where B_1 and B_2 are constant fitting parameters, determined by fitting the temperature dependence curve of the thermal conductivity of the material.

5.2.2 Holland's model

The Holland's model was developed and proposed by Holland in 1963 [116]. In this approach, the heat flow is divided into two parts: one part carried by transverse phonons and the other one by longitudinal phonons. The two polarizations of phonons are then considered separately in the N-process. This model is under the assumption that the k_2 term (from Callaway's model) is zero, valid for cases where resistive scattering processes are dominant over N-process. So the thermal conductivity concerns only k_1 in Callaway's model, and is divided into two parts:

$$k = k_T + k_L \quad (5.16)$$

where

$$k_T = \frac{2}{3} \int_0^{\theta_T/T} \frac{C_T T^3 x^4 e^x (e^x - 1)^{-2} dx}{\tau_T^{-1}} \quad (5.17)$$

$$k_L = \frac{1}{3} \int_0^{\theta_L/T} \frac{C_L T^3 x^4 e^x (e^x - 1)^{-2} dx}{\tau_L^{-1}} \quad (5.18)$$

and

$$x = \frac{\hbar\omega}{k_B T}, \quad i = T, L, \quad \theta_i = \frac{k_B \omega_i}{\hbar}, \quad C_i = \frac{k_B}{2\pi^2 v_i} \left(\frac{k_B}{\hbar}\right)^3 \quad (5.19)$$

The subscripts T and L represent respectively the transverse phonon polarization and longitudinal phonon polarization. θ_T and θ_L are Debye temperatures appropriate for transverse and longitudinal phonon branches. v_T and v_L are distinguished sound velocities for transverse and longitudinal phonons separately, which can be obtained from elastic constant measurements [117].

The temperature and frequency dependence of relaxations rates for N-process and U-process are then chosen to be:

$$\tau_{TN}^{-1} = B_{TN} \omega T^4, \quad \tau_{LN}^{-1} = B_{LN} \omega^2 T^3 \quad (5.20)$$

and

$$\tau_{TU}^{-1} = \begin{cases} \frac{B_{TU} \omega^2}{\sinh(x)} & \omega_1 < \omega < \omega_2 \\ 0 & \omega < \omega_1 \end{cases} \quad (5.21)$$

So that

$$\tau_T^{-1} = \tau_B^{-1} + \tau_I^{-1} + \tau_{TN}^{-1} + \tau_{TU}^{-1} \quad (5.22)$$

$$\tau_L^{-1} = \tau_B^{-1} + \tau_I^{-1} + \tau_{LN}^{-1} \quad (5.23)$$

and the total thermal conductivity k can then be summed up:

$$k = k_T + k_{TU} + k_L \quad (5.24)$$

5.2. Modeling of thermal conductivity of Ge:Mn based on Boltzmann transport equation

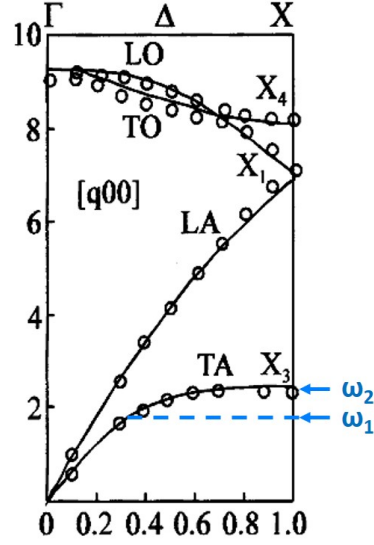


Figure 5.2: Phonon dispersion curves for Ge [13] with additional indications of frequency positions ω_1 and ω_2 introduced by Holland's model.

where

$$k_T = \frac{2}{3} T^3 \int_0^{\theta_1/T} \frac{C_T x^4 e^x (e^x - 1)^{-2} dx}{v_B/L_E + \alpha x^4 T^4 + \beta_T x T^5}, \quad \text{for } \omega < \omega_1 \quad (5.25)$$

$$k_{TU} = \frac{2}{3} T^3 \int_{\theta_1/T}^{\theta_2/T} \frac{C_T x^4 e^x (e^x - 1)^{-2} dx}{v_B/L_E + \alpha x^4 T^4 + \beta_{TU} x^2 T^2 / \sinh x}, \quad \text{for } \omega_1 < \omega < \omega_2 \quad (5.26)$$

$$k_L = \frac{1}{3} T^3 \int_0^{\theta_2/T} \frac{C_L x^4 e^x (e^x - 1)^{-2} dx}{v_B/L_E + \alpha x^4 T^4 + \beta_L x^2 T^5} \quad (5.27)$$

and

$$\alpha = A \left(\frac{k_B}{\hbar} \right)^4, \quad \beta_i = B_i \left(\frac{k_B}{\hbar} \right)^2 \quad (5.28)$$

In the calculation, the transverse acoustic branch is split into two parts by the frequency ω_1 . The position of frequencies ω_1 and ω_2 in the dispersion curves of Ge, are indicated in figure 5.2. It shows that the k_T term in equation 5.25 is the sum of the contribution of low-frequency acoustic transverse modes within $\omega < \omega_1$. The ω_1 is the phonon frequency limit at which the U-processes start to happen, so the k_{TU} term in equation 5.26 is the contribution of the transverse modes with frequencies between ω_1 and ω_2 , while ω_2 is the maximum frequency limit for acoustic transverse modes.

Chapter 5. Interpretation of the experimental results on Ge:Mn thin films

The sound velocity v_B in the relaxation rate terms of τ_B^{-1} and τ_I^{-1} is the same average value. If attempt of distinguished v_T and v_L should be made, an approximation of this v_B is:

$$v_B^{-1} = \frac{1}{3} (2v_T^{-1} + v_L^{-1}) \quad (5.29)$$

The greatest advantage of this model is that, as all scattering processes are considered resistive, the relaxation time for each process can also be seen as the phonon "lifetime" due to the process. However, this model has its own limitations, most importantly is the neglect of the term k_2 from the total thermal conductivity, so that it can not be applied to all samples; secondly, the absence of terms representing the influence of N-processes on other scattering processes; and thirdly, the neglect of contribution of longitudinal modes to U-processes, i.e. the τ_{LU} .

Refinement of Callaway/Holland's model

Comparing to Holland's model, Callaway's model is indeed more reasonable where both k_1 and k_2 are included. However, the neglect of longitudinal U-processes makes the model only suitable for low temperature cases. It is indeed the longitudinal U-processes that are crucial at higher temperatures ($T > 100\text{K}$) to inhibit the thermal conductivity from increasing to infinity. Works on the refinement of Callaway's model have then been developed recently.

One of the modified Callaway/Holland model we would like to discuss is the one proposed by Asen-Palmer et al. in 1997 [12]. In this modified model, both k_1 and k_2 are kept and the distinction between the transverse (2T) and longitudinal (L) modes from Holland's model are conserved. However, the splitting of the transverse acoustic branch into two frequency regions is not considered. Furthermore, the parameter B_{LU} is introduced to include the longitudinal U-processes.

The temperature and frequency dependence of U-process relaxation rates are also found to be better to take an exponential form as [118, 119, 120]:

$$\tau_{TU}^{-1} = B_{TU}\omega^2 T e^{-C_T/T}, \quad \text{and} \quad \tau_{LU}^{-1} = B_{LU}\omega^2 T e^{-C_L/T} \quad (5.30)$$

where C_T and C_L are two Umklapp scattering exponents for transverse and longitudinal phonons in U-processes.

In total, this modified model involves six fitting parameters: B_{TN} , B_{LN} , B_{TU} , B_{LU} , C_T and C_L , for the determination of the thermal conductivity of a given sample, independent of its isotopic concentration. This model has been proved to be highly in agreement with experimental data on isotopically modified Ge samples, within the temperature range of 2K - 300K. It describes reasonably well the Ge thermal conductivity as a function of isotopic concentration.

5.2. Modeling of thermal conductivity of Ge:Mn based on Boltzmann transport equation

A similar modified Callaway/Holland model has been proposed by Morelli [121] following the approach of Asen-Palmer. It has been developed to study the isotope effect on thermal conductivity of Ge, Si and diamond. In this model, the original consideration is to distinguish longitudinal and transverse modes in impurity scattering and boundary scattering processes. So instead of using one same sound velocity v_B as in Callaway's model, v_L and v_T are applied here to separately describe the contributions of longitudinal and transverse modes to the relaxation rates of τ_I^{-1} and τ_B^{-1} . Moreover, this approach permits to link the fitting parameters B_{TN} and B_{LN} to the physical properties of the material including Grüneisen parameter.

For impurity scattering, with conserved temperature and frequency dependence (as in Callaway's model), the relaxations rates are now:

$$\tau_{IL}^{-1} = \frac{\Gamma V}{4\pi v_L^3} \omega^4, \quad \text{and} \quad \tau_{IT}^{-1} = \frac{\Gamma V}{4\pi v_T^3} \omega^4 \quad (5.31)$$

Γ is the mass-fluctuation scattering parameter for a single element made up of several natural isotopes:

$$\Gamma = \sum_i c_i \left[\frac{m_i - \bar{m}}{\bar{m}} \right]^2, \quad \text{with} \quad \bar{m} = \sum_i c_i m_i \quad (5.32)$$

where m_i the atomic mass of the isotope i and c_i the fractional atomic natural abundance of the element.

The boundary scattering rates, always independent of temperature and frequency, are given by:

$$\tau_{BL}^{-1} = \frac{v_L}{L_E}, \quad \text{and} \quad \tau_{BT}^{-1} = \frac{v_T}{L_E} \quad (5.33)$$

So following Callaways integrals of k_1 and k_2 (equations 5.9 and 5.10), while considering one longitudinal (k_L) and two degenerate transverse (k_T) phonon branches, the total thermal conductivity is summed up as:

$$k = k_L + 2k_T \quad (5.34)$$

with

$$k_L = k_{L1} + k_{L2}, \quad \text{and} \quad k_T = k_{T1} + k_{T2} \quad (5.35)$$

In Morelli's work using this model, the simulation results were found to be in good agreement with experimental data for Ge and diamond: in the magnitude and temperature-dependance

of the thermal conductivity, as well as the magnitude of the thermal conductivity with isotopic effect. The results were obtained with only a limited set of fitting parameters.

For the simulation work of Ge:Mn thin films, Holland's model and both above discussed modified Callaway/Holland models have been applied.

5.2.3 Introduction of τ_{NI}^{-1} for nano-inclusion material system

For the study of the phonon scattering contribution of embedded nano-inclusions in the thermal conductivity of the material, an analytical approach has been developed by Kim and Majumdar [122] for the estimation of the phonon scattering cross-section of polydispersed spherical nano-inclusions in solids.

For phonon scattering by nano-inclusions (NI), the relaxation time τ_{NI} is related to the scattering cross section σ :

$$\tau_{NI} = \frac{1}{Cv\sigma} \quad (5.36)$$

where C is the inclusion concentration (or volume density) in unit m^{-3} , and v the group velocity of phonons.

For the estimation of the scattering cross section σ of spherical nano-inclusions, a simple expression has been proposed by Majumdar [81]:

$$\sigma = \pi R^2 \left(\frac{\chi^4}{\chi^4 + 1} \right) \quad (5.37)$$

where R is the radius of the spherical nano-inclusions, and χ a size parameter, defined as $\chi = qR$ where q is the incoming wave vector.

There are two extremes for the scattering processes:

- (1) when $\chi \ll 1$, the inclusions are much smaller than the wavelength. The Rayleigh law can be applied and the scattering cross section obeys a dependence in f^4 with frequency f ;
- (2) when the size parameter χ approaches infinity, known as the geometrical scattering regime, the scattering cross section is $\sigma \approx \pi R^2$, thus independent of frequency f .

The scattering efficiency is defined as the scattering cross section divided by the projection area of the spherical inclusion. It can then be expressed as a function of the size parameter χ for both Rayleigh and near-geometrical scattering regimes, as plotted in figure 5.3. It can be noticed that, Rayleigh scatterings are valid only at very small values of χ ($\chi < 10$). For size parameter bigger than 40, it is the geometrical scattering that dominates.

5.2. Modeling of thermal conductivity of Ge:Mn based on Boltzmann transport equation

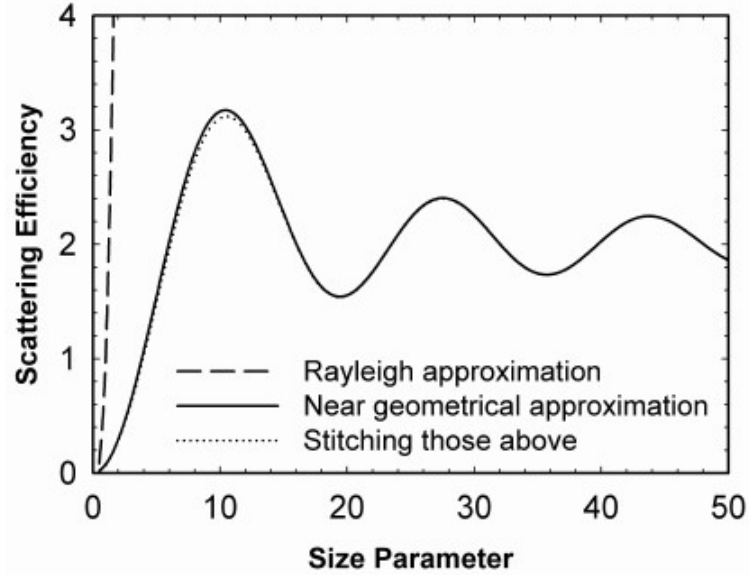


Figure 5.3: The scattering efficiency of the spherical impurity as a function of size parameter, for Rayleigh, near-geometrical regimes and the combination of the two [52].

As for the case of Ge:Mn system, taking the phonon wavelength of 1nm in Ge at RT (from figure 1.6 in chapter 1), and the radius of Ge_3Mn_5 nano-inclusions $R = 10$ nm (from table 2.1 in chapter 2), the calculated size parameter is $\chi \sim 63$. This value is well in the near-geometrical regime as shown in figure 5.3. It is then considered that the scattering by nano-inclusions in Ge:Mn system are geometrical, so that $\sigma \approx \pi R^2$.

In geometrical scattering regime where $\chi \rightarrow \infty$, scatterings are most likely in the forward direction. As the acoustic impedance mismatch between the host medium and the nano-inclusion material is not large, which is the general case for solid-solid interface, the backscattering is negligible. The scattering cross section can then be derived from the forward scattering amplitude.

To represent the diameter distribution of the nano-inclusions, a statistical distribution function, the gamma function has been chosen. Using the shape-scale parametrization, the probability density function of inclusion radius R is:

$$g(R; A, B) = \frac{x^{A-1} e^{-\frac{x}{B}}}{B^A \Gamma(A)} \quad (5.38)$$

where A and B are respectively the scale and shape parameters, and $\Gamma(A)$ is the gamma function evaluated at A .

Chapter 5. Interpretation of the experimental results on Ge:Mn thin films

The nano-inclusion scattering cross section is then:

$$\sigma_{NI} = \int_0^{\infty} \pi R^2 \left(\frac{\sigma_{total}}{\pi R^2} \right) \left(\frac{R^{A-1} e^{-R/B}}{B^A \Gamma(A)} \right) dR \quad (5.39)$$

Since the gamma distribution deals with only positive numbers, it is possible to have the standard deviation larger than the mean diameter of the nano-inclusions. Due to diffraction, scatterings can occur near the edge of the inclusions, so an increasing standard deviation can result in an increase in the scattering cross section that is based on the mean diameter. As a result, for nano-inclusions with large size parameter, the scattering cross section can reach twice the geometrical projection area of the inclusion (πR^2). So that $\sigma = 2\pi R^2$. This approximation then makes the final expression for σ_{NI} as:

$$\sigma_{NI} = \int_0^{\infty} R^2 \left(\frac{R^{A-1} e^{-R/B}}{B^A \Gamma(A)} \right) dR = \int_0^{\infty} R^2 g(R) dR \quad (5.40)$$

Further on, as the variance (square of the standard deviation s) is defined as:

$$s^2 = variance = \int_0^{\infty} R^2 g(R) dR - r^2 \quad (5.41)$$

where r is the mean radius of spherical nano-particles, the σ_{NI} finally takes the form of:

$$\sigma_{NI} = r^2 + s^2 \quad (5.42)$$

From the parameters A and B of Gamma distribution, the mean radius (r) and the variance (s^2) of the nano-inclusions are calculated as $r = A \times B$ and $s^2 = A \times B^2$.

The relaxation rate of the nano-inclusion scattering τ_{NI}^{-1} is then calculated as:

$$\tau_{NI}^{-1} = Cv\sigma = Cv \frac{\int_0^{\infty} \sigma_{NI}(\omega, R) g(R) dR}{\int_0^{\infty} g(R) dR} \quad (5.43)$$

where $\sigma_{NI}(\omega, R)$ is the scattering cross section introduced by nano-inclusions, as a function of phonon frequency ω and the inclusion radius R .

Simulations have been done on ErAs embedded $\text{In}_{0.53}\text{Ga}_{0.47}\text{As}$ alloy samples, based on Callaway's model considering the additional relaxation rate introduced by nano-inclusions τ_{NI}^{-1} [43]. Good agreement has been found between the simulation predictions and experimental data of thermal conductivity of the ErAs/InGaAs nano-inclusion system [43], proving that the proposed solution for σ_{NI} (equation 5.42) is valid for the case of a nano-inclusion in alloy material.

5.2. Modeling of thermal conductivity of Ge:Mn based on Boltzmann transport equation

5.2.4 Simulation results on Ge:Mn

Coming to the Ge:Mn nano-inclusion system, we have applied Holland's model and both modified Callaway/Holland models (developed by Asen-Palmer and Morelli separately) for the simulation. We also take into account the relaxation rate τ_{NI}^{-1} that is introduced by Ge_3Mn_5 nano-inclusions in the modeling. For the simulation work, Ge:Mn/GOI samples grown with different manganese concentrations have been studied. The simulation is done using Python numerical tools, and the modelings are developed by Dr. Dimitri Tainoff in our group.

The total relaxation rate τ_C in the Ge:Mn system is:

$$\tau_C^{-1} = \tau_B^{-1} + \tau_I^{-1} + \tau_N^{-1} + \tau_U^{-1} + \tau_{NI}^{-1} \quad (5.44)$$

In the calculation of τ_{NI}^{-1} using equation 5.42, the inclusion mean radius r and the standard deviation s are calculated from the parameter A and B in gamma distribution function through the fitting of the TEM inclusion distribution graphs. For the inclusion concentration C of Ge:Mn samples, two sets of values have been considered: the values obtained from the TEM

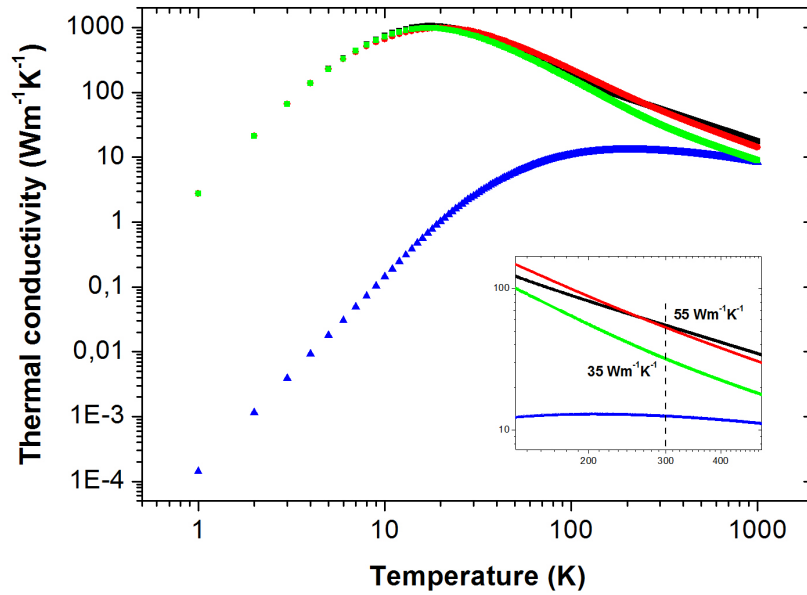


Figure 5.4: Simulation curves of Ge bulk thermal conductivity as a function of temperature using Asen-Palmer (in red), Morelli (in black) and Holland's (in green) models. The curve in blue color is the simulation result obtained from Ge:Mn sample containing 10% Mn using concentration value C_{cal} in Morelli's model. The inset graph is a zoom of the curves at temperature around 300K.

Chapter 5. Interpretation of the experimental results on Ge:Mn thin films

observation/analysis (C_{TEM}) and the ones by calculation ($C_{cal.}$). The values have already been presented table 2.1) in chapter 2.

Simulation of Ge bulk using the three models have been applied firstly in order to validate the modelings. In figure 5.4, it can be seen that the simulation curves of Ge bulk thermal conductivity as a function of temperature using the three models (in color red, green and black separately) overlap nicely between themselves. They are identical compared to the curves obtained in the work of Asen-Palmer and Morelli, and show a good agreement with the experimental curves in figure 1.9 (chapter 1) as well. However, it can be noticed that for Ge at higher temperatures ($> 200K$) the Holland's model gives underestimated values. At 300K, the Ge thermal conductivity given by Asen-Palmer and Morelli's models is around $55 \text{ Wm}^{-1}\text{K}^{-1}$, while the value from Holland's model is $35 \text{ Wm}^{-1}\text{K}^{-1}$.

A simulation curve (in color blue) of sample Ge:Mn containing 10% Mn using concentration value $C_{cal.}$ in Morelli's model is also plotted in figure 5.4. The flat trend of the curve for temperature $> 100 \text{ K}$ is a typical feature for glassy solids [123, 124].

The simulation results on RT thermal conductivities of different Ge:Mn thin films using both sets of inclusion concentrations and three models, are presented together for comparison in table 5.2. Different points can be noticed from the table. Firstly as the inclusion concentration

Sample	S2	S3	S4	S5
Mn%	8	10	12	14
A	8.92	6.15	4.39	2.92
B (nm)	0.93	1.57	2.85	6.24
$r = A \times B$ (nm)	8.3	9.6	13	18
$s^2 = A \times B^2$ (nm ²)	7.7	15	37	112
C_{TEM} (m ⁻³)	$1.3 \cdot 10^{22}$	$6.1 \cdot 10^{21}$	$4.5 \cdot 10^{21}$	$2.6 \cdot 10^{21}$
k_{Asen} (Wm ⁻¹ K ⁻¹)	11.2	12.5	11.6	10.7
$k_{Morelli}$ (Wm ⁻¹ K ⁻¹)	18.6	21.2	19.5	17.8
$k_{Holland}$ (Wm ⁻¹ K ⁻¹)	6.7	7.7	7.1	6.3
$C_{cal.}$ (m ⁻³)	$3.91 \cdot 10^{22}$	$2.19 \cdot 10^{22}$	$1.35 \cdot 10^{22}$	$4.6 \cdot 10^{21}$
k_{Asen} (Wm ⁻¹ K ⁻¹)	7.2	8	7.7	8.5
$k_{Morelli}$ (Wm ⁻¹ K ⁻¹)	10.9	12.5	11.9	13.6
$k_{Holland}$ (Wm ⁻¹ K ⁻¹)	4.4	4.8	4.7	5.1

Table 5.2: Simulation results of thermal conductivities of Ge:Mn samples grown with different Mn concentrations, using both modified Callaway/Holland's models mentioned in the text and the Holland's model. The results are indicated as k_{Asen} , $k_{Morelli}$ and $k_{Holland}$. A and B are respectively the shape parameter and scale parameter from a Gamma distribution treatment of the TEM distribution graphs of nano-inclusions in Ge:Mn. The mean radius r and the variance s^2 are calculated as $A \times B$ and $A \times B^2$ respectively. One should notice that these mean radii and standard deviation values for Ge:Mn samples are not the same as in table 2.1 in chapter 2, where Gaussian fit has been applied.

5.2. Modeling of thermal conductivity of Ge:Mn based on Boltzmann transport equation

values of $C_{cal.}$ are larger than that of C_{TEM} , the simulated thermal conductivities using $C_{cal.}$ are as a result smaller in both Asen-Palmer and Morelli models. As it has been doubted in chapter 2 that the counting method based on TEM images that used for the calculation of the $C_{cal.}$ may underestimate the total inclusion volume thus the inclusion concentration, the simulation results using $C_{cal.}$ values are considered more reliable. Then from the results of the three models using $C_{cal.}$, it can be noticed that Morelli's model gave the highest thermal conductivity values between 11-14 $\text{Wm}^{-1}\text{K}^{-1}$, while Holland's model gave the lowest ones within the range of 4-5 $\text{Wm}^{-1}\text{K}^{-1}$ for all studied Ge:Mn samples. However, it should be reminded that the Holland's model may give underestimated results at RT as shown in previous simulation curves of Ge bulk (figure 5.4).

A plot of the three sets of results are presented in figure 5.5, together with the "V" shape 3-omega experimental curve of Ge:Mn thermal conductivity as a function of Mn%. From the figure it can be seen that, unlike the remarkable "V" shape in the experimental results, the simulated thermal conductivities as a function of Mn% obtained from the three models all show a general flat trend.

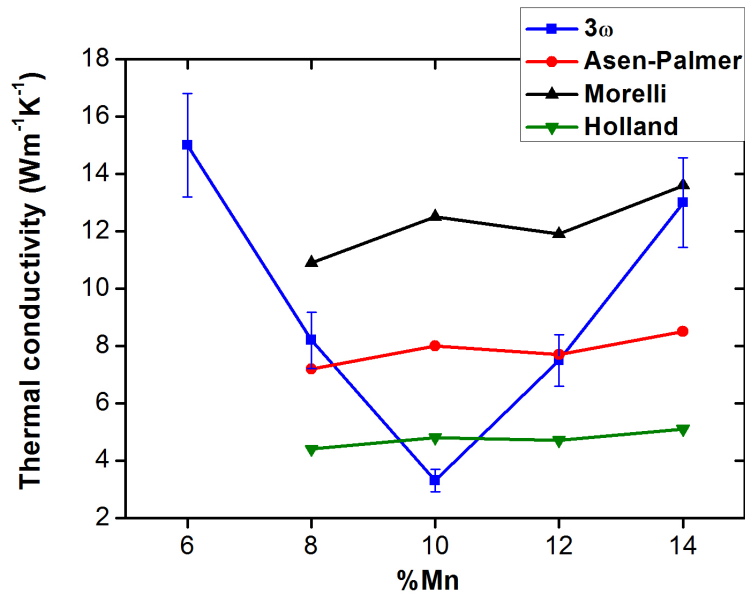


Figure 5.5: Plots of simulation results of Ge:Mn thermal conductivity as a function of Mn concentration using concentration value $C_{cal.}$ in Asen-Palmer (in red), Morelli (in black) and Holland's (in green) models, in comparison with the "V" shape 3-omega experimental curve of Ge:Mn thermal conductivity as a function of Mn% in color blue.

5.3 Conclusion

The simulation results based on the calculated inclusion concentration values $C_{cal.}$ using different models, show reduced thermal conductivity values for all studied Ge:Mn samples: containing Mn concentration of 6%-14%. All simulated thermal conductivities are below $16 \text{ Wm}^{-1}\text{K}^{-1}$ at RT. Values of $4\text{-}5 \text{ Wm}^{-1}\text{K}^{-1}$ are given by Holland's model, which are very close to the minimum thermal conductivity for sample Ge:Mn with 10%Mn that revealed by 3-omega measurements. However, instead of a "V" shape trend revealed by 3-omega results, the variation of Ge:Mn thermal conductivity with the Mn% by simulation is more or less flat. These results are still very encouraging which showed us the possibility of achieving a theoretical path to explain the experimental results on Ge:Mn. Further simulation work will be continued to complete the investigation of this nano-inclusion embedded Ge:Mn system.

Les résultats de simulation en utilisant différents modèles et basés sur les valeurs de concentration d'inclusion calculées $C_{cal.}$, montrent une réduction des valeurs de conductivité thermique pour tous les échantillons de Ge:Mn étudiés: contenant une concentration de Mn de 6%-14%. Toutes les valeurs simulées de conductivité thermique sont en dessous de $16 \text{ Wm}^{-1}\text{K}^{-1}$ à température ambiante. Les valeurs de $4\text{-}5 \text{ Wm}^{-1}\text{K}^{-1}$ sont données par le modèle de Hollande. Ces valeurs sont très proches de la conductivité thermique minimale révélée par les mesures 3-oméga, pour les échantillons de Ge:Mn comprenant 10% de Mn. Cependant, au lieu d'une tendance de forme de "V" mesurée expérimentalement en 3-omega, la variation de la conductivité thermique de Ge:Mn avec la concentration de Mn est plus ou moins plate. Ces résultats restent très encourageants et ouvrent la voie à d'autres investigations théoriques à venir pour expliquer plus quantitativement la spectaculaire diminution conductivité thermique mesurée dans les couches minces de Ge:Mn.

6 Experimental results on other nano-structured thermoelectric materials

Résumé

La méthode 3-oméga, hautement sensible, développée dans ce travail de thèse, a également été appliquée à la mesure de la conductivité thermique d'autres matériaux innovants, sous forme de couche mince thermoélectriques. Dans ce chapitre, nous présentons les résultats obtenus sur deux types de matériaux thermoélectriques différents: un film mince de $\text{Ge}_x\text{Sn}_{1-x}\text{Mn}$ épitaxié et une membrane poreuse de Al_2O_3 remplie de nanofils de Bi_2Te_3 . Pour une confirmation des résultats, les mesures par SThM ont également été effectuées sur les échantillons de membrane de Al_2O_3 .

Taking the benefit of the home-made highly sensitive 3-omega setup, thermal conductivity measurements on some other potential thermoelectric thin film materials have also been done in this work. Here in this chapter, we will present the measurement results on two different types of thermoelectric materials in thin film geometry: an epitaxial $\text{Ge}_x\text{Sn}_{1-x}\text{Mn}$ thin film, and a porous Al_2O_3 membrane filled with Bi_2Te_3 nanowires. For confirmation, SThM measurements have also been performed on Al_2O_3 membrane samples.

6.1 Epitaxial $\text{Ge}_x\text{Sn}_{1-x}\text{Mn}$ thin films

Besides the Ge:Mn thin film, the thermoelectric properties of its related alloy $\text{Ge}_x\text{Sn}_{(1-x)}\text{Mn}$ ($0.85 < x < 1$) containing nano-inclusions have also attracted our attention. The fabrication and TEM characterization of these thin films are carried out by Mustapha Boukhari and André Barski in the laboratory of INAC/CEA in Grenoble.

As it is well known that alloys have dramatically reduced thermal conductivities compared to bulk materials, the idea of adding a quantity of tin into Ge:Mn system could permit further reduction of the Ge:Mn thermal conductivity, as long as it is included in the Ge matrix as alloy disorder and does not inhibit the formation of nano-inclusions. In this way, both nano-inclusions and alloy disorder would introduce additional phonon scatterings inside the Ge matrix, and as the inclusions and alloy atoms have different sizes, being tens of nanometers

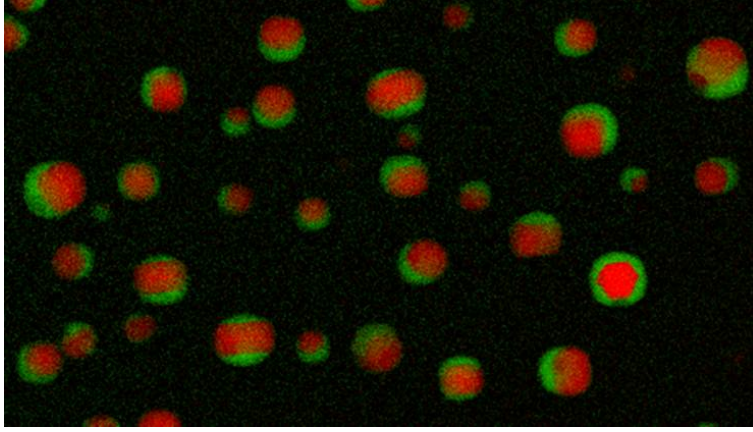


Figure 6.1: TEM image of a GeSnMn thin film grown on GOI substrate. Nano-balls are present in the Ge matrix, being Ge₃Mn₅ nano-inclusions (in red) coated by Sn (in green). The image is taken by Mustapha Boukhari.

Sample	substrate	film thickness (nm)	Sn%	Mn%	$T_{annealing}$ (°C)
GeSnMn-1	GOI	240	3.6	10	717
GeSnMn-2	GOI	240	4.9	10	708

Table 6.1: Detailed information on two GeSnMn samples that have been measured in the work.

and 0.1 nm respectively, it can be expected that the system is efficient to scatter phonons having wavelengths within a large range. Moreover, it has already been revealed that, the presence of Sn atoms bring strain to the Ge_xSn_(1-x)Mn layer, resulting in an increase of carrier mobility [125]. Hence, together with a reduced thermal conductivity due to nano-inclusions, an increased ZT value can finally be awaited for this material.

Two different GeSnMn samples have been measured in the work by the differential 3-omega method around RT. It concerns sample GeSnMn-1 and GeSnMn-2 (table 6.1), grown on GOI substrates both with 10% Mn but different Sn concentrations. Measurements have been done at 300K and 320K for the two samples. The results are presented in table 6.2 together with the results on sample Ge:Mn S7 (10% Mn) and sample Ge:Mn S5 (14% Mn). The plot in figure 6.2 represents a comparison of the measured thermal conductivities of GeSnMn samples and sample Ge:Mn S7.

From the results it can be noticed that both GeSnMn samples show significantly reduced thermal conductivities at RT, compared to Ge bulk. As compared to Ge:Mn samples containing also 10% Mn, the presence of Sn does not bring further reduction of the thermal conductivity below the value of $3.3 \text{ Wm}^{-1}\text{K}^{-1}$ at RT. On the other hand, it can be seen from figure 6.1 that Sn seems to be only present around the Ge₃Mn₅ inclusions. it is then also reasonable to compare the results of GeSnMn to that of Ge:Mn sample with 14% Mn, as 14% is the sum of Sn and Mn

6.1. Epitaxial $\text{Ge}_x\text{Sn}_{1-x}\text{Mn}$ thin films

	Temperature (K)	GeSnMn-1	GeSnMn-2	Ge:Mn 10% Mn (S7)	Ge:Mn 14% Mn (S5)
k ($\text{Wm}^{-1}\text{K}^{-1}$)	300	5.8	4.93	3.3	13
	320	7.09	4.88	4.54	-

Table 6.2: Experimental results of the thermal conductivity of two GeSnMn samples measured by the 3-omega method at 300K and 320K, in comparison with results of sample Ge:Mn with 10% Mn (S7) and with 14% Mn (S5).

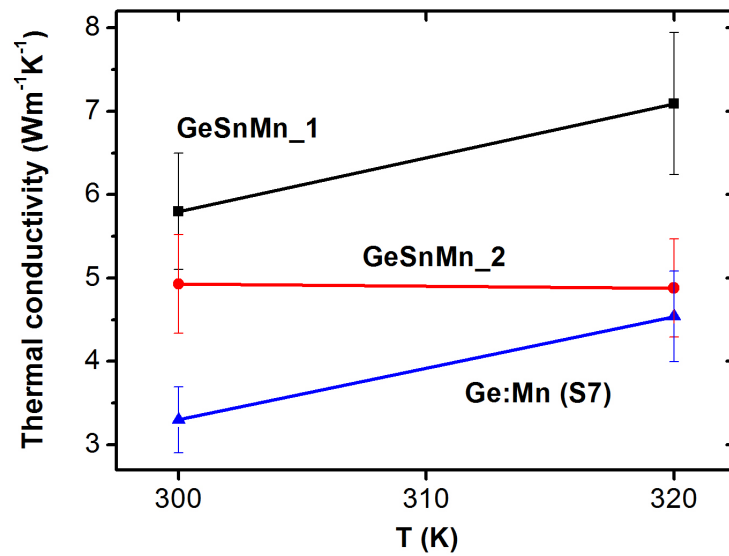


Figure 6.2: Experimental curves of the thermal conductivity of two GeSnMn samples measured by the 3-omega method at 300K and 320K, in comparison with the results of sample Ge:Mn with 10% Mn (S7) (plotted from data in table 6.2)

concentrations in GeSnMn samples. From this aspect, by replacing 4% Mn by Sn, the thermal conductivities of GeSnMn samples gain a further reduction by a factor of two. Furthermore, sample GeSnMn-1 gives an increased thermal conductivity when temperature goes from 300K to 320K, showing the same behavior as the sample Ge:Mn, for which no explanation has been obtained. However, the thermal conductivity of sample GeSnMn-1 shows a quite flat trend for temperature variation, fulfilling the expectation.

These experimental results confirmed the GeSnMn thin films to be one of the most interesting systems for thermal engineering, as well as one of the most promising Ge based TE materials. To continue the studies on GeSnMn systems, especially the influence of Sn% on the thermal conductivity and the temperature-dependent studies, more thermal conductivity measurements will be performed.

6.2 Porous alumina membranes filled with bismuth telluride nanowires

The thermal conductivity of an Al_2O_3 membrane filled with bismuth telluride nanowires (NWs) have also been measured during the work, using both the 3-omega method and the scanning thermal microscopy. This study is part of the PhD work of Meriam Ben-Khedim, supervised by Daniel Bourgault and Laurent Cagnon at the Institut Néel. This PhD project is in the frame of a collaboration with STMicroelectronics, aiming at the thermoelectric characterization of the membranes and their use in a thermoelectric module.

The fabrication of the porous Al_2O_3 membranes is developed and carried out by Laurent Cagnon in Institut Néel. It involves a two-step anodization process developed by Masuda and Fukuda in 1995 [126]. This method permits the fabrication of an anodic porous alumina film with uniform honeycomb structure, with the pore diameter controllable. As shown in figure 6.3(a) and (b), the membrane contains well arranged pores having uniform diameter, within micron sized domains. These porous membranes have been widely used as templates for the growth of NWs or nanotube arrays for applications in various domains [127, 128, 129]. In this work these porous Al_2O_3 membranes serve as templates for the fabrication of Bismuth telluride NWs. All membranes studied in the work are 40-50 μm thick with a fixed pore diameter of 60 ± 5 nm.

The Bi_2Te_3 NWs are electrodeposited from perchloric baths onto the alumina membrane [130]. As shown in figure 6.3(c), the filling of NWs in the membrane is not uniform in all pores. A mechanic polishing process is then needed to remove 10-20 μm thick membrane, to ensure a smooth surface which permits 3-omega measurements. An illustration of the cross view of a final NW-filled alumina membrane is presented in figure 6.3(d). Through alloying, two types of Bi_2Te_3 NWs can be fabricated: the p-type bismuth antimony telluride ($\text{Bi}_x\text{Sb}_{2-x}\text{Te}_3$) and n-type bismuth tellurium selenide ($\text{Bi}_2\text{Te}_{3-x}\text{Se}_x$) NWs. The NW-filled alumina membrane was then stuck to a substrate of copper or glass (up to 2 mm thick), using resist.

In this work, thermal conductivity measurements of the NW-filled alumina membrane have

6.2. Porous alumina membranes filled with bismuth telluride nanowires

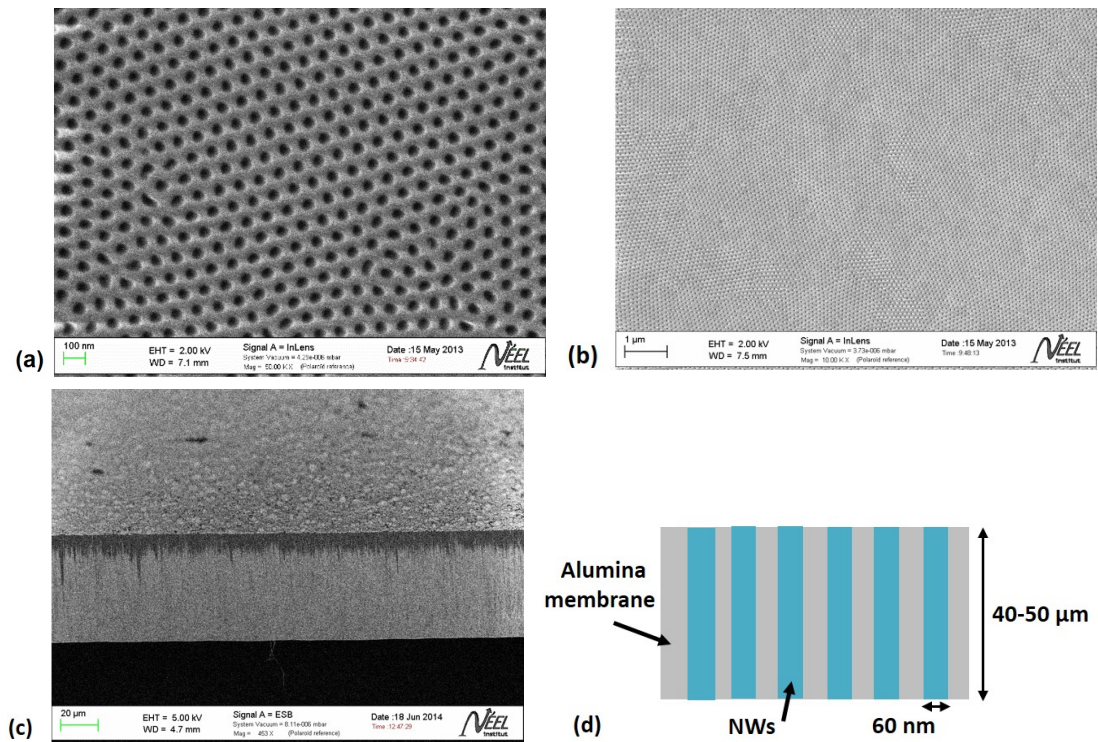


Figure 6.3: Scanning electron microscopy images (taken by Meriam Ben-Khedim) of: (a) an unfilled Al_2O_3 membrane fabricated by two-step anodization. The pore diameter can be identified to be around 50 nm; (b) an unfilled Al_2O_3 membrane containing micro-scaled domains; (c) a NW-filled Al_2O_3 membrane before polishing. The filling of NWs is not uniform in all pores. (d) An illustration of the cross view of a NW-filled Al_2O_3 membrane after polishing, being 40-50 μm thick with a pore diameter of 60 nm.

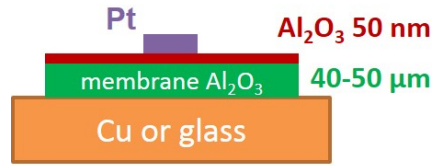


Figure 6.4: Illustration of the cross view of a porous alumina membrane (40-50 μ m thick) stuck on a substrate of Cu or glass, with a Pt transducer deposited on top for 3-omega measurements.

been done using both the 3-omega method and the SThM at RT. For the 3-omega measurements, as the NWs are electrically conductive, an insulating layer of Al_2O_3 (50 nm) by ALD is also required to separate the transducer metal and the membrane. Pt transducers (100 nm thick, 30 μ m in width and 2 mm in length) were then deposited on top of the insulating layer, as illustrated in figure 6.4.

However, unlike the cases of Ge:Mn samples, where the differential 3ω method was applied due to the fact that the Ge:Mn layers were ~ 200 nm thick, here with a thickness up to 50 μ m, the alumina membrane can be seen as a semi-infinite substrate for the transducer which has a thickness of 100 nm. In this case, only the slope of the curve $\Delta T/P$ in the right range of frequency, would be used for the calculation of the thermal conductivity of the membrane (equation 3.15).

As a test, a porous alumina membrane filled with Al_2O_3 (deposited by ALD) on a Cu substrate, has been measured using the 3-omega method. The sample is referred to as "reference membrane" in the following discussion. A precision about this reference membrane is that, the Al_2O_3 deposition by ALD fills perfectly all pores of the alumina membrane. This is due to the fact that ALD allows conformal deposits on all surfaces of the sample, including high aspect ratio nanopores. As the pores are all 60 nm in diameter in the alumina membrane, an ALD deposited thickness larger than 30 nm would fill in the pores.

The signal $V_{3\omega}$ from the reference membrane was registered at different frequencies within the range of 100-800 Hz, which corresponds to a range of thermal penetration depth of 6-20 μ m (taking the thermal diffusivity of glass, $D = 0.0034 \text{ cm}^2\text{S}^{-1}$, for the alumina membrane). As shown in figure 6.5, the real part signal of $V_{3\omega}$ as a function of $\ln \omega$ shows a perfect linearity in the frequency range. From value of the slope, the thermal conductivity of reference membrane was calculated to be $2.6 \text{ Wm}^{-1}\text{K}^{-1}$, at 300K.

An alumina membrane, stuck on a Cu substrate, filled with n-type bismuth tellurium selenide ($\text{Bi}_2\text{Te}_{3-x}\text{Se}_x$) NWs has been measured by 3-omega method. Signals of $V_{3\omega}$ were registered within the frequency range of 100-800 Hz as well. The experimental curve of $\Delta T/P$ as a function of $\ln \omega$ from this NW-filled alumina membrane was plotted in figure 6.6, together with the curve from the reference membrane, as a comparison. It can be noticed from figure 6.6 that, the curve $\Delta T/P$ from NW-filled membrane (in color black) shows two different linearities

6.2. Porous alumina membranes filled with bismuth telluride nanowires

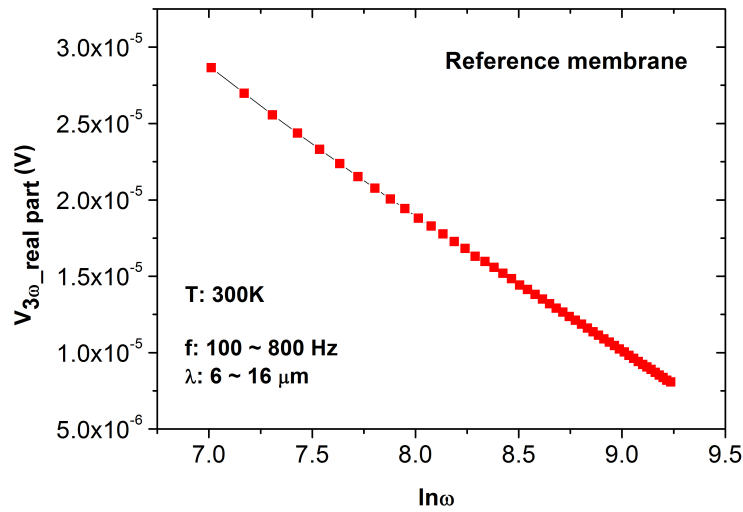


Figure 6.5: Experimental curve of the real part signal of $V_{3\omega}$ as a function of frequency ($\ln\omega$) within the range of 100-800 Hz, from the reference membrane. The curve shows a perfect linearity in the frequency range, and the thermal conductivity of the membrane can be calculated using the slope of the curve.

Sample	Frequency zone (Hz)	k ($\text{Wm}^{-1}\text{K}^{-1}$)
NW-filled membrane	10-40	0.86
	180-800	3.2
Reference membrane	100-800	2.4

Table 6.3: Values of thermal conductivities calculated using the slope values of the $\Delta T/P$ curve in two different frequency zones, from a NW-filled alumina membrane sample (calculated from experimental curve in figure 6.6). The calculated thermal conductivity of the reference membrane is presented together, for comparison.

in two zones of frequencies: a very low frequency range 10-40 Hz, and a range of 180-800 Hz. The higher frequency zone corresponds to a range of thermal penetration depth of 5-12 μm , thus the curve in this range should represent the thermal properties of the NW-filled alumina membrane. The thermal conductivities calculated using the slope values of the curve in both frequency zones are presented in table 6.3, together with the calculated thermal conductivity of the reference membrane. In the lower frequency zone, the slope of the $\Delta T/P$ curve permits the extraction of the thermal conductivity value of $0.86 \text{ Wm}^{-1}\text{K}^{-1}$. As the thermal penetration depths of low frequencies (10-40 Hz) are very possibly larger than the membrane thickness, this value of $0.86 \text{ Wm}^{-1}\text{K}^{-1}$ corresponds probably to the thermal conductivity of the glue (a polymer) that was used to stick the membrane on the Cu substrate.

The results in table 6.3 show that, contrary to expectations, the thermal conductivity of the

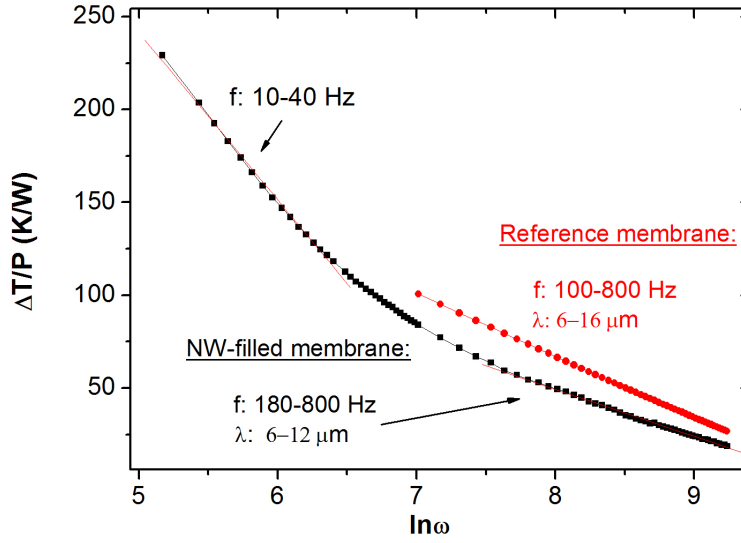


Figure 6.6: Experimental curve of $\Delta T/P$ as a function of frequency ($\ln \omega$) within the range of 100-800 Hz, from an NW-filled alumina membrane sample (in black), plotted together with the curve from the reference membrane (in red).

Sample	k_{SThM} ($\text{Wm}^{-1}\text{K}^{-1}$)	$k_{3\omega}$ ($\text{Wm}^{-1}\text{K}^{-1}$)
Reference membrane	1.71	2.4
NW-filled membrane	0.72	3.2

Table 6.4: SThM thermal conductivity results of a NW-filled membrane and the reference membrane, together with 3ω measurement results on the same two membranes.

NW-filled alumina membrane is larger than that of the reference membrane. This would mean that, the thermal conductivity of $\text{Bi}_2\text{Te}_{3-x}\text{Se}_x$ NW-arrangement is larger than that of the amorphous Al_2O_3 by ALD. To confirm the results, experiments using SThM have been carried out on the same two membranes at laboratory CETHIL in Lyon. As the thickness of the membranes ($\sim 50 \mu\text{m}$) is much larger than the tip-sample thermal exchange radius ($b_{air}=5.88 \mu\text{m}$ as calibrated in chapter 4), it is believed that the obtained thermal conductivities for the membranes were the absolute values. The SThM results of the two membranes are presented in table 6.4, together with the results from the 3ω measurements for comparison.

It can be seen from table 6.4 that, the SThM results show the contrary trend as the 3ω results, that the NW-filled membrane has a smaller thermal conductivity compared to the reference membrane. That is to say, the $\text{Bi}_2\text{Te}_{3-x}\text{Se}_x$ NW-arrangement is more thermal resistive than Al_2O_3 . Facing these contradictory results, more measurements would be required in the future. However, from the results obtained using both experimental methods, it is still clear that the

thermal conductivity of the $\text{Bi}_2\text{Te}_{3-x}\text{Se}_x$ NW-filled membrane stays very small, between $0.7\text{-}3.2 \text{ Wm}^{-1}\text{K}^{-1}$ at RT. Depending on the values of electrical conductivity and Seebeck coefficient, these NW-filled membranes can still be one of the most promising TE materials.

6.3 Conclusion

The highly sensitive 3-omega experimental setup developed for Ge:Mn thin films in the work, has also been used to perform thermal conductivity measurements on other thermoelectric thin film materials. The results on epitaxial GeSnMn thin films, containing nano-balls, revealed dramatically reduced thermal conductivities compared to Ge. Further reduction by a factor of two is also evidenced, compared to 14% Mn Ge:Mn thin film, through simply replacing 4% Mn by Sn. The experimental results of 3-omega and SThM measurements on Al_2O_3 membranes filled with Bi_2Te_3 NWs, do not agree with each other in absolute values. However the NW-filled membranes have still been proved to have low thermal conductivities, between $0.7\text{-}3.2 \text{ Wm}^{-1}\text{K}^{-1}$ at RT. Both the characterized materials have been shown to be promising TE materials for the fabrication of thin film based TE modules at RT.

Le dispositif expérimental 3-oméga développé dans ce travail pour les mesures des propriétés thermiques des films minces de Ge:Mn a également été utilisé pour effectuer des mesures de conductivité thermique sur d'autres matériaux thermoélectriques. Les résultats obtenus sur les films minces de GeSnMn épitaxiés contenant des nano-inclusions ont révélé des valeurs de conductivité thermique considérablement réduites par rapport à celle du Ge. Une réduction par un facteur deux dans GeSnMn en remplaçant simplement 4% de Mn par du Sn est également mise en évidence, par rapport à l'échantillon de Ge:Mn contenant 14% de Mn. Les résultats expérimentaux de mesures 3-oméga et de SThM sur les membranes de Al_2O_3 remplies de Bi_2Te_3 NFs, nous ont permis d'estimer la conductivité thermique des nanofils à des valeurs comprises entre 0.7 à $3.2 \text{ Wm}^{-1}\text{K}^{-1}$ à température ambiante. Ces mesures montrent que les deux matériaux caractérisés sont prometteur pour des applications en thermoélectricité.

Conclusions

This dissertation is a unique experimental investigation on the thermal properties of a new type of "electron crystal - phonon glass" material based on germanium semiconductor. These Ge:Mn thin films are composed of a single-crystalline germanium matrix embedded with spherical Ge_3Mn_5 nano-inclusions, grown by epitaxy on a Germanium-On-Insulator (GOI) substrate. The Ge matrix is p-type doped by Mn atoms, and the nano-inclusions are revealed to have a diameter distribution within 5-50 nm depending on the growth parameters in molecular beam epitaxy. By varying the Mn concentration and the annealing temperature in the growth processes of Ge:Mn, the geometries, mean diameters and diameter distributions of nano-inclusions in Ge:Mn can be tuned. With its unique fabrication processes, structural characters and physical properties, the nano-inclusion embedded Ge:Mn thin films stay as one of the most interesting 3D single-crystalline SC systems for thermal engineering.

The experimental measurements of the thermal conductivities of the Ge:Mn material have been performed using two advanced techniques: the 3-omega method at Institut Néel, and the Scanning Thermal Microscopy (SThM) in CETHIL (Centre d'Energétique et de Thermique de Lyon) in Lyon. A highly sensitive differential 3-omega measurement setup has been developed for thermal characterization of thin films. The technique permits precise measurements of thermal conductivity (error $\sim 14\%$) on electrical conductive thin films. As compared to the value for bulk Ge, dramatically reduced thermal conductivities have been revealed for Ge:Mn thin films containing different Mn% and having different inclusion geometries at room temperature. A minimum value of $3.3 \text{ Wm}^{-1}\text{K}^{-1}$ was found for Ge:Mn thin film containing 10% Mn, beating the "alloy limit" of the thermal conductivity set by $\text{Si}_{1-x}\text{Ge}_x$ alloys at room temperature ($6-12 \text{ Wm}^{-1}\text{K}^{-1}$). The measurement results of SThM confirmed the low thermal conductivities for all Ge:Mn/GOI samples at room temperature.

The strong reductions of the thermal conductivity in Ge:Mn thin films as compared to Ge demonstrated that, the presence of nano-inclusions in the crystalline Ge matrix has indeed a prominent effect on the phonon transport in the matrix. The reduced thermal conductivities of Ge:Mn thin films, in the range of $3-15 \text{ Wm}^{-1}\text{K}^{-1}$ at RT, have confirmed the theoretical predictions that the nano-inclusions introduce more scattering for phonons in Ge and result in a strong reduction of the phonon MFP. To theoretically explain the physics behind the experimental results, numerical simulations using different models based on Boltzmann transport equation have been performed. The simulation results using two different Callaway/Holland

models show encouraging coherence with the experimental thermal conductivity results, with values between $7\text{-}12\text{ Wm}^{-1}\text{K}^{-1}$ for different Ge:Mn thin films. A similar trend of the Ge:Mn thermal conductivity as a function of Mn concentration also appears compared to the experimental results. However, the models failed to fully describe the absolute low value of the Ge:Mn thermal conductivity. A complete theoretical description of the experimental data on Ge:Mn is still awaited.

In the future, investigations on the Ge:Mn system will be continued, including especially the experiments on the temperature dependence of thermal conductivity and the numerical modeling of the obtained results. The objective of the low temperature studies is to understand the mechanisms of the influence of the nano-inclusions on phonon scattering and phonon transport in SC materials, in the limit of commensurate phonon wavelength with the size of the nano-inclusions.

Further development on the fabrication of suspended thermoelectric modules based on Ge:Mn thin films can be expected as well. By implantation of phosphor, the elaboration of a n-type Ge:Mn thin film is conceivable. The doping level of the naturally p-type Ge:Mn can also be enhanced through implantation of boron, increasing the electrical conductivity up to $1000\text{ }\Omega^{-1}\text{cm}^{-1}$. Via the correlation between the structural studies and the thermal property characterization, the best Ge:Mn thin films can finally be selected as TE materials and a ZT value of 0.4 should be attainable.

Finally, the differential 3-omega setup built during this work has been used to perform thermal conductivity measurements on other type of thermoelectric materials in thin film geometry. It includes epitaxial $\text{Ge}_x\text{Sn}_{1-x}\text{Mn}$ thin films and porous Al_2O_3 membranes filled with Bi_2Te_3 nanowires. The results have revealed low thermal conductivities for both materials: $\sim 5\text{-}6\text{ Wm}^{-1}\text{K}^{-1}$ at RT for $\text{Ge}_x\text{Sn}_{1-x}\text{Mn}$ thin films, and $\sim 1\text{-}3\text{ Wm}^{-1}\text{K}^{-1}$ for a NW-filled Al_2O_3 membrane. Both materials have been demonstrated to be among the most promising TE materials, and the experiments confirmed also the high performance of the developed 3-omega setup on low thermal conductivity thin film materials.

Français:

Cette thèse présente une étude expérimentale des propriétés thermiques d'un nouveau matériau de type "cristal d'électron - phonon verre" à base de germanium semi-conducteur. Ces films minces de Ge:Mn sont composés de nano-inclusions sphériques de Ge_3Mn_5 , incluses dans une matrice de germanium monocristalline unique, élaborées par épitaxie sur un substrat de germanium sur-isolant. La matrice est Ge dopé de type p par des atomes de Mn, et les nano-inclusions sont révélées avoir une distribution de diamètre de 5 à 50 nm en fonction des paramètres de croissance en épitaxie par jets moléculaires. En faisant varier la concentration de Mn et la température de recuit pendant les procédés de croissance de Ge:Mn, la géométrie, le diamètre moyen et la distribution de diamètre de nano-inclusions dans Ge:Mn peuvent être

contrôlés. Ses caractéristiques structurales uniques font de ces films minces de Ge:Mn un système 3D prometteur pour la micro/nano ingénierie thermique.

Les mesures expérimentales de la conductivité thermique des couches minces de Ge:Mn ont été effectuées en utilisant deux techniques de pointe: la méthode 3-omega à l'Institut Néel, et la microscopie thermique à sonde locale (SThM) au CETHIL (Centre d'Energétique et de Thermique de Lyon) à Lyon. Un dispositif de la méthode 3-omega différentielle extrêmement sensible a été développé pour la caractérisation thermique des films minces de GeMn. Cette technique permet une mesure précise de conductivité thermique (erreur $\sim 14\%$) sur des films minces conducteurs électriques. Par rapport à la valeur de référence existante pour le Ge, des conductivités thermiques considérablement réduites ont été mesurées à température ambiante pour les films minces de Ge:Mn, contenant différentes concentrations de Mn et possédant donc différentes géométries d'inclusions. Une valeur minimale de $3.3 \text{ Wm}^{-1} \text{ K}^{-1}$ a été mesurée pour les films minces de Ge:Mn contenant 10% de Mn. Elle est inférieure à la limite d'alliage de la conductivité thermique fixée par les alliages de $\text{Si}_{1-x}\text{Ge}_x$ à température ambiante ($6\text{-}12 \text{ Wm}^{-1} \text{ K}^{-1}$). Les résultats de mesure obtenus en SThM ont également confirmé les faibles valeurs de conductivité thermique pour tous les échantillons de Ge:Mn/GOI à température ambiante.

Les fortes réductions de la conductivité thermique des films minces de Ge:Mn par rapport au Ge ont démontré que la présence de nano-inclusions dans la matrice cristalline de Ge a effectivement un effet important sur le transport des phonons dans la matrice. La réduction des valeurs de conductivité thermique dans les films minces de Ge:Mn, de l'ordre de $3\text{-}15 \text{ Wm}^{-1} \text{ K}^{-1}$ à température ambiante, a confirmé que les nano-inclusions introduisent plus de diffusion et entraînent donc une forte réduction du libre parcours moyen des phonons. Pour expliquer théoriquement la physique derrière les résultats expérimentaux obtenus, des simulations numériques à l'aide de différents modèles basés sur l'équation de transport de Boltzmann ont été effectuées. Les résultats des simulations effectuées à l'aide de deux modèles de Callaway/Hollande, adaptés aux couches minces de GeMn, montrent une cohérence encourageante avec les valeurs expérimentales de conductivité thermique (valeurs entre $7\text{-}12 \text{ Wm}^{-1} \text{ K}^{-1}$ pour différents films minces de Ge:Mn). Cependant, les modèles utilisés n'ont pas permis de retrouver les faibles valeurs de la conductivité thermique de Ge:Mn. Une étude théorique utilisant des moyens plus performants est actuellement en cours pour décrire les données expérimentales sur Ge:Mn.

Dans l'avenir, les recherches sur ce système de Ge:Mn seront poursuivies, en particulier l'étude de la dépendance en température de la conductivité thermique et la modélisation numérique des résultats obtenus. L'objectif des études à basse température est de comprendre les mécanismes de l'influence des nano-inclusions sur la diffusion des phonons et le transport de phonons dans les matériaux SC, lorsque la longueur d'onde des phonons devient proche de la taille des nano-inclusions.

La poursuite du développement sur la fabrication de modules thermoélectriques en suspension basés sur les films minces de Ge:Mn est également prévue. L'élaboration d'un film mince de Ge:Mn de type-n par implantation de phosphore est ainsi en cours. Le niveau de dopage du

Chapter 6. Experimental results on other nano-structured thermoelectric materials

Ge:Mn naturel de type-p peut également être renforcé par implantation de bore, ce qui peut augmenter la conductivité électrique jusqu'à $1000 \Omega^{-1} \text{cm}^{-1}$. Via l'étude et l'optimisation de la corrélation entre la structure et les propriétés thermiques des films, les meilleurs films minces de Ge:Mn devraient pouvoir être utilisés en tant que matériaux TE, et une valeur ZT de 0.4 devrait être réalisable.

Enfin, la configuration différentielle de la méthode 3-oméga mise au point pendant ce travail a été également utilisée pour effectuer des mesures de conductivité thermique sur d'autres types de matériaux thermoélectriques sous forme de films minces. Il s'agit de films minces épitaxiés de $\text{Ge}_x\text{Sn}_{1-x}\text{Mn}$ et de membranes poreuses de Al_2O_3 remplies de nanofils de Bi_2Te_3 . Les résultats ont révélé de faibles valeurs de conductivité thermique pour ces deux matériaux: $\sim 5\text{-}6 \text{ Wm}^{-1} \text{K}^{-1}$ à température ambiante pour les films minces de $\text{Ge}_x\text{Sn}_{1-x}\text{Mn}$, et $\sim 1\text{-}3 \text{ Wm}^{-1} \text{K}^{-1}$ pour une membrane de Al_2O_3 remplie de nanofils. Ces deux matériaux peuvent ainsi être considérés comme des matériaux thermoélectriques prometteurs. Ces expériences ont aussi confirmé les performances de la configuration 3-oméga développée pour mesurer les propriétés thermiques de tout type de matériaux sous forme de couches minces.

Appendix

List of all Ge:Mn samples studied in the work

Sample name	Substrate	Characters	note	$k_{3\omega}$ ($\text{Wm}^{-1}\text{K}^{-1}$)	k_{SThM} ($\text{Wm}^{-1}\text{K}^{-1}$)
MERGING02	Ge (n-type)	240 nm, Mn 6%	S8	10.4	-
MERGING04	Ge (n-type)	240 nm, Mn 2%	-	-	3.3
MERGING06	Ge (p-type)	200 nm, Mn 6%	-	6.6 _(300K) , 5.5 _(320K) ($R_C = 0$)	-
MERGING07	Ge (p-type)	240 nm, Mn 6%	-	-	1.8
GeMn-1 μm	Ge	1 μm , Mn 6%	S0	-	1.8/5.4
REC07	GOI	80 nm, Mn 8%, 327 °C	-	4.8	-
REC18	GOI	240 nm, Mn 6%, 709 °C	S1	15	-
REC15	GOI	240 nm, Mn 8%, 672 °C	S2	8.2	4.4/7.6
REC08	GOI	240 nm, Mn 8%, 743 °C	S6	7.4	-
REC12	GOI	240 nm, Mn 10%, 709 °C	S3	3.5	3.7/3.9
REC13	GOI	240 nm, Mn 10%, 757 °C	S7	3.3	3.5/5.1/8.0
REC17	GOI	240 nm, Mn 12%, 703 °C	S4	7.5	4.0/5.1
REC19	GOI	240 nm, Mn 14%, 716 °C	S5	13	4.3
GeMn/GOI1 μm	GOI	240 nm, Mn 10%, SiO ₂ 1 μm in GOI, 709 °C	-	-	5.2/5.3

List of other samples measured in this work

GaAs substrate
Si ₃ N ₄ substrate
n-type Ge substrate
p-type Ge substrate
GOI substrate
Al ₂ O ₃ thin film (50nm) on GaAs substrate
Ge _x Sn _{1-x} Mn thin films on GOI substrate
porous Al ₂ O ₃ membrane filled with Al ₂ O ₃ (50nm) by ALD, on Cu substrate
porous Al ₂ O ₃ membrane filled with Bi ₂ Te _{3-x} Se _x nanowires, on Cu substrate
Si substrate
Mg ₂ SiSb thin film (1.8 μm) on Si substrate



Bibliography

- [1] C. Blanc, A. Rajabpour, S. Volz, T. Fournier, and O. Bourgeois, “Phonon heat conduction in corrugated silicon nanowires below the Casimir limit.,” *Applied Physics Letters*, vol. 103, no. 4, p. 043109, 2013.
- [2] D. Song and C. Gang, “Thermal conductivity of periodic microporous silicon films.,” *Applied Physics Letters*, vol. 84, no. 5, pp. 687 – 689, 2004.
- [3] M. S. Dresselhaus, G. Chen, M. Y. Tang, R. G. Yang, H. Lee, D. Z. Wang, Z. F. Ren, J.-P. Fleurial, and P. Gogna, “New directions for low-dimensional thermoelectric materials.,” *Advanced Materials*, vol. 19, no. 8, p. 1043, 2007.
- [4] E. Chavez-Angel, J. Reparaz, J. Gomis-Bresco, M. Wagner, J. Cuffe, B. Graczykowski, A. Shchepetov, H. Jiang, M. Prunnila, J. Ahopelto, F. Alzina, and C. Sotomayor Torres, “Reduction of the thermal conductivity in free-standing silicon nano-membranes investigated by non-invasive raman thermometry.,” *APL Materials*, vol. 2, no. 1, p. 012113, 2014.
- [5] B. M. Curtin and J. E. Bowers, “Thermoelectric power factor enhancement with gate-all-around silicon nanowires.,” *Journal of Applied Physics*, vol. 115, no. 14, pp. 143704–1 – 143704–9, 2014.
- [6] S. Galagali, N. Sankeshwar, and B. Mulimani, “Thermoelectric transport in zno and gan nanowires.,” *Journal of Physics and Chemistry of Solids*, vol. 83, pp. 8 – 17, 2015.
- [7] S. Cecchi, T. Etzelstorfer, E. Müller, A. Samarelli, L. Ferre Llin, D. Chrastina, G. Isella, J. Stangl, J. Weaver, P. Dobson, and D. Paul, “Ge/sige superlattices for thermoelectric devices grown by low-energy plasma-enhanced chemical vapor deposition.,” *Journal of Electronic Materials*, vol. 42, no. 7, pp. 2030 – 2034, 2013.
- [8] T. C. Harman, P. J. Taylor, M. P. Walsh, and B. E. LaForge, “Quantum dot superlattice thermoelectric materials and devices.,” *Science*, no. 5590, p. 2229, 2002.
- [9] D. Rui, S. Xingliang, Z. Juanjuan, and G. Yuanwen, “Tunability of longitudinal wave band gaps in one dimensional phononic crystal with magnetostrictive material.,” *Journal of Applied Physics*, vol. 115, no. 7, pp. 1 – 8, 2014.

Bibliography

- [10] J. Vasseur, P. Deymier, B. Chenni, B. Djafari-Rouhani, L. Dobrzynski, and D. Prevoost, "Experimental and theoretical evidence for the existence of absolute acoustic band gaps in two-dimensional solid phononic crystals.," *Physical Review Letters*, vol. 86, no. 14, pp. 3012 – 3015, 2001.
- [11] A. Khelif, H. Fu-Li, A. Choujaa, S. Benchabane, and V. Laude, "Octave omnidirectional band gap in a three-dimensional phononic crystal.," *IEEE Transactions on Ultrasonics, Ferroelectrics and Frequency Control*, vol. 57, no. 7, pp. 1621 – 1625, 2010.
- [12] M. Asen-Palmer, K. Bartkowski, E. Gmelin, M. Cardona, A. P. Zhernov, A. V. Inyushkin, A. Taldenkov, V. I. Ozhogin, K. M. Itoh, and E. E. Haller, "Thermal conductivity of germanium crystals with different isotopic compositions," *Phys. Rev. B*, vol. 56, pp. 9431–9447, Oct 1997.
- [13] W. Weber, "Adiabatic bond charge model for the phonons in diamond, si ge and alpha-si.," *Physical Review B (Solid State)*, vol. 15, no. 10, pp. 4789 – 4803, 1977.
- [14] T. KLITSNER and R. O. POHL, "Phonon scattering at silicon crystal surfaces (english).," *Physical review. B, Condensed matter*, vol. 36, no. 12, pp. 6551 – 6565, 1987.
- [15] J. M. Ziman, *Electrons and phonons : the theory of transport phenomena in solids*. Oxford, Clarendon Press, 1960, 1960. Includes bibliography.
- [16] G. Kumar, G. Prasad, and R. Pohl, "Experimental determinations of the lorenz number," *Journal of Materials Science*, vol. 28, no. 16, pp. 4261–4272, 1993.
- [17] L. E. Bell, "Cooling, heating, generating power, and recovering waste heat with thermoelectric systems.," *Science*, vol. 321, no. 5895, pp. 1457 – 1461, 2008.
- [18] B. Poudel, Q. Hao, Y. Ma, Y. Lan, A. Minnich, B. Yu, X. Yan, D. Wang, A. Muto, D. Vashaee, X. Chen, J. Liu, M. S. Dresselhaus, G. Chen, and Z. Ren, "High-thermoelectric performance of nanostructured bismuth antimony telluride bulk alloys.," *Science*, no. 5876, p. 634, 2008.
- [19] H. Ju, M. Kim, and J. Kim, "A facile fabrication of n-type Bi_2Te_3 nanowire/graphene layer-by-layer hybrid structures and their improved thermoelectric performance.," *Chemical Engineering Journal*, vol. 275, pp. 102 – 112, 2015.
- [20] G. Pernot, M. Stoffel, I. Savic, F. Pezzoli, P. Chen, G. Savelli, A. Jacquot, J. Schumann, U. Denker, I. Mönch, C. Deneke, O. Schmidt, J. Rampnoux, S. Wang, M. Plissonnier, A. Rastelli, S. Dilhaire, and N. Mingo, "Precise control of thermal conductivity at the nanoscale through individual phonon-scattering barriers.," *Nature Materials*, vol. 9, no. 6, pp. 491 – 495, 2010.
- [21] C. Peixuan, Z. J. J., J. P. Feser, F. Pezzoli, O. Moutanabbir, S. Cecchi, G. Isella, T. Gemming, S. Baunack, C. G., O. G. Schmidt, and A. Rastelli, "Thermal transport through short-period SiGe nanodot superlattices.," *Journal of Applied Physics*, vol. 115, no. 4, pp. 1 – 10, 2014.

- [22] A. I. Hochbaum, R. Chen, R. D. Delgado, W. Liang, E. C. Garnett, M. Najarian, A. Majumdar, and P. Yang, “Enhanced thermoelectric performance of rough silicon nanowires,” *Nature*, vol. 451, no. 7175, pp. 163 – 167, 2008.
- [23] X. Bin, L. Chuanbo, M. Myronov, and K. Fobelets, “n-si-p-sil-xgex nanowire arrays for thermoelectric power generation,” *Solid-State Electronics*, vol. 83, pp. 107 – 112, 2013.
- [24] M. Maldovan, “Sound and heat revolutions in phononics,” *Nature*, vol. 503, no. 7475, pp. 209 – 217, 2013.
- [25] F. C. Z., G. Y., and H. J. P., “Shaped graded materials with an apparent negative thermal conductivity,” *Applied Physics Letters*, vol. 92, no. 25, p. 251907, 2008.
- [26] S. Guenneau, C. Amra, and D. Veynante, “Transformation thermodynamics: cloaking and concentrating heat flux,” *Optics Express*, vol. 20, no. 7, pp. 8207 – 8218, 2012.
- [27] S. Narayana and Y. Sato, “Heat flux manipulation with engineered thermal materials,” *Physical Review Letters*, vol. 108, no. 21, p. 214303, 2012.
- [28] L. Baowen, W. Lei, and G. Casati, “Thermal diode: rectification of heat flux,” *Physical Review Letters*, vol. 93, no. 18, pp. 184301/1 – 4, 2004.
- [29] W. Lei and L. Baowen, “Phononics gets hot,” *Physics World*, vol. 21, no. 3, pp. 27 – 29, 2008.
- [30] L. Wang and B. Li, “Thermal logic gates: Computation with phonons,” 2007.
- [31] H. Men, K. Y. K. Lee, R. M. Freund, J. Peraire, and S. G. Johnson, “Robust topology optimization of three-dimensional photonic-crystal band-gap structures,” *Optics Express*, vol. 22, no. 19, pp. 22632 – 22648, 2014.
- [32] J. Vasseur, B. Djafari-Rouhani, L. Dobrzynski, M. Kushwaha, and P. Halevi, “Complete acoustic band gaps in periodic fibre reinforced composite materials: the carbon/epoxy composite and some metallic systems,” *Journal of Physics: Condensed Matter*, vol. 6, no. 42, pp. 8759 – 8770, 1994.
- [33] C. Goffaux and J. Vigneron, “Theoretical study of a tunable phononic band gap system,” *Physical Review B (Condensed Matter and Materials Physics)*, vol. 64, no. 7, pp. 075118/1 – 5, 2001.
- [34] Y. Pennec, J. O. Vasseur, B. Djafari-Rouhani, L. Dobrzyński, and P. A. Deymier, “Two-dimensional phononic crystals: Examples and applications,” *Surface Science Reports*, vol. 65, pp. 229 – 291, 2010.
- [35] T. Gorishnyy, C. Ullal, M. Maldovan, G. Fytas, and E. Thomas, “Hypersonic phononic crystals,” *Physical Review Letters*, vol. 94, no. 11, pp. 115501/1 – 4, 2005.

Bibliography

- [36] B. Merheb, P. Deymier, M. Jain, M. Alosyna-Lesuffleur, S. Mohanty, A. Berker, and R. Greger, "Elastic and viscoelastic effects in rubber/air acoustic band gap structures: a theoretical and experimental study.," *Journal of Applied Physics*, vol. 104, no. 6, p. 064913, 2008.
- [37] Y. Liu, J.-Y. Su, Y.-L. Xu, and X.-C. Zhang, "The influence of pore shapes on the band structures in phononic crystals with periodic distributed void pores.," *Ultrasonics*, vol. 49, pp. 276 – 280, 2009.
- [38] L. Yang, N. Yang, and B. Li, "Extreme low thermal conductivity in nanoscale 3d si phononic crystal with spherical pores (english).," *Nano letters (Print)*, vol. 14, no. 4, pp. 1734 – 1738, 2014.
- [39] L. Deyu, W. Yiyang, P. Kim, S. Li, Y. Peidong, and A. Majumdar, "Thermal conductivity of individual silicon nanowires.," *Applied Physics Letters*, vol. 83, no. 14, pp. 2934 – 2936, 2003.
- [40] W. Ning, C. Haijun, H. Hongcai, N. Wataru, K. Michiko, and K. Kunihiro, "Enhanced thermoelectric performance of nb-doped srtio₃ by nano-inclusion with low thermal conductivity.," *Scientific Reports*, p. 1, 2013.
- [41] F. Liangwei, Y. Junyou, X. Ye, P. Jiangying, L. Ming, L. Yubo, and L. Gen, "Ag₂Te₂ nanoinclusion in yb_{0.2}co₄sb₁₂ for high performance thermoelectrics.," *Intermetallics*, vol. 43, pp. 79 – 84, 2013.
- [42] K. Woonchul, S. L. Singer, A. Majumdar, D. Vashaee, B. Zhixi, A. Shakouri, Z. Gehong, J. E. Bowers, J. M. O. Zide, and A. C. Gossard, "Cross-plane lattice and electronic thermal conductivities of eras:ingaas/ingaalas superlattices.," *Applied Physics Letters*, vol. 88, no. 24, p. 242107, 2006.
- [43] K. Woonchul, Z. Joshua, A. Gossard, D. Klenov, S. Stemmer, A. Shakouri, and A. Majumdar, "Thermal conductivity reduction and thermoelectric figure of merit increase by embedding nanoparticles in crystalline semiconductors.," *Physical Review Letters*, vol. 96, no. 4, pp. 045901/1 – 4, 2006.
- [44] J.-Y. Duquesne, "Thermal conductivity of semiconductor superlattices: experimental study of interface scattering.," *Physical Review B (Condensed Matter and Materials Physics)*, vol. 79, no. 15, p. 153304, 2009.
- [45] K. Termentzidis, P. Chantrenne, J.-Y. Duquesne, and A. Sotiropoulos, "Thermal conductivity of gaas/alas superlattices and the puzzle of interfaces.," *Journal of Physics: Condensed Matter*, vol. 22, no. 47, p. 475001, 2010.
- [46] K. Valalaki and A. G. Nassiopoulou, "Low thermal conductivity porous si at cryogenic temperatures for cooling applications," *Journal of Physics D: Applied Physics*, vol. 46, no. 29, p. 295101, 2013.

- [47] M. Isaiev, S. Tutashkonko, V. Jean, K. Termentzidis, T. Nychporuk, D. Andrusenko, O. Marty, R. Burbelo, D. Lacroix, and V. Lysenko, "Thermal conductivity of meso-porous germanium.," *Applied Physics Letters*, vol. 105, no. 3, p. 031912, 2014.
- [48] J. Zide, D. Klenov, S. Stemmer, A. Gossard, G. Zeng, J. Bowers, D. Vashaee, and A. Shakouri, "Thermoelectric power factor in semiconductors with buried epitaxial semimetallic nanoparticles.," *Applied Physics Letters*, vol. 87, no. 11, pp. 112102 – 1–3, 2005.
- [49] Z. Gehong, B. Je-Hyeong, J. E. Bowers, J. M. O. Zide, A. C. Gossard, Z. Bian, R. Singh, A. Shakouri, K. Woochul, S. L. Singer, and A. Majumdar, "Eras:(ingaas) $1-x$ (inalas) x alloy power generator modules.," *Applied Physics Letters*, vol. 91, no. 26, p. 263510, 2007.
- [50] Z. Gehong, B. Je-Hyeong, J. E. Bowers, L. Hong, A. C. Gossard, S. L. Singer, A. Majumdar, B. Zhixi, M. Zabarjadi, and A. Shakouri, "Thermoelectric power generator module of 16×16 bi_2te_3 and 0.6segmented elements.," *Applied Physics Letters*, vol. 95, no. 8, p. 083503, 2009.
- [51] L. E. Clinger, G. Pernot, T. E. Buehl, P. G. Burke, A. C. Gossard, C. J. Palmstro, A. Shakouri, and J. M. O. Zide, "Thermoelectric properties of epitaxial tbas:ingaas nanocomposites.," *Journal of Applied Physics*, vol. 111, no. 9, pp. 094312 – 094312–5, 2012.
- [52] W. C. Kim, *Thermal Transport in Nanostructured Materials*. PhD thesis, 2005.
- [53] T. Devillers and A. D. d. t. . A. f. a. t. o. d. Barski, *Etude des propriétés physiques des phases de $\text{Ge}(1-x)\text{Mn}(x)$ ferromagnétiques pour l'électronique de spin (French)*. PhD thesis, Université Joseph Fourier, 2008.
- [54] M. Jamet, A. Barski, T. Devillers, V. Poydenot, R. Dujardin, P. Bayle-Guillemaud, J. Rothman, E. Bellet-Amalric, A. Marty, J. Cibert, R. Mattana, and S. Tatarenko, "High-curie-temperature ferromagnetism in self-organized ge_1xmnx nanocolumns.," *Nature Materials*, vol. 5, no. 8, p. 653, 2006.
- [55] T. Devillers, M. Jamet, A. Barski, V. Poydenot, P. Bayle-Guillemaud, E. Bellet-Amalric, S. Cherifi, and J. Cibert, "Structure and magnetism of self-organized $\text{ge}_1\text{-xmnx}$ nanocolumns on $\text{ge}(001)$.," *Physical Review B (Condensed Matter and Materials Physics)*, vol. 76, no. 20, pp. 205306 – 1–12, 2007.
- [56] S. Tardif, S. Cherifi, M. Jamet, T. Devillers, A. Barski, D. Schmitz, N. Darowski, P. Thakur, J. Cezar, N. Brookes, R. Mattana, and J. Cibert, "Exchange bias in gemn nanocolumns: The role of surface oxidation.," *Applied Physics Letters*, vol. 97, no. 6, p. 062501, 2010.
- [57] A. Jain, M. Jamet, A. Barski, T. Devillers, I.-S. Yu, C. Porret, P. Bayle-Guillemaud, V. Favre-Nicolin, S. Gambarelli, V. Maurel, G. Desfonds, J. F. Jacquot, and S. Tardif, "Structure and magnetism of ge_3mn_5 clusters.," *Journal of Applied Physics*, vol. 109, no. 1, p. 013911, 2011.

Bibliography

- [58] D. Cahill and R. Pohl, "Thermal conductivity of amorphous solids above the plateau.," *Physical Review B (Condensed Matter)*, vol. 35, no. 8, pp. 4067 – 4073, 1987.
- [59] D. Cahill, M. Katiyar, and J. Abelson, "Thermal conductivity of a-si:h thin films.," *Physical Review B (Condensed Matter)*, vol. 50, no. 9, pp. 6077 – 6081, 1994.
- [60] S.-M. Lee and D. G. Cahill, "Heat transport in thin dielectric films.," *Journal of Applied Physics*, vol. 81, no. 6, p. 2590, 1997.
- [61] K. Jung Hun, A. Feldman, and D. Novotny, "Application of the three omega thermal conductivity measurement method to a film on a substrate of finite thickness.," *Journal of Applied Physics*, vol. 86, no. 7, pp. 3959 – 3963, 1999.
- [62] J. Jin, M. P. Manoharan, Q. Wang, and M. A. Haque, "In-plane thermal conductivity of nanoscale polyaniline thin films.," *Applied Physics Letters*, vol. 95, no. 3, p. 033113, 2009.
- [63] O. Bourgeois, T. Fournier, and J. Chaussy, "Measurement of the thermal conductance of silicon nanowires at low temperature.," *Journal of Applied Physics*, vol. 101, no. 1, pp. 016104 – N.PAG, 2007.
- [64] X. Hu, A. Padilla, X. Jun, T. Fisher, and K. Goodson, "3-omega measurements of vertically oriented carbon nanotubes on silicon.," *Transactions of the ASME. Journal of Heat Transfer*, vol. 128, no. 11, pp. 1109 – 1113, 2006.
- [65] A. Jain and K. Goodson, "Measurement of the thermal conductivity and heat capacity of freestanding shape memory thin films using the 3 method.," *Journal of Heat Transfer*, vol. 130, no. 10, p. 102402, 2008.
- [66] A. Sikora, H. Ftouni, J. Richard, C. Hébert, D. Eon, F. Omnès, and O. Bourgeois, "Highly sensitive thermal conductivity measurements of suspended membranes (sin and di-amond) using a 3-völklein method.," *Review of Scientific Instruments*, vol. 83, no. 5, p. 054902, 2012.
- [67] H. Ftouni, C. Blanc, A. Sikora, J. Richard, M. Defoort, K. Lulla, E. Collin, and O. Bourgeois, "Thermal conductivity measurement of suspended si-n membranes from 10 k to 275 k using the 3-volklein method.," in *Journal of Physics: Conference Series*, vol. 395, (UJE, Institut NE´EL, 25 avenue des Martyrs, Grenoble, 38042, France, 27015), p. 012109, 2012.
- [68] H. S. Carslaw and J. C. Jaeger, *Conduction of heat in solids*. Oxford University Press : New York, NY, United States, 1959.
- [69] C. Paddock and G. Eesley, "Transient thermorefectance from thin metal films.," *Journal of Applied Physics*, vol. 60, no. 1, pp. 285 – 290, 1986.
- [70] W. S. Capinski and H. J. Maris, "Improved apparatus for picosecond pump-and-probe optical measurements.," *Review of Scientific Instruments*, vol. 67, no. 8, p. 1720, 1996.

- [71] D. G. Cahill, "Analysis of heat flow in layered structures for time-domain thermoreflectance.," *Review of Scientific Instruments*, vol. 75, no. 12, pp. 5119 – 5122, 2004.
- [72] B. Bonello, B. Perrin, and C. Rossignol, "Photothermal properties of bulk and layered materials by the picosecond acoustics technique.," *Journal of Applied Physics*, vol. 83, no. 6, pp. 3081 – 3088, 1998.
- [73] R. M. Costescu, D. G. Cahill, F. H. Fabreguette, Z. A. Sechrist, and S. M. George, "Ultra-low thermal conductivity in w/al₂o₃ nanolaminates.," *Science*, no. 5660, p. 989, 2004.
- [74] S. T. Huxtable, D. G. Cahill, and L. M. Phinney, "Thermal contact conductance of adhered microcantilevers.," *Journal of Applied Physics*, vol. 95, no. 4, p. 2102, 2004.
- [75] "A fundamental introduction of time-domain thermoreflectance (tdtr)."
- [76] D. G. Cahill, "Comparison of the 3 method and time-domain thermoreflectance."
- [77] C. C. Williams and H. K. Wickramasinghe, "Scanning thermal profiler.," *Applied Physics Letters*, vol. 49, no. 23, p. 1587, 1986.
- [78] A. Majumdar, "Scanning thermal microscopy.," *Annual Review of Materials Science*, vol. 29, no. 1, p. 505, 1999.
- [79] B. A. Nelson and W. P. King, "Measuring material softening with nanoscale spatial resolution using heated silicon probes.," *Review of Scientific Instruments*, vol. 78, no. 2, pp. 024301 – 8, 2007.
- [80] P. Tovee, M. Pumarol, D. Zeze, K. Kjoller, and O. Kolosov, "Nanoscale spatial resolution probes for scanning thermal microscopy of solid state materials.," *Journal of Applied Physics*, vol. 112, no. 11, p. 114317, 2012.
- [81] A. Majumdar, J. Carrejo, and J. Lai, "Thermal imaging using the atomic force microscope.," *Applied Physics Letters*, vol. 62, no. 20, p. 2501, 1993.
- [82] G. Mills, H. Zhou, A. Midha, L. Donaldson, and J. M. R. Weaver, "Scanning thermal microscopy using batch fabricated thermocouple probes.," *Applied Physics Letters*, vol. 72, no. 22, 1998.
- [83] M.-H. Li, J. Wu, and Y. Gianchandani, "Surface micromachined polyimide scanning thermocouple probes.," *Journal of Microelectromechanical Systems*, vol. 10, no. 1, pp. 3 – 9, 2001.
- [84] M. Chirtoc, X. Filip, J. Henry, J. Antoniow, and J. Pelzl, "Sensitivity of ac scanning thermal microscopy to thermophysical parameters.," in *Journal de Physique IV (Proceedings)*, vol. 125, (Lab. Thermophys., Univ. de Reims, France), pp. 83 – 85, 2005.
- [85] A. Dawson, M. Rides, A. Cuenat, and L. Winkless, "Micro- and nano-scale measurement of the thermophysical properties of polymeric materials using atomic force microscopy.," *International Journal of Thermophysics*, vol. 34, no. 5, p. 865, 2013.

Bibliography

- [86] W. Haeblerle, M. Pantea, and J. Hoerber, "Nanometer-scale heat-conductivity measurements on biological samples.," *Ultramicroscopy*, vol. 106, no. Proceedings of the Seventh International Conference on Scanning Probe Microscopy, Sensors and Nanostructures, pp. 678 – 686, 2006.
- [87] D. Cahill, "Thermal conductivity measurement from 30 to 750 k: the 3omega method.," *Review of Scientific Instruments*, vol. 61, no. 2, pp. 802 – 808, 1990.
- [88] T. Borca-Tasciuc, A. R. Kumar, and G. Chen, "Data reduction in 3 method for thin-film thermal conductivity determination.," *Review of Scientific Instruments*, vol. 72, no. 4, p. 2139, 2001.
- [89] T. Borca-Tasciuc, L. Weili, L. Jianlin, Z. Taofang, D. Song, C. Moore, C. Gang, K. Wang, M. Goorsky, T. Radetic, R. Gronsky, S. Xiangzhong, and M. Dresselhaus, "Thermal conductivity of si/ge superlattices.," *Eighteenth International Conference on Thermoelectrics Proceedings, ICT'99 (Cat No99TH8407)*, p. 201, 1999.
- [90] T. Tao and A. Majumdar, "Reexamining the 3-omega technique for thin film thermal characterization.," *Review of Scientific Instruments*, vol. 77, no. 10, p. 104902, 2006.
- [91] Y. Q. Liu, D. Tainoff, M. Boukhari, J. Richard, A. Barski, P. Bayle-Guillemaud, E. Hadji, and O. Bourgeois, "Sensitive 3-omega measurements on epitaxial thermoelectric thin films," *IOP Conference Series: Materials Science and Engineering*, vol. 68, no. 1, p. 012005, 2014.
- [92] R. Costescu, M. Wall, and D. Cahill, "Thermal conductance of epitaxial interfaces.," *Physical Review B (Condensed Matter and Materials Physics)*, vol. 67, no. 5, pp. 54302 – 1–5, 2003.
- [93] A. Cappella, J.-L. Battaglia, V. Schick, A. Kusiak, A. Lamperti, C. Wiemer, and B. Hay, "High temperature thermal conductivity of amorphous al₂O₃ thin films grown by low temperature ald.," *Advanced Engineering Materials*, vol. 15, no. 11, pp. 1046 – 1050, 2013.
- [94] C. S. Gorham, J. T. Gaskins, G. N. Parsons, M. D. Losego, and P. E. Hopkins, "Density dependence of the room temperature thermal conductivity of atomic layer deposition-grown amorphous alumina (al₂O₃).," *Applied Physics Letters*, vol. 104, no. 25, pp. 1 – 4, 2014.
- [95] S. Lefèvre, S. Volz, J.-B. Saulnier, C. Fuentes, and N. Trannoy, "Thermal conductivity calibration for hot wire based dc scanning thermal microscopy.," *Review of Scientific Instruments*, vol. 74, no. 4, p. 2418, 2003.
- [96] A. Assy, S. Lefèvre, P.-O. Chapuis, and S. Gome's, "Analysis of heat transfer in the water meniscus at the tip-sample contact in scanning thermal microscopy.," *Journal of Physics D: Applied Physics*, vol. 47, no. 44, p. 442001, 2014.

- [97] P.-O. Chapuis, *Contribution à l'étude des transferts thermiques à l'échelle nanométrique : interaction pointe-surface*. PhD thesis, 2007.
- [98] S. Lefèvre, J.-B. Saulnier, and S. Volz, *Modélisation et élaboration des métrologies de microscopie thermique à sonde locale résistive (French)*. PhD thesis, Ecole nationale supérieure de mécanique et d'aérotechnique, 2004.
- [99] L. David, S. Gomes, and M. Raynaud, "Modelling for the thermal characterization of solid materials by dc scanning thermal microscopy.," *Journal of Physics D (Applied Physics)*, vol. 40, no. 14, pp. 4337 – 4346, 2007.
- [100] M. Yovanovich and E. Marotta, "Thermal spreading and contact resistance," *Heat Transfer Handbook*, vol. 1, p. 261, 2003.
- [101] A. Assy, *Development of two techniques for thermal characterization of materials: Scanning Thermal Microscopy (SThM) and 2 method*. PhD thesis, 2015.
- [102] A. Saci and J.-Y. D. d. t. . A. f. a. t. o. d. Duquesne, "Transport thermique dans les milieux nano-structurés (gaas)n / (alas)n (french).," 2011.
- [103] C. J. Glassbrenner and G. A. Slack, "Thermal conductivity of silicon and germanium from 3°k to the melting point," *Phys. Rev.*, vol. 134, pp. A1058–A1069, May 1964.
- [104] H. Stohr and W. Klemm *Z. Anorg. Allgem. Chem.*, vol. 241, p. 305, 1954.
- [105] M. E. M. E. Levinshstein, M. Shur, and S. L. Rumyantsev, *Properties of advanced semiconductor materials : GaN, AlN, InN, BN, SiC, SiGe*. New York : Wiley, 2001. Includes bibliographical references.
- [106] D. Singh, J. Murthy, and T. Fisher, "Effect of phonon dispersion on thermal conduction across si/ge interfaces.," *Journal of Heat Transfer*, vol. 133, no. 12, p. 122401, 2011.
- [107] V. JEAN, *Modélisation du transport de phonon dans les semi-conducteurs nanostructurés*. PhD thesis, l'Université de Lorraine, 2014.
- [108] D. Cahill and R. Pohl, "Thermal properties of a tetrahedrally bonded amorphous solid: Cdgeas2.," *Physical Review B (Condensed Matter)*, vol. 37, no. 15, pp. 8773 – 8780, 1988.
- [109] J. Alvarez-Quintana and J. Rodríguez-Viejo, "Interfacial effects on the thermal conductivity of a-ge thin films grown on si substrates.," *Journal of Applied Physics*, vol. 104, no. 7, p. 074903, 2008.
- [110] P. Le Comber and J. Mort, *Electronic and structural properties of amorphous semiconductors. Proceedings of the thirteenth session of the Scottish Universities Summer School in Physics, Aberdeen, Scotland, July 31–August 18, 1972*. Academic Press, Inc., New York, 1973.

Bibliography

- [111] A. Minnich and C. Gang, "Modified effective medium formulation for the thermal conductivity of nanocomposites.," *Applied Physics Letters*, vol. 91, no. 7, pp. 073105–1–3, 2007.
- [112] L.-C. Liu and M.-J. Huang, "Thermal conductivity modeling of micro- and nanoporous silicon.," *International Journal of Thermal Sciences*, vol. 49, pp. 1547 – 1554, 2010.
- [113] J. Callaway, "Model for lattice thermal conductivity at low temperatures," *Phys. Rev.*, vol. 113, pp. 1046–1051, Feb 1959.
- [114] P. G. Klemens, "The scattering of low-frequency lattice waves by static imperfections," *Proceedings of the Physical Society. Section A*, vol. 68, no. 12, p. 1113, 1955.
- [115] H. B. G. Casimir *Physica*, vol. 5, p. 595, 1938.
- [116] M. G. Holland, "Analysis of lattice thermal conductivity," *Phys. Rev.*, vol. 132, pp. 2461–2471, Dec 1963.
- [117] J. de Launay, *The Theory of Specific Heats and Lattice Vibrations*. Academic Press, New York, 1956.
- [118] R. E. Peierls *Annalen der Physik (Leipzig)*, vol. 3, p. 1055, 1929.
- [119] C. Herring, "Role of low-energy phonons in thermal conduction," *Phys. Rev.*, vol. 95, pp. 954–965, Aug 1954.
- [120] P. G. Klemens, "The thermal conductivity of dielectric solids at low temperatures (theoretical).," *Proceedings of the Royal Society of London. Series A, Mathematical and Physical Sciences*, no. 1092, p. 108, 1951.
- [121] D. Morelli, J. Heremans, and G. Slack, "Estimation of the isotope effect on the lattice thermal conductivity of group iv and group iii-v semiconductors.," *Physical Review B (Condensed Matter and Materials Physics)*, vol. 66, no. 19, pp. 195304 – 1–9, 2002.
- [122] W. Kim and A. Majumdar, "Phonon scattering cross section of polydispersed spherical nanoparticles.," *Journal of Applied Physics*, vol. 99, no. 8, pp. 84306 – 1–7, 2006.
- [123] J. Freeman and A. Anderson, "Thermal conductivity of amorphous solids.," *Physical Review B (Condensed Matter)*, vol. 34, no. 8, pp. 5684 – 5691, 1986.
- [124] J. R. Romero-Arias, F. Salazar, G. G. Naumis, and G. Fernandez-Anaya, "Thermal conductivity, relaxation and low-frequency vibrational mode anomalies in glasses: A model using the fermi-pasta-ulam nonlinear hamiltonian.," *Philosophical Transactions: Mathematical, Physical and Engineering Sciences*, no. 1901, p. 3173, 2009.
- [125] J. D. Sau and M. L. Cohen, "Possibility of increased mobility in ge-sn alloy system," *Phys. Rev. B*, vol. 75, p. 045208, Jan 2007.

- [126] H. Masuda and K. Fukuda, "Ordered metal nanohole arrays made by a two-step replication of honeycomb structures of anodic ..," *Science*, vol. 268, no. 5216, p. 1466, 1995.
- [127] N. Saidin, K. Kok, I. Ng, F. Bustamam, N. Mat, and S. Abidin, "Fabrication of porous alumina templates for electrochemical synthesis of nanowires.," in *AIP Conference Proceedings*, vol. 1455, (Malaysian Nuclear Agency, Industrial Technology Division, Bangi, Selangor, Kajang, 43000, Malaysia), pp. 104 – 108, 2012.
- [128] W. Daoai, Z. Lianbing, L. Woo, M. Knez, and L. Lifeng, "Novel three-dimensional nanoporous alumina as a template for hierarchical tio2 nanotube arrays.," *Small*, vol. 9, no. 7, pp. 1025 – 1029, 2013.
- [129] C. Sousa, D. Leitao, M. Proenca, J. Ventura, A. Pereira, and J. Araujo, "Nanoporous alumina as templates for multifunctional applications.," *Applied Physics Reviews*, vol. 1, no. 3, p. 031102, 2014.
- [130] M. B. Khedim, L. Cagnon, V. Serradeil, T. Fournier, and D. Bourgault, "Thermoelectric nanowires based on bismuth telluride.," *Materials Today: Proceedings*, vol. 2, no. 12th European Conference on Thermoelectrics, pp. 602 – 609, 2015.



List of Figures

1.1	Schematic representation of a 1D linear atom chain.	8
1.2	Dispersion relation curve for a 1D linear atom chain in color blue; the red lines represent the linear relation at small q	9
1.3	Schematic representation of a 1D diatomic linear chain.	9
1.4	Dispersion relation curves for a 1D diatomic linear chain model, showing one optical branch and one acoustic branche. The frequency of phonon modes at the edge of the 1 st Brillouin zone depends on the force constant and atom masses. 10	
1.5	Phonon dispersion curves of bulk germanium [13]. Symbol Γ represents the center of the Brillouin zone.	11
1.6	Spectral radiance curves of phonons in term of wavelength in germanium at different temperatures (from 1K to 300K). Each curve has a peak which is red-shifting as temperature decreases.	13
1.7	Illustration of the heat conduction in a material under a temperature gradient.	17
1.8	Schematic illustrations of normal process and Umklapp process. k_1 and k_2 are wave vectors of the two incoming phonons, k_3 the wave vector of created outgoing phonon; and k'_3 the sum of incoming phonon momentum pointing outside the first Brillouin zone, being equivalent to the k_3 in it after the transformation via a reciprocal lattice vector G	21
1.9	Thermal conductivity vs temperature of five germanium single crystals with different isotopic concentrations: ^{70}Ge (99.99%), ^{70}Ge (96.3%), ^{70}Ge (86%), ^{nat}Ge 1 and $^{70/76}\text{Ge}$. Sample ^{70}Ge (99.99%) and ^{nat}Ge 1 have been measured with two different experimental setups in Stuttgart (S) and Moscow (M). The dot-dashed line represents a T^3 law expected for pure boundary scattering, while the dashed line shows a $1/T$ dependence for phonon scattering at high temperature [12].	22

List of Figures

1.10 (a) Typical range of electrical conductivities for insulators, SCs and conductors; (b) range of thermal conductivities for liquids, nonmetallic solids, and pure metals at normal temperature and pressure.	24
1.11 The phononic spectrum, with a frequency range of 1Hz-1THz going from infra-sound to heat [24].	26
1.12 Computational phonon dispersion curve of a 3D cubic lattice PC with hollow spheres connected by cylindrical bonds. The curves show a phononic band gap of 16.26 % [31].	27
1.13 1D, 2D and 3D PCs made of two different elastic materials arranged periodically. Different colours represent materials with different elastic properties [24]. . . .	28
2.1 (a) Schematic illustration of a typical nano-inclusion embedded material system; (b) High-resolution cross-sectional TEM image of randomly distributed ErAs particles in an epitaxial matrix of InGaAs layer [48]; (c) TEM image of a Ge:Mn thin film containing nano-inclusions (taken by Dimitri Tainoff). In the image the scales of Λ_{ph} and l_{e^-} stand respectively for phonon MFP and electron MFP at RT.	32
2.2 Transverse TEM images of a Ge:Mn thin film showing the presence of manganese-rich Ge_xMn_y nanocolumns in a perfect germanium crystalline matrix [53]: (a) bright field; (b) dark field.	33
2.3 In-plane TEM images of Ge:Mn thin films (taken by Eric Prestat): (a) with the presence of Ge_3Mn_5 nano-inclusions in a 1 μ m thick Ge:Mn film; (b) showing the crystalline structures in both the Ge matrix and the inclusions.	34
2.4 (a) Schematic illustration of the Germanium-on-Insulator substrate used for the growth of the Ge:Mn thin films; (b) transverse TEM image of a Ge:Mn thin film (80 nm thick) in Ge_xMn_y nanocolumn phase grown on a GOI substrate (taken by Eric Prestat).	35
2.5 Diameter distribution graphs for nano-inclusions in Ge:Mn samples containing 8% Mn, annealed at two different temperatures: (a) at 672 °C; (b) 743 °C.	36
2.6 TEM images of Ge:Mn thin films showing new inclusion forms besides the form of sphere, from samples containing 8% Mn annealed at two different temperatures: (a) 672 °C; (b) 743 °C.	36
2.7 Transverse TEM images of Ge:Mn thin films (240 nm thick) grown on GOI substrates: (a) with Mn concentration of 12% and annealing temperature of 703 °C; (b) with Mn concentration of 6% and annealing temperature of 709 °C.	37

2.8	Diameter distribution graphs for nano-inclusions in Ge:Mn thin films with different Mn concentrations: 8%, 10%, 12% and 14%.	38
2.9	Plots of nano-inclusion concentrations C_{TEM} and $C_{cal.}$ as a function of Mn concentration.	39
3.1	Schematic diagram of a transducer metal line in a four-contact geometry, designed for 3ω measurements.	42
3.2	Schematic diagram of a cylindrical heat flow from a 1D transducer line into a semi-infinite substrate.	45
3.3	Schematic diagram of a suspended nanowire with the transducer line deposited on top for 3ω measurements [1].	46
3.4	Schematic diagrams for the case of a suspended membrane with the transducer line in the center for 3ω measurements: (a) the temperature profile; (b) the sample geometry for the measurement [66].	46
3.5	Schematic diagram of the principles of a scanning thermal microscopy	48
3.6	Schematic illustration of the profile of a film-on-substrate sample	52
3.7	Calibration curve (dotted black line) of a Pt transducer showing the evolution of its electrical resistance as a function of temperature in RT range; the straight red line is the linear fit of the experimental curve.	54
3.8	Schematic illustration of the profile of a film-on-substrate sample with an insulating layer.	55
3.9	Schematic diagram of the electrical circuit for a 3ω measurement setup using differential method.	57
3.10	Schematic diagram of the electrical circuit for a 3ω measurement setup using Wheatstone bridge.	57
3.11	Experimental graph showing the linear relation between the $V_{3\omega}$ and the cubic current on test sample GaAs using the differential method.	59
3.12	Experimental curves of signal $V_{3\omega}$ from test sample GaAs substrate using: (a) differential method; (b) Wheatstone bridge.	60
3.13	Comparison of the experimental curves at 4 mA on sample GaAs using differential method and Wheatstone bridge.	60
3.14	Illustration of the cross view of a test sample containing a thin layer of Al_2O_3 (50 nm) on top of a GaAs substrate. The Pt transducer is deposited on the oxide layer.	61

List of Figures

3.15	Curves (the real part) of the temperature oscillation signals as a function of frequency ($\ln \omega$) recorded from both the GaAs substrate sample and the $\text{Al}_2\text{O}_3/\text{GaAs}$ test sample, applying an AC current of 4 mA. The curves show the same slope, while a vertical shift is observable between them, which permits the calculation of the thermal conductivity of the Al_2O_3 layer.	61
3.16	Experimental curves of $\Delta T/P$ as a function of $\ln \omega$ measured at different currents from sample S8 (Ge:Mn 240 nm on n-type Ge substrate). The maximum and minimum values of the slope of the $\Delta T/P$ curves are identified for the analysis of the slope error in the 3-omega measurements.	62
3.17	(a) Scanning electron microscopy image of the Wollaston probe showing the composition of a Pt/Rh filament, the silver shell around the filament, and a mirror at the top of the wire arms; (b) Optical microscope image of the tip of a Wollaston probe used in the work.	64
3.18	Schematic diagram of the CCM mode in STHM with a feedback circuit added to the Wheatstone bridge. In our experiments the two fixed resistances are 100Ω and 20Ω . R_p is the total probe resistance and R_v refers to a variable resistance that is required to balance the bridge.	65
3.19	Schematic diagram of the thermal conductance network of the in-contact probe-sample system in STHM experiments.	66
3.20	Schematic diagram of the Lefèvre model to solve the probe-sample system problem in STHM experiments [98].	67
3.21	(a) Schematic illustration of the heat flux lines for two samples of different thermal conductivity λ_s . For less thermally conductive sample (λ_{s1}) the heat flux lines reach farther, thus giving a larger b_{air} . (b) Experimental data of b_{air} and G_{air} (thermal conductance through air, equals to G_c) as a function of λ_s (colored points), together with their corresponding fitting curves (in dots) [101].	69
3.22	Schematic illustration of the multi-layer structure of a Ge:Mn thin film grown on the Germanium-on-Insulator substrate, with the thickness of each layer indicated in the graph.	69
4.1	The designed mask of transducer line in four-contact geometry, with the width ($2b$) of the transducer $30\ \mu\text{m}$, the length 2 mm, and the size of the square contact $200\ \mu\text{m}$	73

4.2	Experimental setups for differential 3ω technique: (a) sample holder with the sample stuck at the center and micro-bonded to the metallic pads around for connection; the temperature of the sample holder is controlled thanks to a heater and a standard commercial platinum thermometer (behind the heater in the image); (b) sample holder connected and ready to be mounted into a cryostat; (c) a view of the whole setups with a connected sample inside the cryostat. . . .	73
4.3	Experimental curves of normalized temperature oscillation ($\Delta T/P$) as a function of frequency ($\ln\omega$) recorded from a $50\ \mu\text{m}$ wide transducer applying different AC currents, from a sample Ge:Mn on a n-type Ge substrate. The black arrow indicates the increase of current, and curves from different currents are distinguished by color.	75
4.4	Experimental curves of $\Delta T/P$ as a function of $\ln\omega$ obtained from both the 6% Ge:Mn sample and its Ge substrate (n-type) at 300K. The transducer line is $30\ \mu\text{m}$ wide and applied AC current 12 mA.	77
4.5	Scanning electron microscopy images of Ge membranes suspended between two contact pads from a GOI structure: (a) front view, the Ge membrane has $20\ \mu\text{m}$ in length and $10\ \mu\text{m}$ in width; (b) side view.	78
4.6	Illustration of a series of $\Delta T/P$ curves as a function of frequency ($\ln\omega$), corresponding to the addition of each layers on the Si substrate in a Ge:Mn/GOI sample.	79
4.7	Experimental curves of $\Delta T/P$ as a function of frequency ($\ln\omega$) from a GOI substrate sample, measured at different temperatures. The black arrow indicates the increase of temperature. Curves for different temperatures are distinguished by color.	80
4.8	Experimental curves of $\Delta T/P$ as a function of frequency from a Ge:Mn/GOI sample with 10% Mn (S7) and a bare GOI substrate, at 300K.	81
4.9	Experimental curve showing the RT thermal conductivity results of Ge:Mn thin films as a function of Mn concentration (from data in table 4.5). The error bar of each data is 14.4%. The "V" shape of the curve gives the minimum value at Mn concentration of 10%.	82
4.10	Schematic illustration of: (a) the Germanium-on-Insulator substrate used for the growth of the Ge:Mn thin films; (b) a Ge layer (240 nm) grown on the GOI substrate.	84

List of Figures

4.11	Thermal conductivities of the Si membranes, k/k_{bulk} , normalized to the bulk Si value as a function of the thickness are shown in solid red symbols, in comparison with previous works on SOI and membranes. The amorphous Si (a-Si) limit is also shown in dotted-dashed line [4]. (b) Simulation curves of the phonon MFP as a function of temperature for Ge [107]. The curve in color blue is for transverse acoustic phonons and color green for longitudinal acoustic phonons. The average Ge phonon MFP is the curve in red.	85
4.12	Experimental curves showing the temperature-dependent variation of the thermal conductivity of different Ge:Mn/GOI samples (i.e. containing different Mn concentrations or treated at different annealing temperatures).	88
4.13	Plot of the SThM experimental thermal conductivity results of different Ge:Mn samples (Ge:Mn/GOI series and sample S0) as a function of Mn% (data in table 4.8), together with results of 3ω measurements (data in table 4.5).	90
5.1	The plots of calculated phonon MFP values as a function of Mn concentration, using Minnich model ($\Lambda_{Minnich}$) and the kinetic relation with 3ω measurement results ($\Lambda_{3\omega}$).	96
5.2	Phonon dispersion curves for Ge [13] with additional indications of frequency positions ω_1 and ω_2 introduced by Holland's model.	101
5.3	The scattering efficiency of the spherical impurity as a function of size parameter, for Rayleigh, near-geometrical regimes and the combination of the two [52]. . .	105
5.4	Simulation curves of Ge bulk thermal conductivity as a function of temperature using Asen-Palmer (in red), Morelli (in black) and Holland's (in green) models. The curve in blue color is the simulation result obtained from Ge:Mn sample containing 10% Mn using concentration value C_{cal} . in Morelli's model. The inset graph is a zoom of the curves at temperature around 300K.	107
5.5	Plots of simulation results of Ge:Mn thermal conductivity as a function of Mn concentration using concentration value C_{cal} . in Asen-Palmer (in red), Morelli (in black) and Holland's (in green) models, in comparison with the "V" shape 3-omega experimental curve of Ge:Mn thermal conductivity as a function of Mn% in color blue.	109
6.1	TEM image of a GeSnMn thin film grown on GOI substrate. Nano-balls are present in the Ge matrix, being Ge_3Mn_5 nano-inclusions (in red) coated by Sn (in green). The image is taken by Mustapha Boukhari.	112

6.2	Experimental curves of the thermal conductivity of two GeSnMn samples measured by the 3-omega method at 300K and 320K, in comparison with the results of sample Ge:Mn with 10% Mn (S7) (plotted from data in table 6.2)	113
6.3	Scanning electron microscopy images (taken by Meriam Ben-Khedim) of: (a) an unfilled Al ₂ O ₃ membrane fabricated by two-step anodization. The pore diameter can be identified to be around 50 nm; (b) an unfilled Al ₂ O ₃ membrane containing micro-scaled domains; (c) a NW-filled Al ₂ O ₃ membrane before polishing. The filling of NWs is not uniform in all pores. (d) An illustration of the cross view of a NW-filled Al ₂ O ₃ membrane after polishing, being 40-50 μm thick with a pore diameter of 60 nm.	115
6.4	Illustration of the cross view of a porous alumina membrane (40-50 μ m thick) stuck on a substrate of Cu or glass, with a Pt transducer deposited on top for 3-omega measurements.	116
6.5	Experimental curve of the real part signal of $V_{3\omega}$ as a function of frequency ($\ln \omega$) within the range of 100-800 Hz, from the reference membrane. The curve shows a perfect linearity in the frequency range, and the thermal conductivity of the membrane can be calculated using the slope of the curve.	117
6.6	Experimental curve of $\Delta T/P$ as a function of frequency ($\ln \omega$) within the range of 100-800 Hz, from an NW-filled alumina membrane sample (in black), plotted together with the curve from the reference membrane (in red).	118



List of Tables

2.1	Structural parameters extracted from TEM characterization on Ge:Mn samples containing different Mn concentrations. The C_{TEM} is obtained based on TEM images with front view of the sample using a software counting method; $C_{cal.}$ is the inclusion concentration calculated theoretically based on TEM distribution graphs. The inclusion mean diameter (d_{mean}) and its standard deviation are extracted from a Gaussian distribution treatment of the inclusion distribution graphs from TEM imaging.	38
3.1	Performance comparison of three main experiment methods for thermal conductivity measurement of both bulk materials and thin films.	49
3.2	List of calibration samples used in our SThM experiments (the values of thermal conductivity and of the uncertainty are given by the material supplier NEYCO).	68
4.1	Experimental results of thermal conductivity of Ge substrate measured via a $50 \mu\text{m}$ wide transducer at different AC current, for a sample Ge:Mn on n-type Ge substrate. The values of k_{Ge} are extracted from experimental curves of $\frac{\Delta T}{P}$ presented in figure 4.3.	75
4.2	Experimental results of thermal conductivity of Ge substrate measured at different AC currents normalized regarding the value obtained with $P_l = 1 \text{ W/m}$ (k_{ref}). The results were obtained from a Ge:Mn sample on n-type Ge substrate via a $30 \mu\text{m}$ wide transducer.	76
4.3	Experimental results of thermal conductivity of Ge substrate measured at different temperatures with a dissipation power of 1 W/m . The results were obtained from a Ge:Mn sample on n-type Ge substrate via a $30 \mu\text{m}$ wide transducer.	76
4.4	Experimental results of the Si substrate thermal conductivity at different temperatures from a bare GOI substrate sample, extracted from figure 4.7.	79

List of Tables

4.5	Experimental results of thermal conductivity of different Ge:Mn thin films on GOI (with different Mn% or annealed at different temperatures), obtained from 3ω measurements at RT. The error of each experimental value is 14.4%.	80
4.6	Calculation results of the phonon MFP ($\Lambda_{3\omega}$) in Ge:Mn thin films grown with different Mn concentrations using the kinetic relation based 3ω experimental results. The Ge phonon MFP at RT is taken to be 200 nm.	84
4.7	SThM experimental data for the calibration in experiment M1, using bulk SiO_2 , ZrO_2 and Ge as reference samples.	89
4.8	SThM experimental thermal conductivity results (measurement M1 and M2) on different Ge:Mn samples (Ge:Mn/GOI series and sample S0) at RT, in comparison with 3ω measurement results on the same samples.	89
5.1	Calculation results of phonon MFP for Ge:Mn thin films grown with different Mn concentrations, using Minnich model ($\Lambda_{Minnich}$) and the kinetic relation (equation 4.1) with 3ω experimental results ($\Lambda_{3\omega}$). $k_{3\omega}$ refers to experimental values of thermal conductivity for Ge:Mn samples obtained by 3ω measurements.	95
5.2	Simulation results of thermal conductivities of Ge:Mn samples grown with different Mn concentrations, using both modified Callaway/Holland's models mentioned in the text and the Holland's model. The results are indicated as k_{Asen} , $k_{Morelli}$ and $k_{Holland}$. A and B are respectively the shape parameter and scale parameter from a Gamma distribution treatment of the TEM distribution graphs of nano-inclusions in Ge:Mn. The mean radius r and the variance s^2 are calculated as $A \times B$ and $A \times B^2$ respectively. One should notice that these mean radii and standard deviation values for Ge:Mn samples are not the same as in table 2.1 in chapter 2, where Gaussian fit has been applied.	108
6.1	Detailed information on two GeSnMn samples that have been measured in the work.	112
6.2	Experimental results of the thermal conductivity of two GeSnMn samples measured by the 3-omega method at 300K and 320K, in comparison with results of sample Ge:Mn with 10% Mn (S7) and with 14% Mn (S5).	113
6.3	Values of thermal conductivities calculated using the slope values of the $\Delta T/P$ curve in two different frequency zones, from a NW-filled alumina membrane sample (calculated from experimental curve in figure 6.6). The calculated thermal conductivity of the reference membrane is presented together, for comparison.	117
6.4	SThM thermal conductivity results of a NW-filled membrane and the reference membrane, together with 3ω measurement results on the same two membranes.	118